THESIS FOR THE DEGREE OF DOCTOR OF PHILOSOPHY

Experimental Studies of Effusion Cooling

K. M. BERNHARD GUSTAFSSON

Department of Thermo and Fluid Dynamics
CHALMERS UNIVERSITY OF TECHNOLOGY
Göteborg, Sweden 2001

Experimental Studies of Effusion Cooling
K. M. BERNHARD GUSTAFSSON
ISBN 91-7291-028-3

Doktorsavhandlingar vid Chalmers tekniska högskola
Ny serie nr 1712
ISSN 0346-718X

Institutionen för termo- och fluiddynamik
Chalmers tekniska högskola
SE-412 96 Göteborg, Sweden
Phone +46-(0)31-7721400
Fax: +46-(0)31-180976

Cover:
Stream-traces of a slanted jet in crossflow based on measurements using laser-Doppler anemometry. The stream-traces are colored by the turbulent kinetic energy and the thicker magenta colored stream-tubes show vortex cores.

Vasastadens bokbinderi
Göteborg, Sweden 2001

Experimental Studies of Effusion Cooling

by

K. M. Bernhard Gustafsson

Deparment of Thermo and Fluid Dynamics
Chalmers University of Technology
SE-412 96 Göteborg, Sweden

Summary

The desire to increase efficiency of jet engines, has led to an increase in temperature in the combustion chambers and in the turbine stage. There is thus an interest in efficient cooling methods. Film cooling and effusion cooling are often used where there is a great heat load.

A parametric study of surface temperature distributions on effusion cooled plates was done by means of infrared thermography. The effects of different temperature ratios, velocity ratios, Reynolds numbers, hole spacings, injection angles and thermal heat conductivity of the wall material were investigated. The experiment was designed to scale with a combustion chamber condition of a real gas turbine. A linear relationship between surface temperature and temperature ratio between the hot crossflow and the coolant was found. The results show the way in which the different parameters act and their relative importance. It is intended that the results of this study will be helpful in finding a design in which it is ascertained that the wall temperature is kept below a certain value.

A complete mapping of the 3D velocity field and turbulence fields near one of the injection holes in the third row of holes was made using laser-Doppler anemometry. In this case, $T_{jet}/T_c = 1$, Re_d=5800, U_{jet}/U_0=0.89 and the jet was injected at an angle of 30° to the crossflow. The three velocity components and the complete turbulent stress tensor have been measured in 35340 points around and behind the jet. Such a complete experimental mapping of the velocity field and turbulence field has not, to the best of the knowledge of the author, been presented before. A topological map of the flow field is presented, and the vorticity field and pressure field are discussed. The different terms in the production of the Reynolds stresses are presented. The coolant and crossflow fluid was found to mix efficiently in the three-dimensional mean flow field.

Keywords: effusion cooling, full coverage film cooling, film cooling, jet in crossflow, infrared thermography, laser-Doppler anemometry, flow visualization

Preface

This thesis has two parts, I & II. The first part presents surface temperature measurements made on an effusion cooled plate. All thermography data are published (1) as listed below and a condensed version as has been published (2). The second part reports on detailed experimental study of the flow field around a typical jet on an effusion-cooled plate (a slanted jet in crossflow). A feasibility study of the flow field was made and presented at LADOAN10 (3). A more elaborate measurement series was presented at APS/DFD'00 (4).

(1) GUSTAFSSON, K. M. B. An experimental study of the surface temperature of an effusion-cooled plate using infrared thermography. Thesis for the degree of Licentiate in Engineering. *Report no. 98/9*. Department of Thermo and Fluid Dynamics, Chalmers University of Technology, SE-412 96 Göteborg, Sweden, 1998.

(2) GUSTAFSSON, K. M. B. & JOHANSSON, T. G. An experimental study of surface temperature distribution on effusion-cooled plates. *Journal of Engineering for Gas Turbines and Power* **123**(2).

(3) GUSTAFSSON, K. M. B. LDA-measurements of jets in crossflow for effusion cooling applications. To appear in a bound volume of selected papers. *Applications of Laser Techniques to Fluid Mechanics*, 10^{th} International Symposium, July 10-13, 2000, Lisbon, Portugal.

(4) GUSTAFSSON, K. M. B. & JOHANSSON, T. G. An experimental study of a slanted jet in crossflow. 53^{rd} Annual Meeting of the American Physical Society - Division of Fluid Dynamics, November 19-21, 2000, Washington D.C., *Bull. Am. Phy. Soc.* **45**(9). Also, as a video entry in the Gallery of Fluid Motion.

Acknowledgements

I would like to thank my adviser Gunnar Johansson for his guidance, his expertise and many interesting discussions during the course of this thesis. Many thanks also to my examiner Lars Davidson for supervision and encouragement. I am very grateful to technicians Uno Hansson, Roland Andersson and Morgan Svensson for all their help with the construction of my experimental set-up. Lars Jernquist helped a great deal with miscellaneous electrical devices and circuit boards. Thanks go to William K. George for great sailing and introducing me to Turbulence. Help with the thermography measurements by the Department of Solid Mechanics at Chalmers, Örjan Staaf at FOI Linköping and Arne Roos at Ångströmlaboratoriet at Uppsala Universitet is gratefully acknowledged. Thanks also go to Anders Janocha at Chalmers Medialab for the editing and processing of the computer animations.

The financial support of Energimyndigheten, NUTEK and Bengt Ingeströms stipendiefond is gratefully acknowledged.

Le savant n'étudie pas la nature parce que cela est utile; il l'étudie parce qu'il y prend plaisir et il y prend plaisir parce qu'elle est belle. Si la nature n'était pas belle, elle ne vaudrait pas la peine d'être connue, la vie ne vaudrait pas la peine d'être vécue. - Henri Poincaré

Contents

Part I

Surface temperature distribution

Chapter 1

Introduction

Since the dawn of jet engines, rockets and space vehicles, there has been a need for cooling parts that are exposed to hot or even ionized gases. The combustion chamber walls, turbine endwalls, turbine blades and flameholders especially need effective cooling. The desire to increase efficiency, i.e. reduce the specific fuel consumption and raise the thrust/weight ratio of jet engines and gas turbines, has led to an increase in pressure and temperature in the combustion chambers and in the turbine stage. Typical examples are shown in figure 1.1 and figure 1.3. The lifetime of a combustion chamber wall will decrease as the temperature increases. Efficient cooling methods such as *effusion cooling* (full coverage film cooling or discrete hole cooling) must thus be used to protect the wall. Effusion is the emergence of a gas from a container through a small hole. To protect solid surfaces from high temperature gases, a secondary fluid is usually introduced in the boundary layer. This secondary fluid can enter the boundary layer in several different ways, usually through holes or slots in the wall. Replacing a part of the solid wall by a porous wall section and letting a cooling fluid flow through this section yields a very efficient cooling method, *transpiration cooling* (mass transfer cooling), where the cooling medium approaches

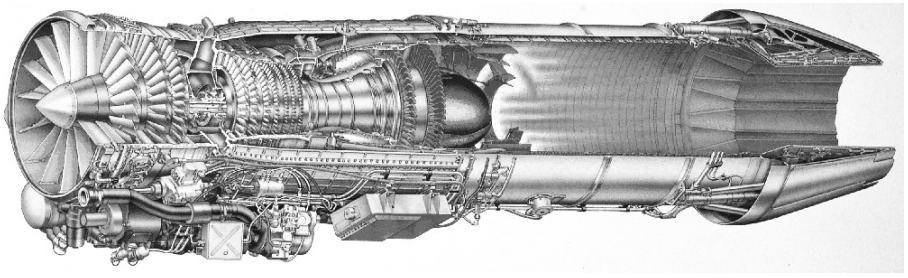

Figure 1.1: The RM12 jet engine.

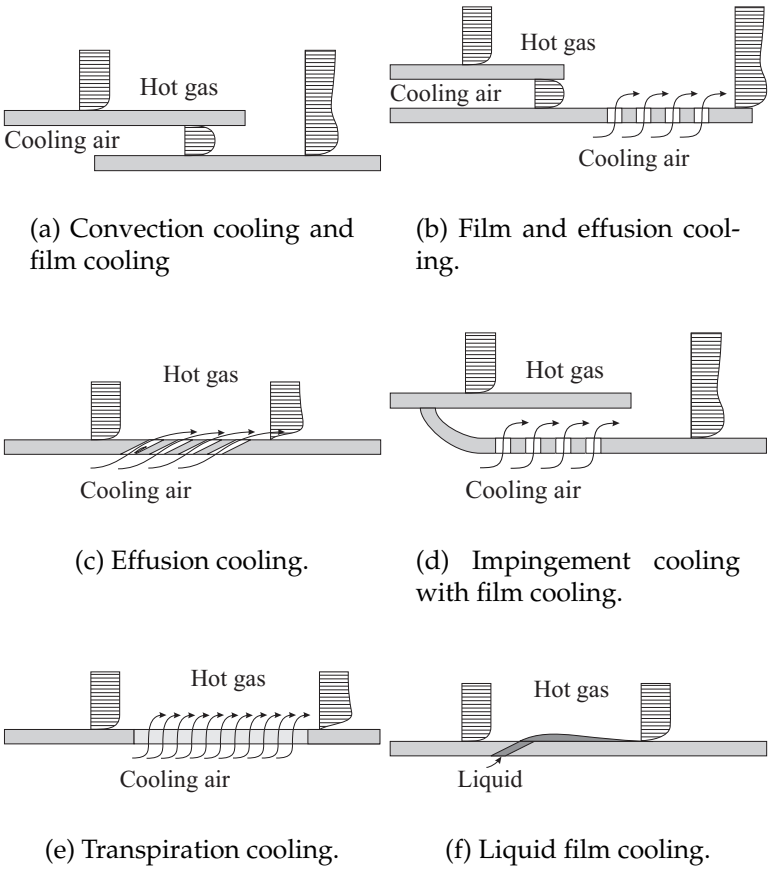

(a) Convection cooling and film cooling

(b) Film and effusion cooling.

(c) Effusion cooling.

(d) Impingement cooling with film cooling.

(e) Transpiration cooling.

(f) Liquid film cooling.

Figure 1.2: Different cooling methods.

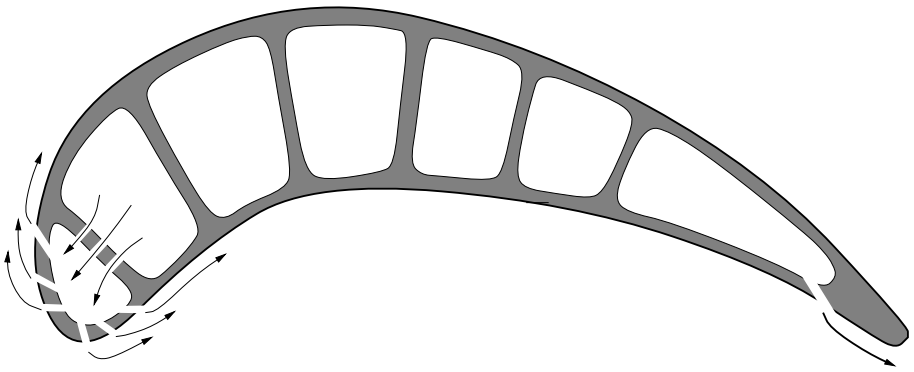

Figure 1.3: A cross-section of a turbine blade in a gas turbine. The leading and trailing edges are cooled by film cooling and internally by impingement cooling, while the middle section is cooled by internal convection cooling.

the temperature of the wall, see Eckert & Cho (1994). Although probably one of the most efficient methods, transpiration cooling suffers from two serious disadvantages. Porous materials do not have the strength to withstand the mechanical and thermal stresses required. The small pore size leads to clogging, which results in an uneven distribution of the cooling fluid and causes overheating. The most practical cooling method is perhaps *effusion cooling*, in which the cooling fluid is injected into the boundary layer through discrete holes (three-dimensional) or through slots (two-dimensional). Film cooling is not intended to cool the location at which the injection takes place but to protect the region downstream. An alternative method is *convection cooling*, in which no cooling fluid is introduced into the boundary layer. The heat is thus transferred by conduction through the wall. Eckert & Livingood (1954) compared convection, transpiration and film cooling methods. Their finding was that transpiration cooling is the most effective cooling method, followed by film cooling and convection cooling. Convection cooling combined with film cooling is shown in figure 1.2(a) and effusion cooling and film cooling are shown in figures 1.2(b) and 1.2(c). Transpiration cooling is shown in 1.2(e). Liquids can be used as cooling fluids at which the wall is cooled by the endothermic process of vaporization, see figure 1.2(f). There are still other types of cooling methods, such as *ablation cooling* (sublimation cooling). In this method, the material in the wall decomposes and can be used for only a short time, e.g. in rocket nozzles. Both ablation and transpiration cooling are highly effective and can be used exactly where the heat transfer load is the highest. Film cooling and transpiration cooling also protect the wall from radiative heat transfer if the cooling medium possesses strong absorption bands or is highly scattering. The superior effectiveness of transpiration cooling over convection cooling is reduced if the cooling medium is transparent.

The short-term goal of this project was to provide experimental surface wall temperature data useful for the design of effusion-cooled combustion chamber walls, and a parametric study of wall temperatures of an effusion-cooled plate was thus done which is described in part I and in Gustafsson (1998). Different conditions in a real combustion chamber were mapped by varying naturally occurring non-dimensional variables. It is intended that the results of this study will be helpful in finding a design in which it is ascertained that the wall temperature is kept below a certain value (about 900°C in a practical case) for the varying operational parameters at hand and for this to be accomplished for a minimum amount of cooling air. The wall temperatures were measured with an infrared camera. As the surrounding walls were hotter than the cooled test plate, the measured wall temperature must be corrected. Reflections from

surrounding walls were treated by a simple radiative transfer model. An error estimate of the measured temperatures is also presented.

Many different operational and design parameters exert an influence on the surface temperature distribution. This study examined the way in which these parameters act and their relative importance. These results may also be useful for comparison with numerical results.

A large number of investigations on film cooling have been carried out, and the research area is very active. Previous work on film cooling and jet in crossflow can be divided into five different groups:

1. surface static pressure distributions

2. flow visualization

3. empirical data including point-wise velocity and temperature measurements in 1D and sometimes in 2D, film cooling effectiveness etc.

4. mass transfer studies (analogous to adiabatic film cooling effectiveness) on surfaces under isothermal conditions.

5. analytical modeling

Foster & Lampard (1980) investigated injectant concentrations downstream of one row of holes. The injection angle, upstream boundary layer thickness and lateral hole spacing were varied. Shallow injection showed the best effectiveness for small blowing rates and steep injection was better at high blowing rates.

Eckert (1984) gave methods to predict heat transfer in film cooled systems from adiabatic and isoenergetic heat transfer coefficients.

Bazdidi-Tehrani & Andrews (1994) investigated the adiabatic film cooling effectiveness of an effusion cooled plate. A significant increase in film cooling performance was found when the number of holes was increased. The film cooling performance was furthermore found to vary little with temperature ratio. It was also shown that it is possible with effusion cooling to reduce the coolant airflow to 10%–20% of the combustor airflow. Current types of wall film cooling use about 40%–50%.

Salcudean *et al.* (1994) made measurements of leading edge film cooling. Rapid changes in the flow rate from the holes was observed for small overall flow rates because the pressure drops when the crossflow is accelerated. This uneven distribution of coolant is a problem that arises when the film cooling holes receive their supply from a common plenum.

Cho & Goldstein (1995a) & (1995b) present Sherwood number, Sh, data (mass transfer coefficients) within the injection holes, on the back surface

and on the exposed surface using a naphtalene sublimation technique. The mass transfer data were related to the adiabatic film cooling effectiveness. Their findings were that the mass transfer coefficient was rather uniform within the hole. A three to four times higher *Sh* than for a flat plate was found at the sides on the top surface for $\rho_{jet}U_{jet}/\rho_0 U_0 < 1$. Blowing factors above 1.0 instead resulted in high *Sh* downstream of the jet.

Friedrichs *et al.* (1996) carried out measurements of adiabatic heat transfer coefficients on endwalls in a linear turbine blade cascade using a diazo technique (ammonia gas and diazo surface coating). An oil and dye surface flow visualisation was also presented. Effects of the three-dimensional separation lines at the endwall on the cooling film were examined and under- and over-cooled regions were indicated.

Goldstein & Stone (1997) made ammonia-diazo flow visualizations of row-of-holes film cooling on convex and concave walls. Their findings were that the rate of injection determined whether the injection angle effect was large or small. The injection angle effect was small for small blow factors and the injection angle was important for large blow factors. On the concave wall, high blowing rates and shallow injection angle gave the best cooling effect. Injection at a momentum flux ratio of 0.25 with a high density ratio and shallow injection was preferred on the convex wall.

Ligrani & Ramsey (1997) measured adiabatic and isoenergetic Stanton numbers on a film cooled wall with two rows of compund angle injection holes and also with no compound angle. The compund angle configuration showed better film cooling effectiveness.

Gritsch *et al.* (1998a) made detailed measurements of adiabatic film cooling effectiveness for single hole injection at high Mach numbers using infrared thermography. Both cylindrical and diffuser shaped hole geometries were studied. Expanded hole exits showed better spreading of the coolant than cylindrical holes. Discharge coefficients (ratio of actual mass flow to ideal mass flow, assuming isentropic expansion in the hole) for expanded hole exits were investigated by Gritsch *et al.* (1998b). The laid-back fan shaped hole showed the best film cooling performance. Sasaki *et al.* (1979) and Martiny *et al.* (1995) also report infrared thermography measurements but for multi-row film cooling.

Leontiev (1999) gave a review of methods for calculations of heat transfer under film cooling. Film cooling effectiveness correlations that account for longitudinal pressure gradients, compressibility, swirl, roughness of the surface and turbulence of the main flow was presented. Methods to solve the conjugate heat transfer problem, i.e. account for the longitudinal heat conductance along the wall were also given. Transpiration cooling was found to be the most effective with minimal discharge of coolant.

This study differs from most others in that here the cooling effect of several rows of holes, distributed over 100 diameters, is studied. The results of investigations on the effect of single or double rows of holes can not be adapted to this case with several rows of holes. Vortices generated by different jets in different rows will interact with each other, creating flow patterns that are not present in the single row cases. The present study gives the effects of many different operational and design parameters studied under the same experimental conditions.

A flow field measurement of one single jet on an effusion cooled plate was made using laser-Doppler anemometry. This experiment is described in part II on page 45. The topology of the velocity field, Reynolds stresses etc for a typical effusion cooling jet are given here. Computing heat transfer on film cooled walls poses a great challange to numerical modelers. These models must be validated against experimental results, which motivates the present study.

Chapter 2

Experimental set-up

2.1 Wind tunnel

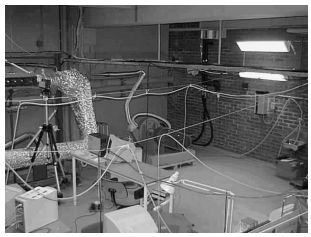

The wind tunnel used in these experiments was originally designed, built and used by Rydholm (1995) and was re-designed to allow new experiments. The test section, the gauze screens, the honeycomb, the plenum chamber, the heat exchanger, the control units and the instrumentation were replaced. A layout of the experimental set-up is shown in figures 2.1 and 2.2 on the next page. The contraction ratio of the wind tunnel is 5.6.

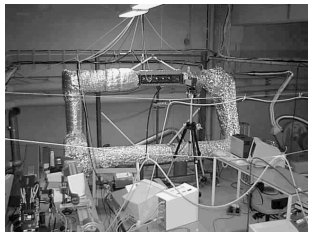

The wind tunnel consists of two closed loops, one hot main loop and one secondary cold loop, see figure 2.1. The main loop is able to withstand temperatures of 300°C and is heated by an 8 kW heater. A Pt-100 RTD measures the temperature and is used to control the heater. The velocity is measured by a removable static pitot tube located in the first upwind lid in the test section. Six lids were used to allow optical access for the infrared camera used in the wall temperature measurements. The cooling air is taken from the main loop and cooled by a compact heat exchanger. A vortex-shedding flow meter measures the volumetric flow rate in the secondary loop. (The vortices are shed from a strut at frequencies proportional to the flow velocity.) The two-wire signal (4 mA to 20 mA) from the vortex meter is fed to the PID-controller of the driver, which controls the fan.

The velocity profile in the main duct was measured by LDA and found to be uniform within 0.5%. The plenum chamber has one perforated plate

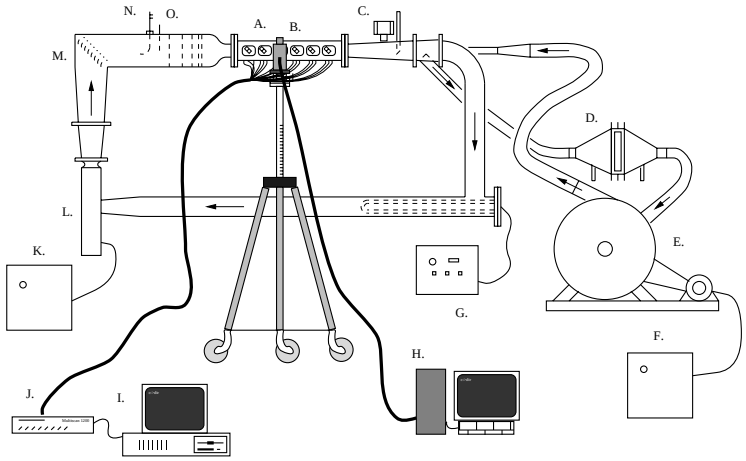

A. Test section with thermocouples (type T) mounted in wall.
B. Infrared camera: AGEMA THV 900
C. Schlumberger vortex flow meter
D. Compact heat exchanger
E. Fan
F. Control drive
G. Heater and control unit
H. Agema system controller for the THV 900 system (Erika)
I. PC 386
J. IOtech Multiscan 1200, temperature measurement instrument
M. Vanes
N. RTD, Pt100

Figure 2.1: Side view of the experimental set-up. (Reprinted with the permission of ASME.)

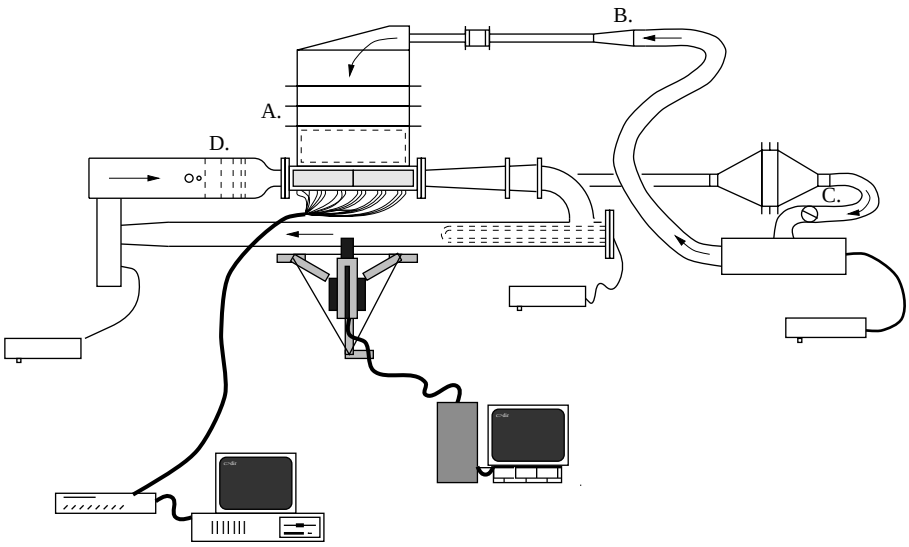

A. Plenum chamber with nets
B. Contraction with honeycomb
C. Valve
D. Net arragement

Figure 2.2: Top view of the experimental set-up.

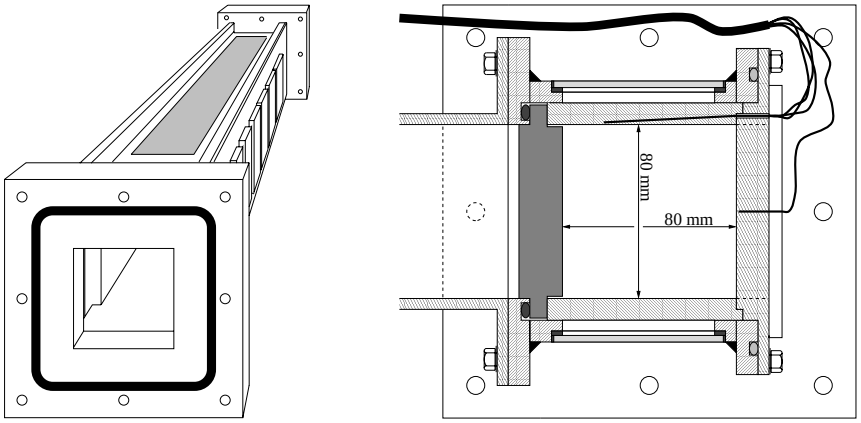

(a) The test section. High temperature resistant Viton O-rings were used where gaskets were needed.

(b) A cross-section showing the thermocouples mounted in the side wall and in the lid. The innermost walls can be changed to walls with optical access.

Figure 2.3: General picture of the test section.

with a 5% open area and three gauze screens for flow adjustment. The velocity profile in the plenum chamber was measured by LDA and found to be uniform within 6% in the area between 130 mm and 510 mm (the plenum chamber was 660 mm long) when no test plate was mounted. As knowledge of the surrounding wall temperatures is important for the infrared thermography measurements, 18 thermocouples of type T (Copper versus Nickel) were mounted in the side wall of the test section and in the removable lids. The signals were recorded by a temperature measurement device and exported to a workstation for use in the wall temperature correction program. The test section measures 80 mm $\times$ 80 mm $\times$ 720 mm, see figure 2.3. The side walls can be removed and replaced by windows of ordinary glass of high optical quality. Thin glass (approximately 1.5 mm) was used to avoid cracks caused by temperature gradients. Optical access makes possible e.g. LDA and LIF measurements.

2.2 Test plates

As different hole spacings, injection angles and wall materials were to be studied, the test plates were made exchangeable. An example of a hole pattern is shown in figure 2.4 on the next page. The test plates were made of steel and teflon, which possess quite different thermal conductivities,

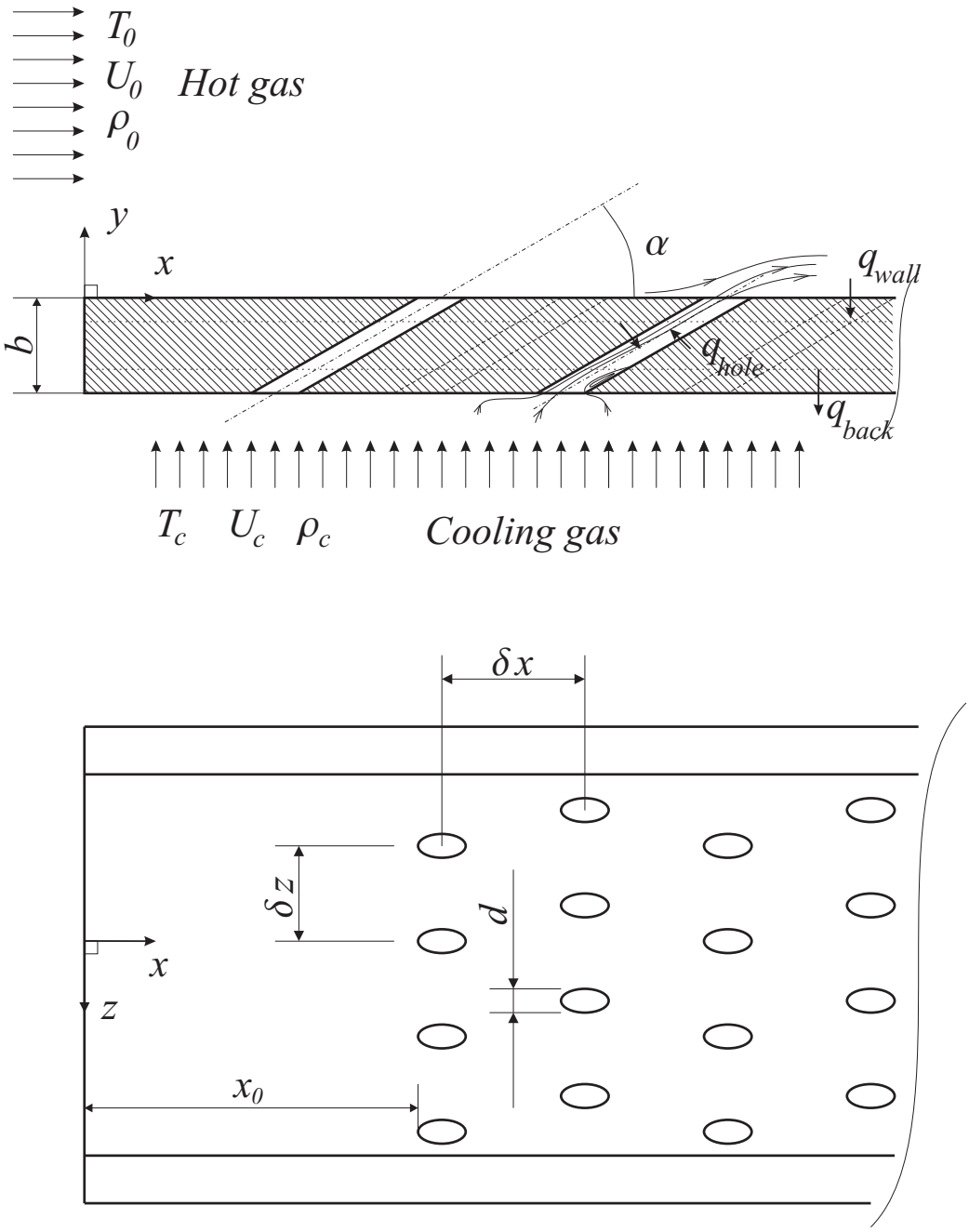

Figure 2.4: The test plate with an example of hole pattern. *Top:* Thole *et al.* (1997) reported a separation bubble in the injection hole on the lee side for stagnant plenum supply.

Case	T_0	T_c	U_0	U_c	δx	α	n	λ_s
	[°C]	[°C]	$\left[\frac{\text{m}}{\text{s}}\right]$	$\left[\frac{\text{m}}{\text{s}}\right]$	[mm]	[°]		$\left[\frac{W}{m \cdot K}\right]$
13	249	27.5	28.9	0.30	30	30	84	45
47	208.1	25.6	16.9	0.29	30	30	80	0.5
49	200	28	30.2	0.51	30	30	80	0.5
50	200	26.2	30.3	0.29	30	30	80	0.5
59	250	27	30.0	0.30	30	30	80	0.5
63	270	33.5	17	0.50	30	30	80	0.5
65	271	32.8	30	0.50	30	30	80	0.5
67	272	32.8	45.6	0.50	30	30	80	0.5
83	250	29	30	0.29	15	30	156	0.5
85	250	30.5	46.1	0.49	15	30	156	0.5
97	200	30	17	0.33	60	20	44	0.5
99	200	30	30	0.33	60	20	44	0.5
101	200	29.5	46.1	0.33	60	20	44	0.5
103	247	32.3	17	0.33	60	20	44	0.5
105	247	31.6	29.9	0.33	60	20	44	0.5
107	247	30.1	46	0.33	60	20	44	0.5
115	150	25.6	46.1	0.33	60	20	44	0.5
116	287.8	32.4	46	0.33	60	20	44	0.5
122	200	28.8	30	0.30	30	20	80	0.5
128	250	28.3	17	0.30	30	20	80	0.5
131	250	30.5	30	0.30	30	20	80	0.5
134	250	28.7	46	0.30	30	20	80	0.5
143	200	25.7	17	0.29	15	20	156	0.5
144	200	27.3	30	0.29	15	20	156	0.5
152	250	27.3	17	0.295	15	20	156	0.5
155	249	28	30	0.295	15	20	156	0.5
157	248	30.3	46	0.49	15	20	156	0.5
158	250	28.5	46	0.293	15	20	156	0.5
171	200	32	30.1	0.30	60	15	40	0.5
172	200	36	46.1	0.48	60	15	40	0.5
194	200	26	30.1	0.29	30	15	76	0.5

Table 2.1: Operational and design parameters for different test cases. The spanwise hole spacing, δz was 20 mm and the wall thickness, b, was 20 mm, for all test plates.

Properties of teflon	**Value**
Density, ρ_s	2.14 kg/m^3
Thermal conductivity, λ_s	0.5 W/(m·K)
Coeff. of linear thermal expansion	
- from 20°C to 100°C	$16{\cdot}10^{-5}$ K^{-1}
- from 20°C to 200°C	$19.5{\cdot}10^{-5}$ K^{-1}
- from 20°C to 300°C	$25{\cdot}10^{-5}$ K^{-1}
Specific heat, c_p	
at 0°C	960 J/(kg·K)
at 50°C	1050 J/(kg·K)
at 200°C	1250 J/(kg·K)
Melting point (becomes a gel)	325°C
Max service temperature	260°C

Table 2.2: Technical specifications of teflon with 10% carbon according to the manufacturer.

$\lambda_s \approx 45$ W/(m·K) for steel and $\lambda_s \approx 0.5$ W/(m·K) for teflon. To reduce the reflections from the hot surrounding walls, the plates were coated with a highly emissive paint, NEXTEL velvet coating, which has an emissivity of 0.96 in the (8-12) μm band. The teflon used contained approximately 10% carbon, which made the coating stick better to the plate. An injection hole diameter of 5 mm was choosen in the scaling of the experiment. The width of the test section was 80 mm and the span-wise hole separation was $\delta z/d$=4. As a staggered hole arrangement was used, the plate allowed four lateral hole rows. Test plates with three different injection angles, 15°, 20° and 30°, and three different stream-wise hole spacings of $\delta x/d$=3, 6 and 12, were manufactured in teflon. One steel test plate was also made, with an injection angle of 30° and hole spacing of $\delta x/d$=6, see table 2.1 on the preceding page. The holes were drilled using a fixture. Teflon has a coefficient of thermal expansion of $16{\cdot}10^{-5}$ K^{-1}, whereas steel has a much lower coefficient of thermal expansion, $1{\cdot}10^{-5}$ K^{-1} (see table 2.2). As the expansion of the teflon plates is quite large, they were made shorter than the steel plate. This allowed the teflon plates to expand ∼11 mm in the stream-wise direction for a 100°C temperature increase and 700 mm–long test plates.

Chapter 3

Wall temperature measurement technique

The first step in this project was to measure wall temperatures, which is the most important quantity in effusion cooling. A number of different techniques were first considered, such as thermocouples and liquid crystal thermography. Liquid crystals are difficult to calibrate and can not withstand temperatures above approximately 120°C, and were therefore not used. Thermocouples suffer from poor spatial resolution and are difficult to attach exactly to the wall surface. Infrared thermography was chosen because of its reasonably good spatial resolution, and the digital output can easily be archived and processed in a computer. A disadvantage is that the temperature, emissivity and reflectivity of the surrounding surfaces must be measured accurately to obtain reliable wall temperatures.

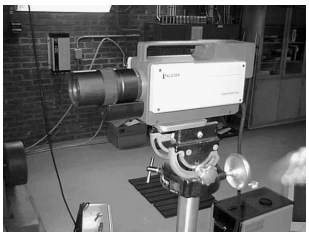

An AGEMA THV 900 LW (8 μm to 12 μm) system was used in the experiments, see the figure at the side. A thermograph was taken when one of the lids was quickly removed. A sapphire window was used at first instead of the lid. This concept had to be abandoned because static electricity made dust particles stick to the glass, which affected the transmissivity. An advantage of not using a sapphire window was that no correction of the measured wall temperature owing to emission from the hot sapphire was needed. As sapphire is not transparent in the long wavelength band, it would have been necessary to use a SW (3 μm to 5 μm) infrared camera. No change in the wall temperature could be observed on a short time scale when a lid was removed. This was investigated by recording the procedure on video and using line scanning. In line scanning mode, the vertical scanning mirror

in the camera is still, and it is possible to scan at 2.5 kHz.

As the whole test plate could be covered with six thermographs, a complete mapping of the test plate was made. The six corrected thermographs overlapped each other by approximately 1 mm. An algorithm for stitching them together was constructed, resulting in seamless joints. The absolute value of the differences in temperature and differences in temperature gradients in the overlapping areas was minimized.

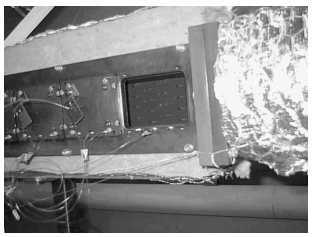

The surface of the test plates was coated with NEXTEL velvet coating. Due to the high emissivity, 0.96, in the 8 to 12 μm band, reflections from the hot surrounding walls were reduced. The temperature of the surrounding walls was measured with thermocouples, which were mounted in the side walls and in the lids. The thermocouples were mounted in cavities drilled from the outside. The wall thickness at the bottom of the cavities was only about 0.1 mm, assuming the temperature at the thermocouple position to be very close to the wall temperature. The side walls and lids were made of steel and painted with NEXTEL coating. An insulating layer on each side of the test section made heat losses small. The error in measured wall temperature caused by a temperature gradient is thus small. The error in the measured side wall temperature is $\pm 0.4\%$ (in the 133°C to 350°C range) for type T thermocouples, plus the instrument error of ± 0.5°C, according to the manufacturer. At 200°C, the total error in the thermocouple reading would be ± 1.3°C.

3.1 Wall temperature correction algorithm

As the test plates were cooled, the surrounding walls were hotter than the test plate. Reflections from the hot surroundings were subtracted from the intensity read by the infrared camera to obtain the true wall temperature. The corrected temperature of the wall, T_1, was computed as

$$T_1 \approx \left(\frac{T_{IR}^4}{\epsilon} - \frac{\rho^D}{A_1} \sum_{i=1}^{n} F_{i1} A_i T_i^4 \right)^{1/4} \tag{3.1}$$

where T_{IR} is the temperature read by the infrared camera with the emissivity, ϵ, set to 1.00. A derivation of this expression is given in appendix B on page 119. Some approximations were made, e.g. diffuse emissivity, and only one diffuse reflection was considered as the diffuse reflectivity is very

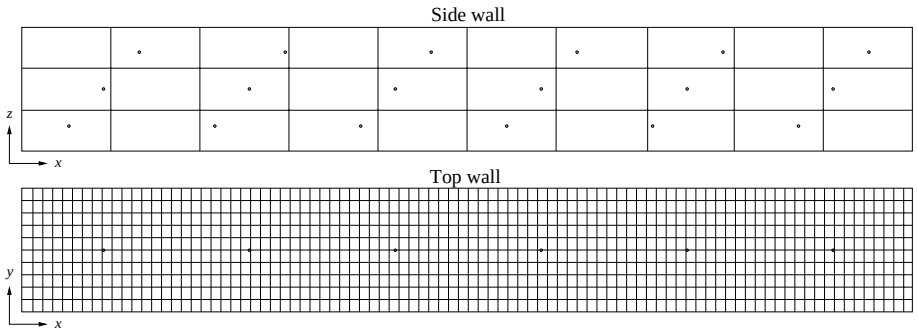

Figure 3.1: The computational mesh used in the wall temperature correction algorithm. Mesh size 90×10 on the top wall and 10×3 on the side walls. The temperature data from the infrared camera were placed on a 136×272 mesh at the bottom wall for each lid location. The dots denote the thermocouple positions.

low (≈ 0.02). In the wall temperature correction algorithm, the side walls were split into cells, see figure 3.1. It was assumed that the emissivity, reflectivity and temperature were constant in each cell. The mesh size was 90×10 on the top wall and 10×3 on the side walls. Temperature data from the infrared camera were placed on a 136×272 mesh at the bottom wall at each lid location. The inlet wall and outlet wall were approximated by one cell each. The measured side wall and top wall temperatures were used to create an interpolating function. This function set the temperature in each computational cell. The following interpolation function was used for the side walls (*N.b.* the coordinate system is defined as in figure 3.1)

$$T = c_1 + c_2x + c_3y + c_4xy + c_5x^2 + c_6y^2 + c_7x^2y. \tag{3.2}$$

The top wall temperatures were interpolated with the function

$$T = c_1 + c_2x + c_3x^2. \tag{3.3}$$

An example of the correction of the surface temperature is shown in figure 3.4. It is shown that the temperature correction is only a few degrees Celsius. A careful examination of the figure will reveal six darker areas and five lighter ones, see also figure 3.3 on the following page, which shows the irradiated heat flux. The darker areas correspond to the central part of the lid locations, where the surface has greater exposure to the relatively cool laboratory hall.

3.2 Wall temperature error estimate

An error estimate of the measured temperature was derived and is given in equation 3.4 on page 17 and in appendix B on page 119. Specular reflec-

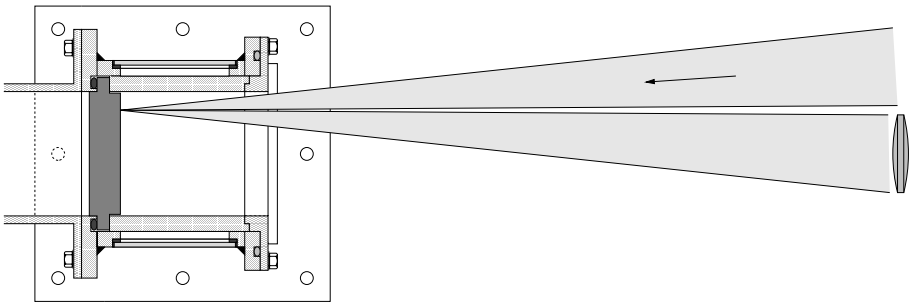

Figure 3.2: Specular reflections from the side walls may occur in the small area closest to the wall.

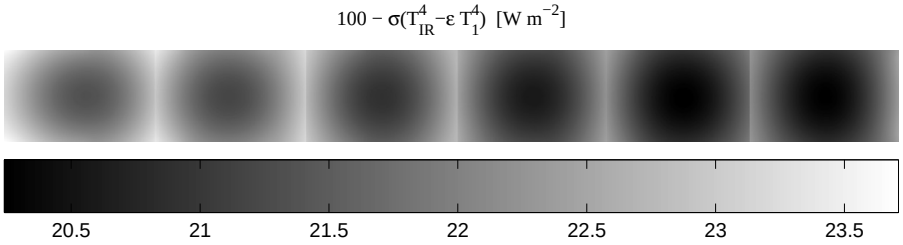

Figure 3.3: The irradiated heat flux, $\frac{\epsilon\rho^D}{A_1}\sum_i F_{i1}A_iT_i^4$, for case 100 is plotted.

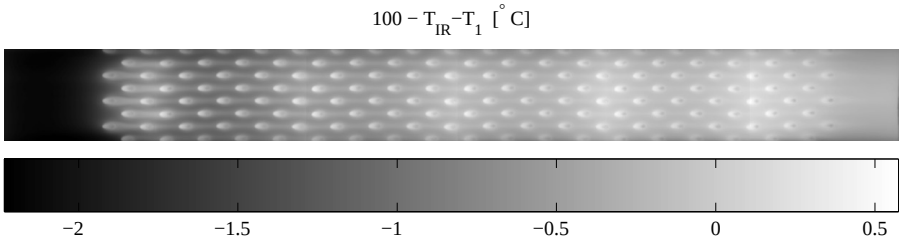

Figure 3.4: The difference in uncorrected temperature, T_{IR}, and the corrected temperature, T_1, for case 100 is plotted.

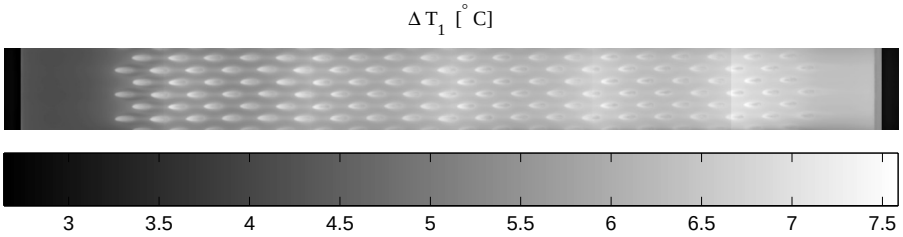

Figure 3.5: Example of a result from the error estimate calculations. The plot shows ΔT_1 [°C].

tions occurred only close to the side walls, see figure 3.2 on the preceding page. The estimate is valid if $\Delta T_1/T_1$, $\Delta T_{IR}/T_{IR}$ and $\Delta T_i/T_i$ is small compared to unity, see appendix B.

$$
\begin{aligned}
|\Delta T_1| \approx & \left| \left(\frac{T_{IR}}{T_1} \right)^3 \frac{\Delta T_{IR}}{(\epsilon + \Delta\epsilon)} \right| + \\
& + \left| \frac{\rho^D \epsilon}{T_1^3 (\epsilon + \Delta\epsilon) A_1} \sum_{i=1}^{n} F_{i1} A_i \Delta T_i T_i^3 \right| + \\
& + \left| \frac{\rho^D \Delta\epsilon + \epsilon \Delta\rho^D}{4 (\epsilon + \Delta\epsilon) T_1^3 A_1} \sum_{i=1}^{n} F_{i1} A_i \left(T_i^4 + 4 \Delta T_i T_i^3 \right) \right| . \qquad (3.4)
\end{aligned}
$$

In the temperature error estimate calculations, ΔT_{IR} was, according to the manufacturer of the infrared camera, $\pm 1\%$ of the range, which equals ± 2.5°C in our case. ΔT_i was ± 1.3°C, as specified before, and $\Delta\rho^D$ and $\Delta\epsilon$ were 0.02, resulting in an additional error of about 2°C.

An example of the error estimate of calculations of T_1 is shown in figure 3.5. The conclusion made from these calculations is that approximately half of the contribution to the error of the measured wall temperature comes from the error in the infrared camera reading and the other half from the uncertainty in the values of the emissivity and reflectivity of the walls and temperature of the surrounding walls. It should be mentioned that the error (about 2.5°C) in the temperature reading of the infrared camera is probably constant or changes monotonically with temperature. This implies that differences in temperature readings between different plates or different positions are smaller and amount only to about half the error of typically 5 K.

3.3 Calculation of view factors

The computation of the correction of the temperatures involves view factors, F_{ij}. In the computations, the surrounding area is split up into a large number of rectangular cells. The exchange of radiation is between rectangles with a perpendicular orientation with respect to the side and end walls and between rectangles with a parallel orientation with respect to the top side of the test section. The side walls are in direct contact with the investigated plates and, in the corners, the variation in the direction of the radiated beams, β_i and β_j, across the cell areas can not be neglected. Rather elaborate formulas for the view factors must be used for this case, as given in appendix A on page 115. The situation is simpler when considering the top side of the test section, since, in this case, the direction between the radiating cell areas is always large and the direction of the radiation beam can be considered constant for each point of cells. In the latter case, the view factor can be written as

$$A_i F_{ij} = \int_{A_j}\int_{A_i} \frac{\cos(\beta_i)\cos(\beta_j)}{\pi r_{ij}^2} dA_i dA_j \approx \frac{\cos(\beta_i)\cos(\beta_j)}{\pi r_{ij}^2} A_i A_j. \qquad (3.5)$$

This approximation is valid if the variation in r_{ij}, $\cos(\beta_i)$ and $\cos(\beta_j)$ is small within A_i and A_j. As areas A_i and A_j were small compared to r_{ij}^2 in this case, the simplification was justified, see figure 3.6 on page 20.

3.4 Infrared camera

The infrared camera had a spatial resolution of 1.5 mrad (see table 3.1 on the next page, where the relevant properties of the infrared camera are given) which, at the focusing distance used in the experiments, yielded a spatial resolution at 50% modulation of 0.75 mm. The diameter of the injection holes was 5 mm. The camera covered approximately 8.7 mm with 136 lines. Thus one injection hole was covered by approximately 8.5 pixels, but only 6.7 different temperature readings at 50% modulation could be made.

3.5 Emissivity measurements

The emissivity of the NEXTEL coating was measured at the Swedish Defence Research Agency FOI (former FOA) and at the Ångström laboratory at the University of Uppsala using an integrating sphere. Measurements of

Scanner	**900 LW**
Detector type	Mercury Cadmium Telluride
Spectral response	(8 to 12) μm
Frame frequency	15 Hz or 30 Hz
Line frequency	2.5 kHz
Lines/frame	136
Spatial resolution at 50% modulation	
- elements/line	230
- mrad at 20° FOV (field of view)	1.5
Samples/line	272
Measurement performance	
Temperature range	-30°C to 1500°C
Sensitivity at 30°C	0.08°C
Accuracy	$\pm$ 1°C or $\pm$ 1% of range
Repeatability	$\pm$ 0.5°C or $\pm$ 0.5% of range
Dynamic range	12-bit (4096 levels)
Lens	
Field of view (H$\times$V)	20° $\times$10°
Minimum focus distance	0.5 m
Spatial resolution at 50% modulation	1.5 mrad

Table 3.1: Technical specifications of the infrared camera, AGEMA THV 900 LW, according to the manufacturer.

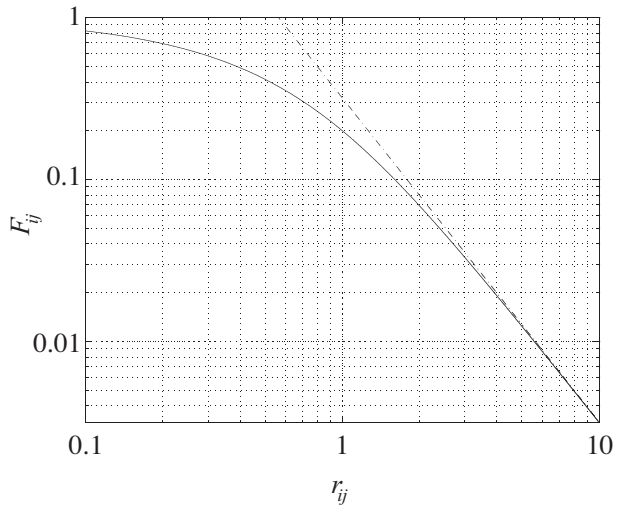

Figure 3.6: Comparison between the analytically calculated view factor, F_{ij}, between two parallel opposite unit squares and the numerical approximation (denoted by a dashed/dotted line). In the experiments, the top cells are $\sim$1 cm^2 and the separating distance is 8 mm. The difference between the analytical and approximate view factor at r_{ij}=8 is very small.

the emissivity were also made in this project with the THV 900 system. An aluminum can was painted with NEXTEL coating and an insulating layer was wrapped around it, except for a small area where the measurements were made. The can contained hot water of 70°C to 80°C and was well stirred. A Pt-100 RTD was used to measure the ambient room temperature, T_{amb}, which was approximately 23°C and the temperature of the hot water, T_{H_2O}, with an accuracy of $\sim \pm 0.2$°C. As the aluminum wall was very thin ($\sim$0.1 mm), its surface temperature is estimated to be within ± 0.05°C of that of the hot water. A thermograph was taken with emissivity set to 1.00, which gives T_{meas}. The emissivity of the surface was calculated as

$$\epsilon = \frac{T_{meas}^4 - T_{amb}^4}{T_{H_2O}^4 - T_{amb}^4}. \tag{3.6}$$

This method is estimated to give an accuracy in ϵ of ± 0.02. The main source of error in the ϵ determination is the temperature reading with the infrared camera (± 1°C is assumed). All three independent measurements estimated the emissivity to be 0.96. The Ångström laboratory estimated the diffuse part of the reflection to be 0.02. The emissivity of old paint used in the experiments and of new paint was checked. A small section of a used test plate was painted with fresh paint. No change in emissivity caused by degradation or soiling could be observed.

Chapter 4

Dimensional analysis

The surface temperature distribution is a function of the parameters from the governing equations and the boundary conditions. In order to extract only the most relevant dimensionless variables we consider here an idealized case, see figure 2.4 on page 10, where the injection plate (which in the experiments is the test plate) is infinitely long and infinitely wide and the main gas stream extends to infinity in the direction perpendicular to the injection plate. The basis for the analysis is the continuity, momentum and energy equations in their general compressible form and the energy equation for the conduction in the injection plate together with the appropriate boundary conditions. Some of the boundary conditions are given in figure 2.4. In addition to these, the fluid velocity must be zero on a solid wall and the temperature and heat flux must be continuous across a solid fluid interface. One thing to be noted here is that we must not specify the inlet density of the hot mainstream gas because the two gas streams must have the same pressure (apart from a small difference due to the pressure loss in the passage of the injection holes). The ideal gas law, assumed to hold here for the gas, thus gives

$$\rho_0 = \rho_c \frac{T_0}{T_c}. \tag{4.1}$$

We choose here to use U_c, T_c, ρ_c and d as primary scaling variables. In addition, we assume all material properties of the fluid and wall material to be constant. Appendix C on page 123 presents a more elaborate analysis, in which the details of the geometry of the test section are included, as is the variation with temperature in the material properties of the fluid and in the wall material. In a real case, thermal radiation, curvature effects, high free-stream turbulence levels, rotation, external pressure gradients and the presence of different gases, e.g. combustion gases, with different

material properties may have to be included in the analysis, but this is not done here.

The radiative heat transfer may not be negligible in a real case. An analysis in which radiation in its most general form is taken into account is also presented in C.9 on page 132.

The dependent variable in which we are interested here is the surface temperature of the injection plate. Since we have chosen T_c as a primary scaling variable, we get

$$T_w^\star = \frac{T_w}{T_c} \tag{4.2}$$

where the star, $\star$, from now on denotes a dimensionless variable. The dependence of this dimensionless variable is to be determined as a function of the set of independent variables as found in our dimensional analysis. These are given in appendix C on page 123 and in the following.

4.1 Primary dimensionless groups

From the expression for dimensionless viscosity, eq. C.26 on page 129, we have

$$\frac{\mu_c}{\rho_c U_c d} = \frac{1}{Re_c} \tag{4.3}$$

where Re_c is the Reynolds number.

From the expression for dimensionless thermal conductivity of the fluid, eq. C.27 on page 129, we have

$$\frac{\lambda_c T_c}{\rho_c U_c^3 d} = \frac{1}{(\kappa - 1)\, Ma_c^2\, Re_c\, Pr_c} \tag{4.4}$$

where Pr_c is the Prandtl number, Ma_c is the Mach number and κ is the specific heat ratio. From the dimensionless equation of state, eq. C.25 on page 128, we have

$$\frac{RT_c}{U_c^2} = \frac{1}{\kappa\, Ma_c^2}. \tag{4.5}$$

From the dimensionless specific heat at constant pressure, eq. C.30 on page 129, we have

$$\frac{T_c c_{p_c}}{U_c^2} = \frac{1}{(\kappa - 1)\, Ma_c^2}. \tag{4.6}$$

Finally, from the expression for dimensionless thermal conductivity of solid, eq. C.33 on page 129, we have

$$\frac{T_c \lambda_{s,ref}}{\rho_c U_c^3 d} = \frac{1}{(\kappa - 1)\, Ma_c^2\, Re_c\, Pr_c} \frac{\lambda_{s,ref}}{\lambda_c}. \tag{4.7}$$

In addition to these parameters emerging from the basic equations, we have from the dimensionless boundary conditions

$$\frac{b}{d} \qquad \frac{\delta x}{d} \qquad \frac{\delta y}{d} \qquad \frac{x_{off}}{d} \qquad \alpha$$

and the ratios of velocity and temperature

$$\frac{U_0}{U_c} \qquad \frac{T_0}{T_c}.$$

4.2 Secondary dimensionless groups

The temperature dependence of viscosity and thermal conductivity can be approximated with Sutherland's law, eq. C.26 on page 129 and eq. C.27 on page 129. These expressions give the parameters S_μ/T_c and S_λ/T_c. If these are small compared to unity, the gas behaves like an ideal gas. In the energy equation for the solid test plate, eq. C.32 on page 129, ρ_s/ρ_c appeared, but this ratio is significant only in a non-stationary case. The equations for the linear temperature dependence for c_p, c_{p_s} and λ_s, i.e. eq. C.30, eq. C.31 and eq. C.33, respectively, on page 129 gave the following dimensionless parameters

$$\frac{T_c^2\left(\frac{\partial c_p}{\partial T}\right)_c}{U_c^2} \qquad \frac{T_c c_{p_{s,ref}}}{U_c^2}$$

$$\frac{T_c^2\left(\frac{\partial c_{p_s}}{\partial T}\right)_{ref}}{U_c^2} \qquad \frac{T_c^2\left(\frac{\partial \lambda_s}{\partial T}\right)_{ref}}{\rho_c U_c^3 d}.$$

In a real case of a combustion chamber, radiative heat transfer may be important. This is not studied in these experiments.

4.3 Scaling of the experiment

Table 4.1 on the following page gives some examples of the conditions in a combustion chamber and in the experiment given. The experiment scales with the combustion chamber on all the primary variables. A better scaling of the thermal conductivity ratio, λ_s/λ_c, could have been achieved with stainless steel with $\lambda_s \approx$16 W/(m·K). Due to difficulties in the manufacturing process, no such plates were made. The values of λ_s in the experiment serve as two extreme cases of low and high thermal conductivity. To scale S_μ/T_c and S_λ/T_c properly, a different gas, such as an ideal gas, would have been necessary.

Dimensional variables	Combustion chamber	Experiment	Units
$\|U_0\|$	0-300	17-48	m/s
T_0	1300-1850	423-573	K
U_c	1-10	0.3, 0.5, 0.7	m/s
U_{jet}	$\leq \|U_0\|$	~ 5 - ~ 50	m/s
T_c	$\sim$700	300	K
p_0	1.5-4	0.101	MPa
ρ_0	2.8-11	0.62-0.83	kg/m^3
ρ_c	7.5-20	1.2	kg/m^3
c_{p_c}	$\sim$1140	1005	J/(kg·K)
μ_c	$\sim 3.3 \cdot 10^{-5}$	$1.9 \cdot 10^{-5}$	Pa· s
λ_c	$5 \cdot 10^{-2}$	$2.66 \cdot 10^{-2}$	W/(m·K)
λ_s	$\sim$30	0.5 and 45	W/(m·K)
d	0.5-1.5	5	mm
b	0.8-2	20	mm
δx	3-12	15-60	mm
δz	5	20	mm
Dimensionless groups	**Combustion chamber**	**Experiment**	
$\frac{\rho_c U_c d}{\mu_c}$	110-9000	97-225	
$\frac{\lambda_c T_c}{\rho_c U_c^3 d}$	1.2-9300	3900-50000	
$\frac{\lambda_s T_c}{\rho_c U_c^3 d}$	720-5.6 $\cdot 10^6$	73000-940000, (6-80)$\cdot 10^6$	
$\frac{R T_c}{U_c^2}$	(0.02-2)$\cdot 10^5$	(1.76-9.6)$\cdot 10^5$	
$\frac{c_{p_c} T_c}{U_c^2}$	(0.08-8)$\cdot 10^5$	(6.2-34)$\cdot 10^5$	
U_{jet}/U_c	0-300	7-167	
U_0/U_c	0-300	24-160	
T_0/T_c	1.86-2.64	1.4-1.9	
λ_s/λ_c	$\sim$600	$\sim$19, $\sim$1700	
S_μ/T_c	0.16	0.37	
S_λ/T_c	0.28	0.65	
$\delta x/d$	2-24	3-12	
$\delta z/d$	3.3-10	4	
b/d	0.5-4	4	
α	$\sim$30°-90°	15°-30°	

Table 4.1: Scaling of the experiments. The combustion chamber values serve only as an example.

Chapter 5

Results

Figure 5.1 on the next page and figure 5.5 on page 30 show the surface temperature distribution, T_w/T_c, for three different velocity ratios, U_0/U_c. A unique number is associated with each thermograph, which can be used to correlate T_w/T_c in figures 5.2 on page 27 to 5.13 on page 39. Table 2.1 on page 11 lists all experimental parameters for the thermographs in this thesis. The top thermograph in figure 5.1, in which U_0/U_c is large, shows attached jets, resulting in streaks of low temperature. There is a decrease in temperature in front of the first row of holes resulting from heat conduction in the plate. This effect becomes more pronounced as the velocity ratio is reduced. The test plates were made of teflon with a very low heat conductivity in order to come as close as possible to an adiabatic case and to be able to see the interesting features of the temperature distribution. However, we can see in all cases, from figure 5.1 to figure 5.13, that there is a considerable effect of the conductive heat transfer in front of the holes. The middle thermograph in figure 5.1, with somewhat lower U_0/U_c, also shows streaks of low temperature with two hot areas behind the injection holes. This is an indication that hot air is swept down behind the cold jet by a side vortex in the mean velocity field. In the bottom thermograph in figure 5.1, which represents the case with the lowest velocity ratio, U_0/U_c, the area behind the injection holes is heated and there are no streaks of low temperature. This is consistent with the idea of fully separated jets, and hot fluid is advected around the jet and reaches the wall with an increased wall temperature as a result. Even streaks of elevated temperature behind the injection holes are visible. The effect is increased some rows downstream, where different vortices may interact. For the lowest velocity ratios, the surface temperature upstream of the first row of holes is lower than in the case with higher velocity ratios. This might be a consequence of less convective heat transfer owing to a larger blockage effect. The im-

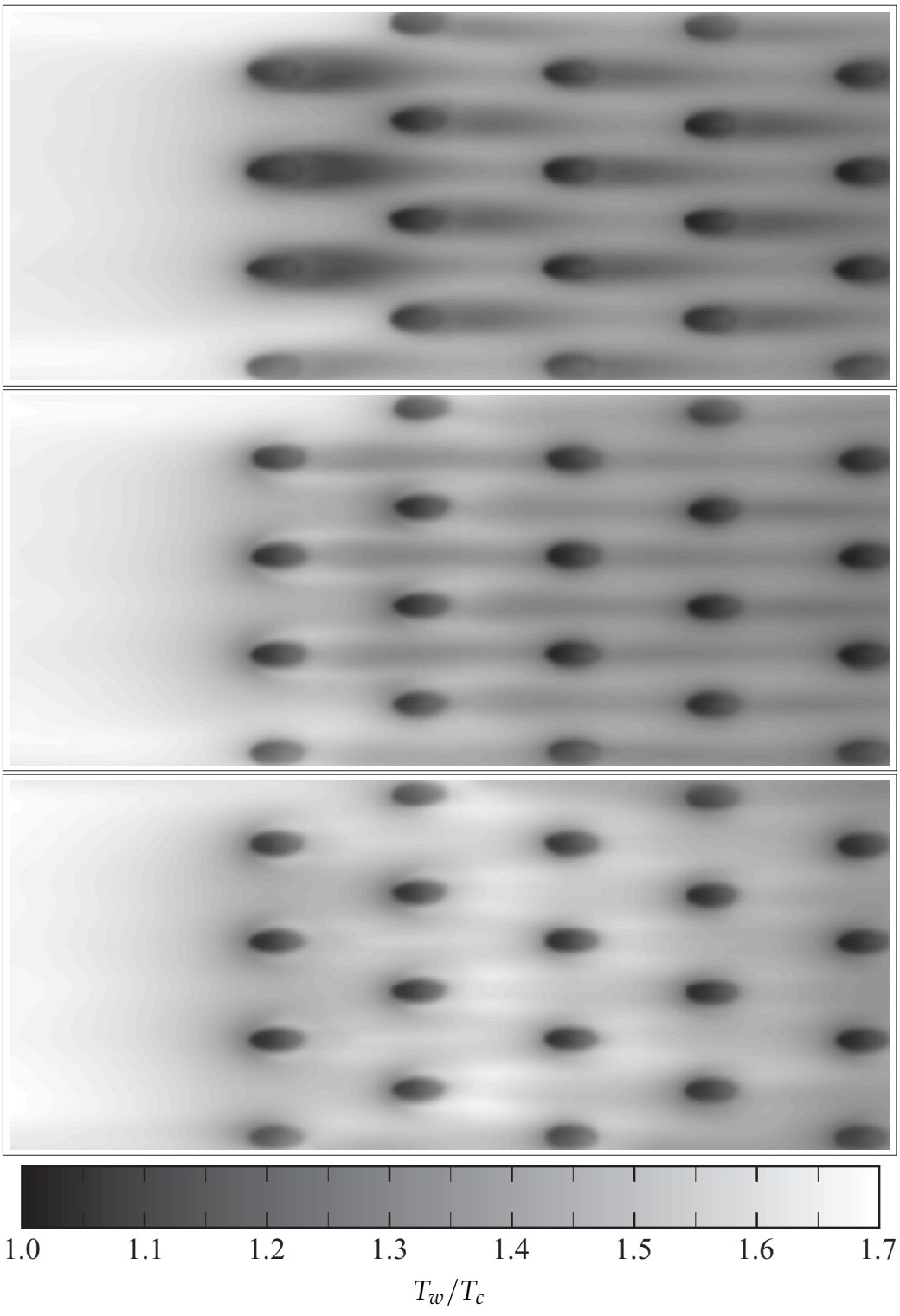

Figure 5.1: Close-ups of the first rows of holes for teflon plates with T_0/T_c=1.78, Re_c=150, $\delta x/d$ =6, α=30°. A variation in U_0/U_c is made, from the top U_0/U_c={91, 60, 34}. (Reprinted with the permission of ASME.)

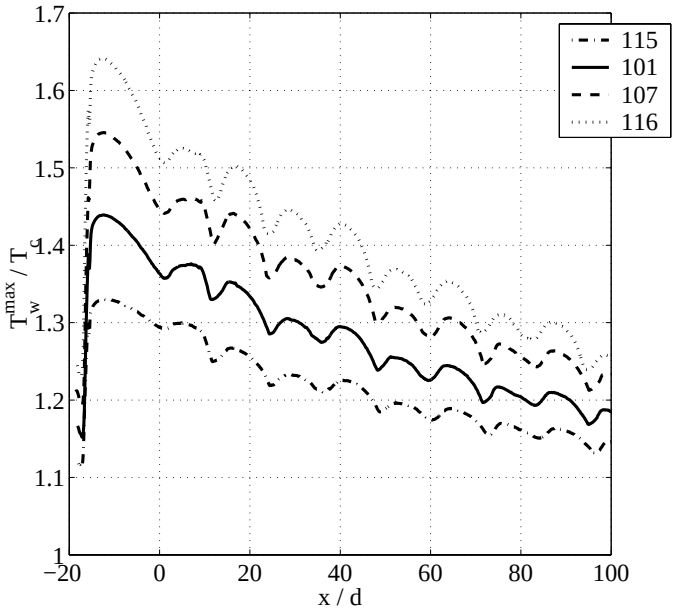

#	T_0/T_c
115	1.42
101	1.56
107	1.71
116	1.84

Figure 5.2: The effect of T_0/T_c for a teflon plate where U_0/U_c=140, Re_c=100, δx =12, α=20° and $n = 44$. (Reprinted with the permission of ASME.)

portance of the different parameters is discussed below. From figure 5.2 to figure 5.13, the maximum surface temperature, T_w^{max}/T_c, in the span-wise direction, z, is given for each x value. The T_w^{max}/T_c parameter is the most important to the lifetime of the cooled parts. Temperature gradients in the plate may also be important to the lifetime. Note that a position x/d=0 corresponds to the leading edge of the injection hole in the first row.

5.1 Effects of the temperature ratio

A higher mainstream temperature, T_0/T_c, gives a higher surface temperature, T_w/T_c, as expected. Figure 5.3 on the following page shows three examples of how the maximum span-wise temperature ratio, T_w^{max}/T_c, increases with T_0/T_c. Linear curve fits with error estimates of the predictions (50% of the estimated points are within the band) are also plotted. We see that the relationship is approximately true and can be represented by

$$\frac{T_w^{max}}{T_c} = (1 - \eta_w^{max}) \cdot \left(\frac{T_0}{T_c} - 1 \right) + 1. \tag{5.1}$$

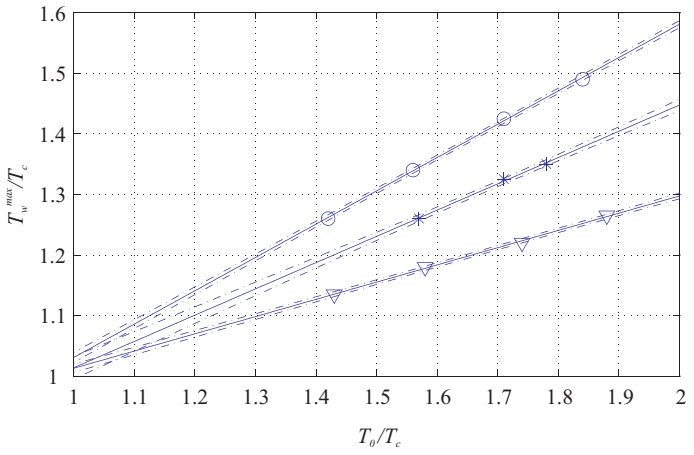

Figure 5.3: The maximum span-wise temperature ratio, T_w/T_c versus T_0/T_c, for three teflon plates at $x/d = 20$. ◯ U_0/U_c=140, Re_c=100, $\delta x/d$ =12 and α=20°. ⋆ U_0/U_c=59, Re_c=151, $\delta x/d$ =6 and α=30°. ▽ U_0/U_c=58, Re_c=90, $\delta x/d$ =3 and α=20°. (Reprinted with the permission of ASME.)

Rewriting this, we see that η_w^{max} is a film cooling effectiveness parameter.

$$\eta_w^{max} = \frac{T_0 - T_w^{max}}{T_0 - T_c} \tag{5.2}$$

Bazdidi-Tehrani & Andrews (1994) reported a weak dependence of T_0/T_c on the film cooling performance. Figure 5.4 on the next page shows that the dependence of T_0/T_c on film cooling effectiveness appears to decrease as U_0/U_c is decreased. Although not shown here, this observation holds for all the investigated cases.

When T_0/T_c increases, the density ratio ρ_0/ρ_c decreases. This will probably affect the jet lift-off and the relative decrease in enthalpy of the hot crossflow. Figure 5.4 also shows that the film cooling effectiveness increases as the temperature ratio increases. This effect is more pronounced at high velocity ratios. It should be mentioned that the temperature of the cooling air was nearly constant throughout the experiment, so that the variation in Re_c is due only to a variation in U_c. The effect of temperature dependence on the viscosity and thermal heat conductivity is included in the T_0/T_c parameter.

5.2 Effects of the velocity ratio

An increase in the amount of cooling air corresponds to a reduction in the U_0/U_c parameter. This can have a great effect on the surface temperature,

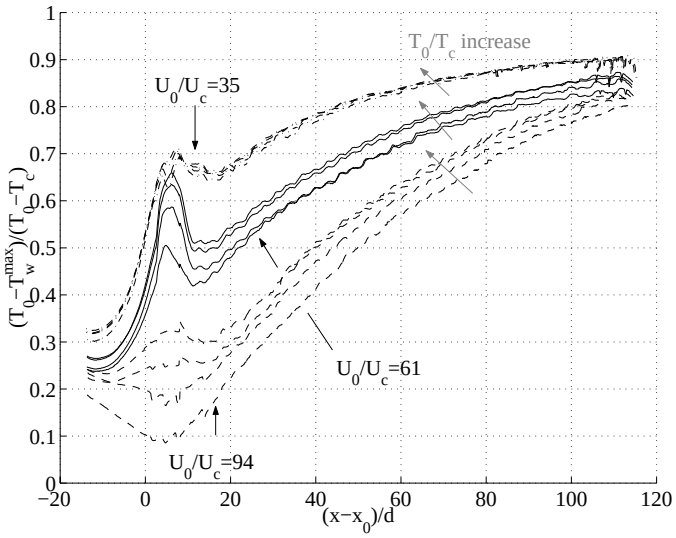

Figure 5.4: The film cooling effectiveness, η_w^{max}, based on the maximum spanwise temperature ratio, T_w/T_c, versus T_0/T_c. Teflon plate with Re_c=148, $\delta x/d$ =3, α=30° and n=156. (Reprinted with the permission of ASME.)

as shown in figure 5.6 on page 31. In this case, the hole spacing is small and the jet speed is thus low (recall that U_c measures the cooling air speed in the plenum chamber and not the velocity of the jet). There is no cooling film for the first rows for the largest U_0/U_c, and the surface temperature is not reduced. The cooling air is distributed only in the downstream holes, probably owing to the pressure drop in the test section, see figure 5.6 on page 31. This is an important aspect when designing cooling systems fed from a single plenum, as described by e.g. Salcudean *et al.* (1994). When the mainstream velocity is reduced, cooling air is distributed in upstream rows, causing an effective decrease in temperature. With a more sparse hole spacing, the jet speed is higher for the same U_0/U_c. The change in cooling effect will not be as pronounced as before, see figures 5.7 on page 32 and 5.8 on page 33. For these cases, the jet penetrates into the mainstream and cooling air is distributed in all holes.

5.3 Effects of the Reynolds number

The Reynolds number, Re_c, has a small effect on the surface temperature at downstream positions on the test plates with $\delta x/d$ =6 and $\delta x/d$ =12, considering a variation in this parameter of about two times, see figure 5.9 on page 34. For the plates with $\delta x/d$ =3, there is a significant difference

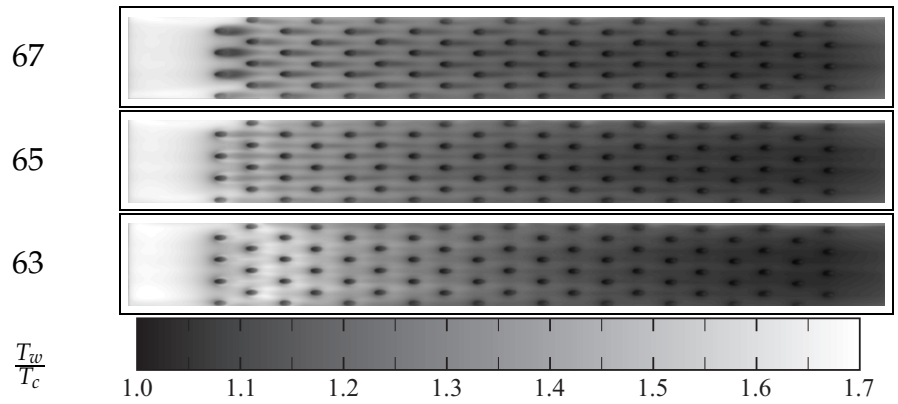

Figure 5.5: The effect of different velocity ratios, U_0/U_c, is shown in thermographs of a teflon plate where T_0/T_c=1.78, Re_c=150, $\delta x/d$ =6, α=30° and n=80. A variation in U_0/U_c is made, from top U_0/U_c={91, 60, 34}. (Reprinted with the permission of ASME.)

at upstream positions, see figure 5.10 on page 35. There seems to be an increase in temperature after the first row of holes in the cases with low Re_c, which is also clearly seen in figures 5.9 and 5.10. The variation in Re_c is caused only by a variation in U_c, as mentioned in the section covering the T_0/T_c effect.

5.4 Effects of the stream-wise hole spacing

The stream-wise hole spacing, $\delta x/d$, has a major effect on the surface temperature, see figure 5.11. A dense hole spacing, $\delta x/d$, generally gives a low T_w/T_c, if enough cooling air is supplied. The near transpiration cooling situation of low $\delta x/d$ seems to drastically reduce the surface temperature, also reported in Bazdidi-Tehrani & Andrews (1994). Higher $\delta x/d$ gives rise to larger oscillations in the temperature profiles in figure 5.11, i.e. larger temperature gradients. For the same U_0/U_c, the plates with dense spacing will have lower jet velocities and more attached jets as compared with those that are sparsely spaced. The drastic increase in available surface for convective heat transfer inside the wall may also explain the large effect. Foster & Lampard (1980) reported increased film coverage and less jet lift-off when the span-wise hole spacing, δz, was decreased.

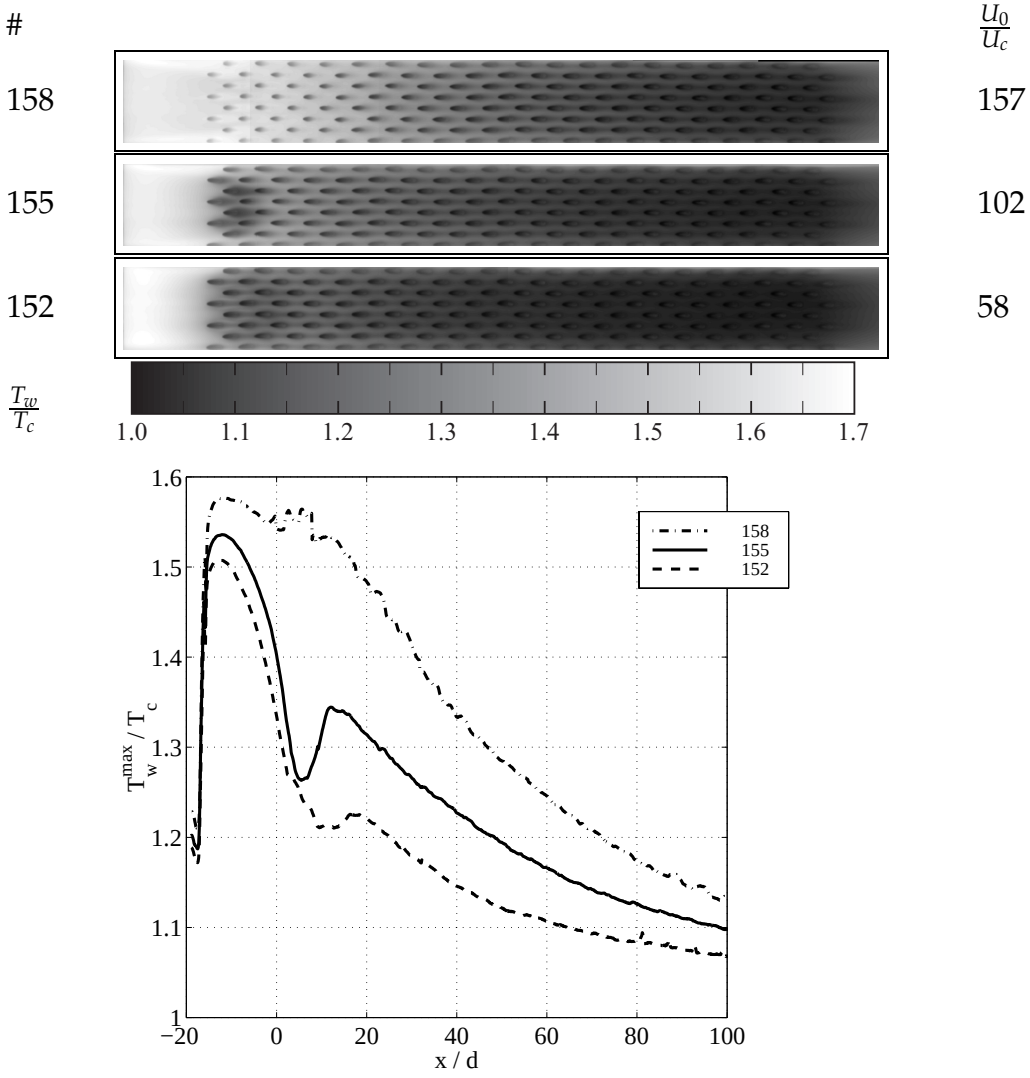

Figure 5.6: The effect of different velocity ratios, U_0/U_c, is shown in thermographs of a teflon plate where T_0/T_c=1.7, Re_c=90, $\delta x/d$ =3, α=20° and n=156. A variation in U_0/U_c is made, from top U_0/U_c={157, 102, 58}.

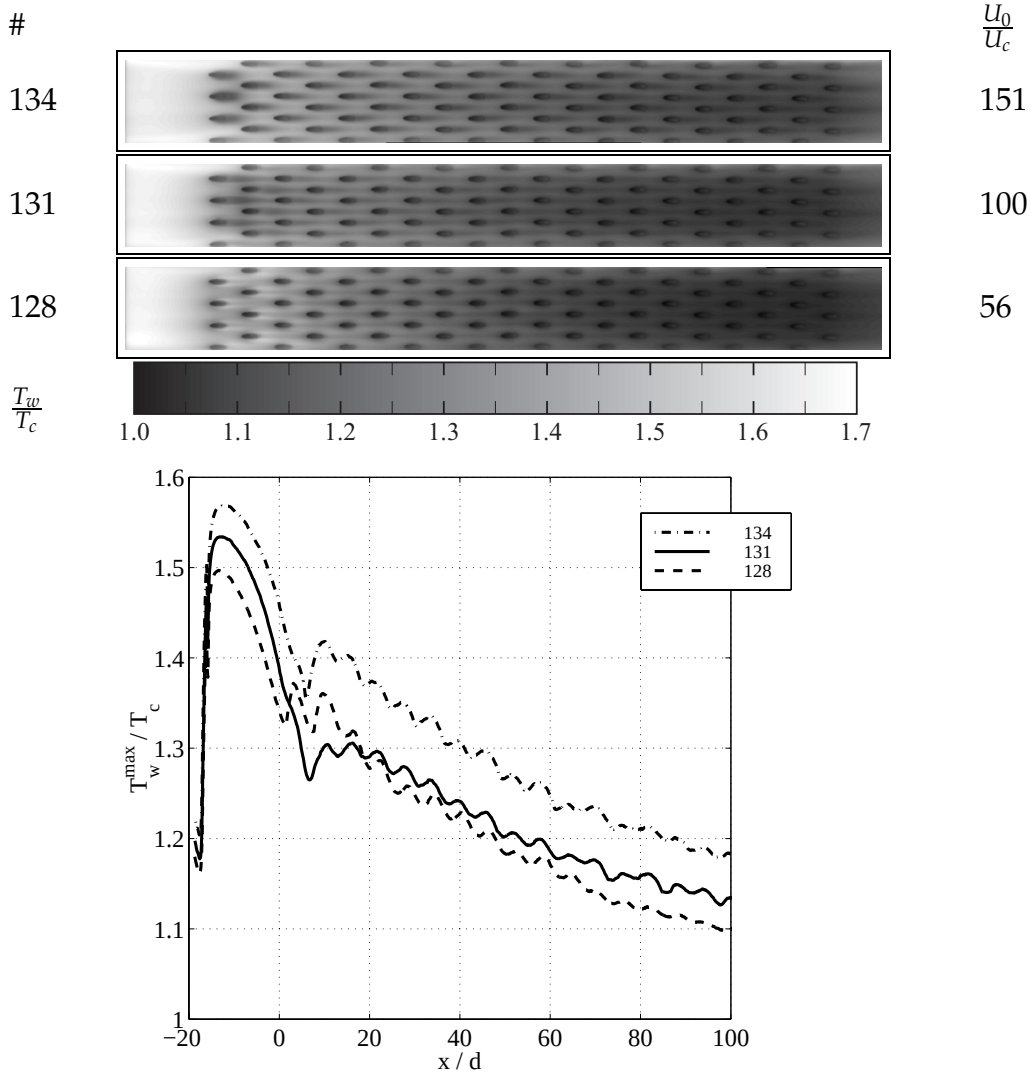

Figure 5.7: The effect of different velocity ratios, U_0/U_c, is shown in thermographs of a teflon plate where T_0/T_c=1.7, Re_c=92, $\delta x/d$ =6, α=20° and n=80. A variation in U_0/U_c is made, from top U_0/U_c={151, 100, 56}. (Reprinted with the permission of ASME.)

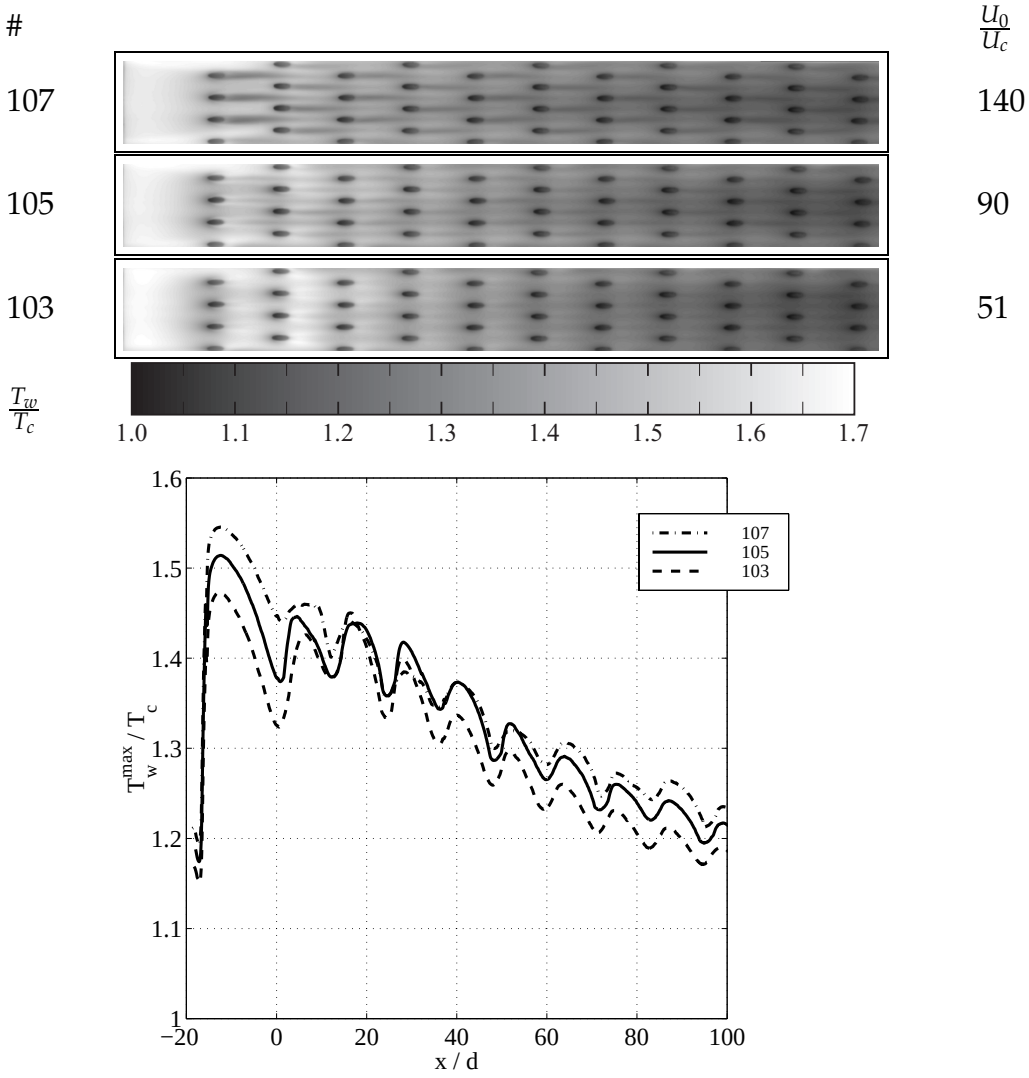

Figure 5.8: The effect of different velocity ratios, U_0/U_c, is shown in thermographs of a teflon plate where T_0/T_c=1.7, Re_c=100, $\delta x/d$ =12, α=20° and n=44. A variation in U_0/U_c is made, from top U_0/U_c={140, 90, 51}. (Reprinted with the permission of ASME.)

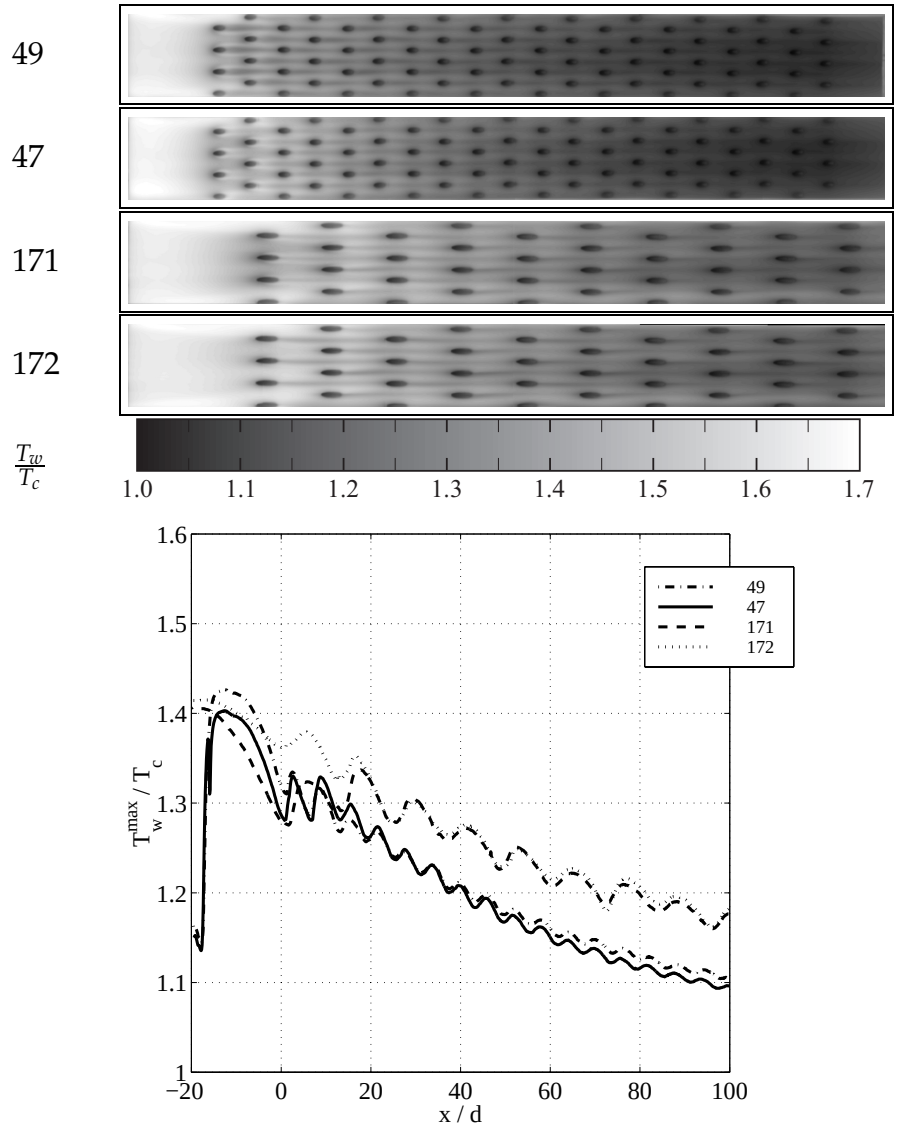

49:	Re_c=153	U_0/U_c=59	$\delta x/d$ =6	α=30°	n=80
47:	Re_c=87	U_0/U_c=59	$\delta x/d$ =6	α=30°	n=80
171:	Re_c=88	U_0/U_c=100	$\delta x/d$ =12	α=15°	n=40
172:	Re_c=138	U_0/U_c=96	$\delta x/d$ =12	α=15°	n=40

Figure 5.9: The effect of different Reynolds numbers, Re_c, is shown in thermographs of a teflon plate where T_0/T_c=1.53-1.59. (Reprinted with the permission of ASME.)

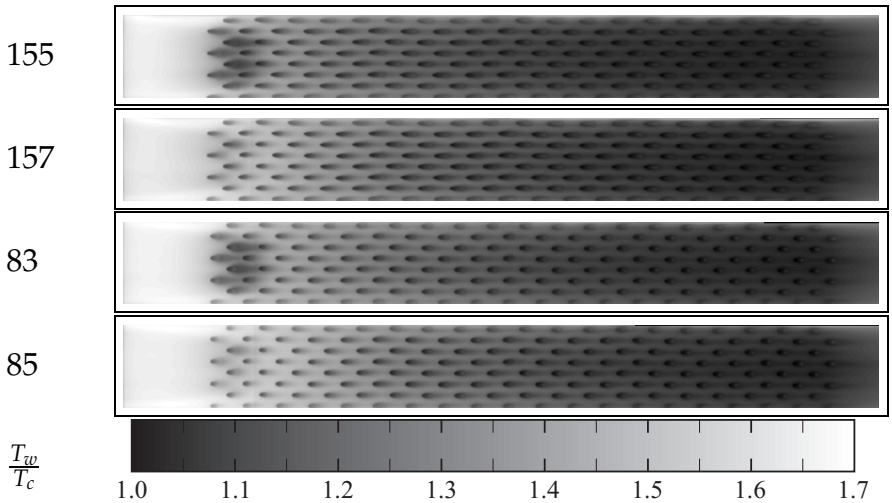

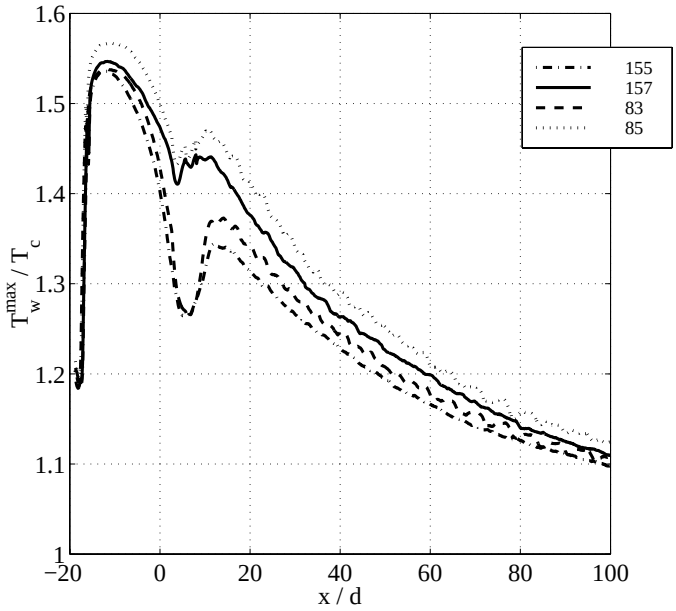

155: Re_c=90 U_0/U_c=102 $\delta x/d$ =3 α=20° n=156
157: Re_c=147 U_0/U_c=94 $\delta x/d$ =3 α=20° n=156
83: Re_c=88 U_0/U_c=103 $\delta x/d$ =3 α=30° n=156
85: Re_c=146 U_0/U_c=94 $\delta x/d$ =3 α=30° n=156

Figure 5.10: The effect of different Reynolds numbers, Re_c, is shown in thermographs of a teflon plate where T_0/T_c=1.7. (Reprinted with the permission of ASME.)

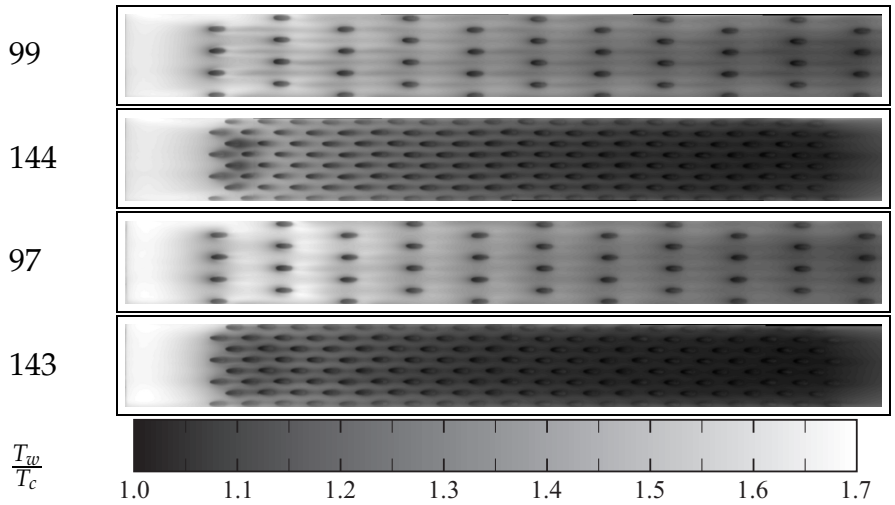

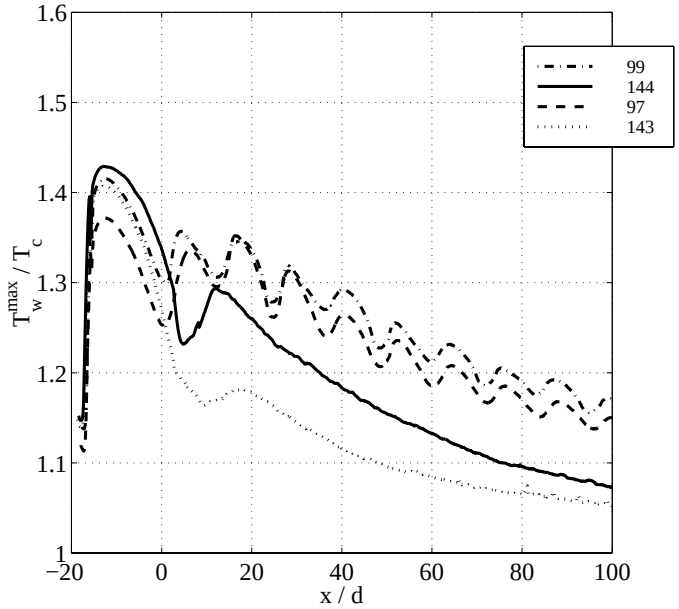

99: Re_c=97 U_0/U_c=91 $\delta x/d$ =12 α=20° n=44
144: Re_c=91 U_0/U_c=102 $\delta x/d$ =3 α=20° n=156
97: Re_c=97 U_0/U_c=52 $\delta x/d$ =12 α=30° n=44
143: Re_c=91 U_0/U_c=58 $\delta x/d$ =3 α=30° n=156

Figure 5.11: The effect of different stream-wise hole spacings, $\delta x/d$, is shown in thermographs of a teflon plate where α=20° and T_0/T_c=1.56-1.58. (Reprinted with the permission of ASME.)

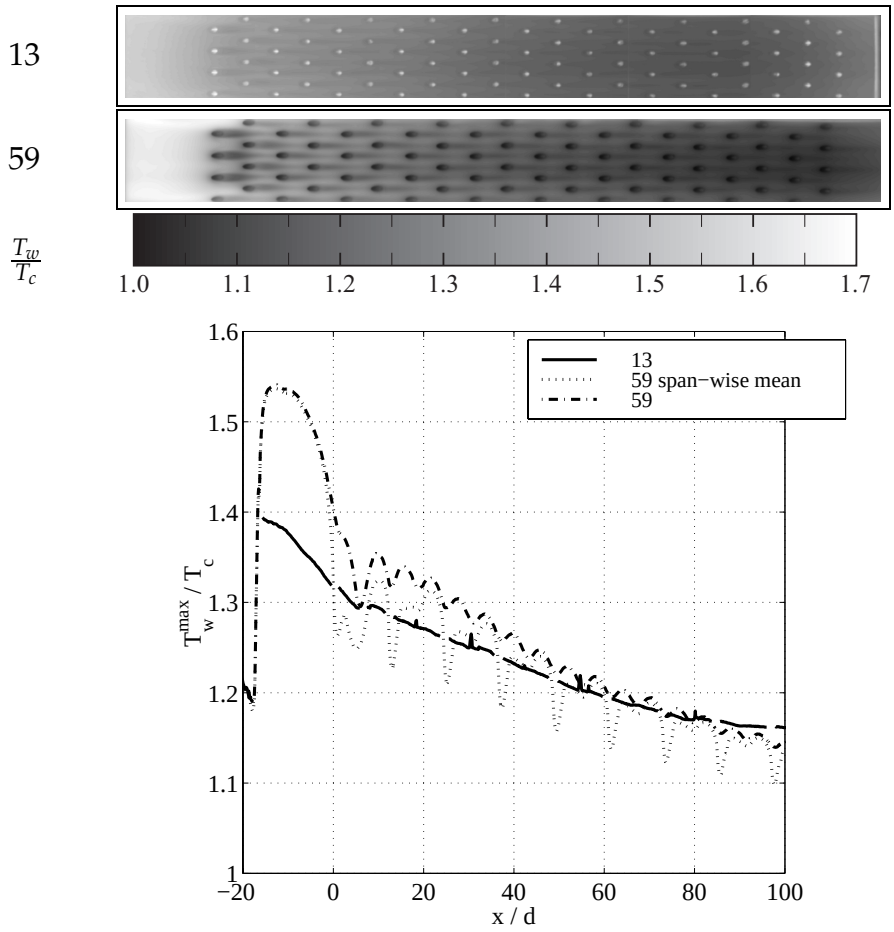

Figure 5.12: The effect of different heat conductivity ratios, λ_s/λ_c, is shown in thermographs of a teflon plate with λ_s/λ_c=1700 and $n = 84$ for the steel plate at the top and λ_s/λ_c=19 and n=80 for the teflon plate at the bottom; furthermore, $\delta x/d$ =6, α=30°, Re_c={91,94} U_0/U_c=100 and T_0/T_c=1.7. (Reprinted with the permission of ASME.)

5.5 Effects of the thermal heat conductivity ratio

The heat conductivity ratio, λ_s/λ_c, has an effect on the surface temperature, see figure 5.12 on the preceding page. Higher λ_s/λ_c gives smoother surface temperature profiles, i.e. smaller temperature gradients, and a lower temperature at the start of the effusion cooled plate. A variation in λ_s/λ_c does not seem to have a major influence on either the temperature at the end of the plate or on the mean span-wise temperature level. Note that the plates are supported at each end and that effects caused by heat conduction may be visible for the steel plate, which has a high thermal conductivity. It is necessary when making computations of effusion cooled walls to solve the conjugate heat transfer problem, as pointed out by Leontiev (1999).

5.6 Effects of the injection angle

The injection angle, α, has only a small effect on the surface temperature, see figure 5.13 on the next page. The plates with injection angles of 20° and 15° are somewhat better than the 30° injection hole plates. Shallower injection angles promote attachment of the jet to the wall but do not seem to reduce the overall surface temperature. LeBrocq, Launder & Priddin (1971) and Colladay & Russell (1976) reported that slanted jets stay attached to a higher degree. Low α values reduce the surface temperature of the $\delta x/d$ =3 test plates when U_0/U_c is large to a better extent than do high α values. It should be mentioned that the lengths of the injection holes are 8, 11.7 and 15.5 diameters for the 30°, 20° and 15° cases, respectively, if b/d=4. It is much more difficult to make a 15° injection hole than a 30° hole. It has been pointed out by Foster & Lampard (1980) and Goldstein & Stone (1997) that shallow injection angles give the highest effectiveness for low blowing rates and that steep injection angles perform better at higher blow factors because of increased vortex interaction. From a manufacturing point of view, it is advantageous to keep α as high as possible.

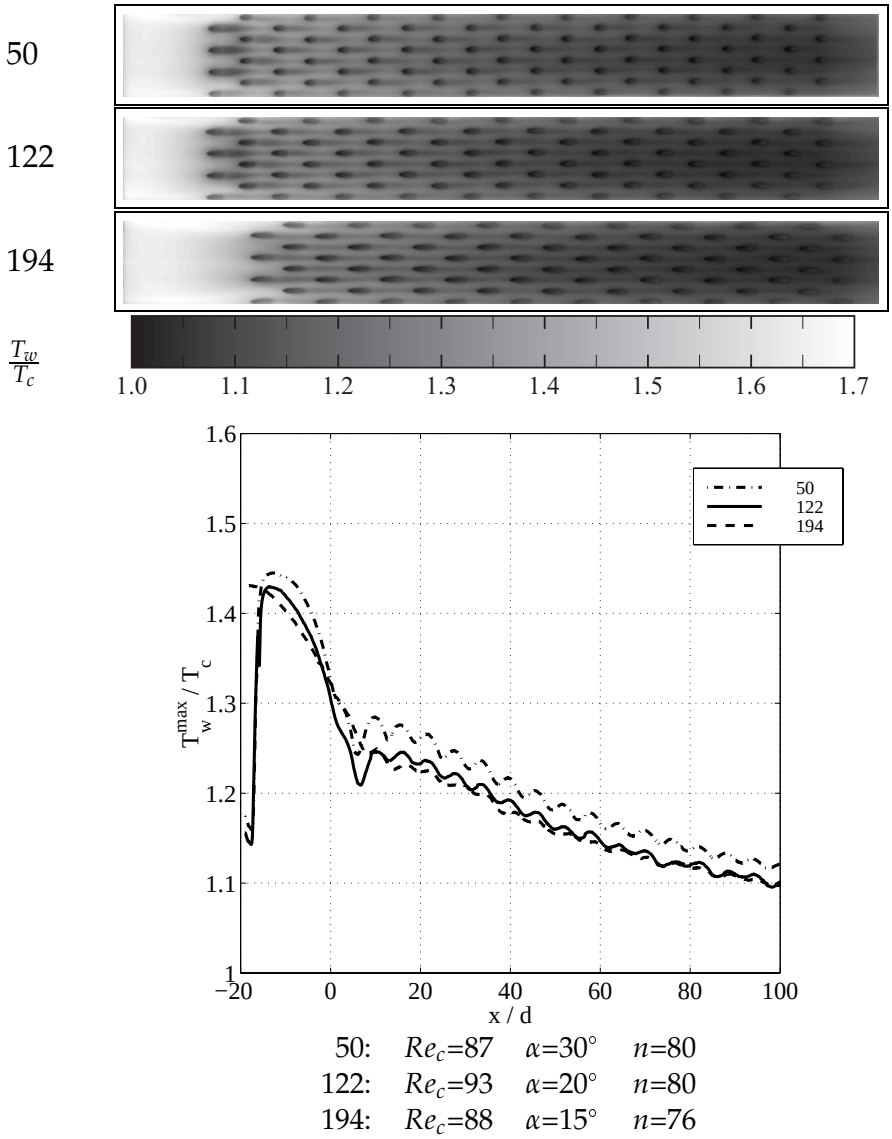

Figure 5.13: The effect of different injection angles, α, is shown in thermographs of three different teflon plates where U_0/U_c=100, $T_0/T_c = 1.58$ and $\delta x/d$ =6. (Reprinted with the permission of ASME.)

Chapter 6

Conclusions

A parametric study was made of 242 cases with different temperature ratios between hot and cold air streams, T_0/T_c, velocity ratios, U_0/U_c, Reynolds number, Re_c, stream-wise hole spacing ratio, $\delta x/d$, wall material heat conductivity ratio, λ_s/λ_c and injection hole angle, α.

1. Examination of thermographs shows a considerable effect of the conduction in front of the holes due to the blockage caused by the injected jets when U_0/U_c is low. Fully separated jets and hot fluid advected to the wall can also be observed. Even streaks of elevated temperatures behind the injection holes are seen for the low U_0/U_c cases.

2. The surface temperature distribution, T_w/T_c, seems to increase linearly with the temperature ratio, T_0/T_c, when the crossflow to jet velocity ratio is low.

3. For dense hole spacing with low jet speeds, the velocity ratio seems to have a large effect, causing uneven distribution of the cooling film. The U_0/U_c parameter seems to decrease in importance as $\delta x/d$ is increased (higher jet speeds and more uniform cooling film distributions).

4. The Reynolds number, Re_c, has a small effect in downstream positions, but an elevation in temperature was observed for the lowest Re_c after the first row of holes.

5. The closer to the transpiration cooling situation one gets, the better. A small $\delta x/d$ seemed to have a major effect when enough cooling air was supplied.

6. The heat conductivity ratio, λ_s/λ_c, did not seem to change the temperature in the mean, except in front of the injection holes. The highest temperatures at the upstream part of the plate were reduced. Larger temperature gradients could of course be seen for low λ_s/λ_c.

7. The injection angle did not seem to have a major effect on the surface temperature. Low α gives somewhat lower temperatures; the 15° and 20° temperature profiles seem to coincide slightly below that of the 30° temperature profiles.

Part II

Velocity and turbulence field measurements

Chapter 7

Introduction

Modern gas turbines need efficient cooling of the combustion chamber walls, turbine blades and flame-holders. Effusion cooling, or full coverage film cooling, is a very powerful method used in combustion chambers. Cooling air, taken from the compressor stage, is injected at an angle to the crossflow through small holes in the wall. Thousands of holes are made in the wall, and a large fraction of the wall area is thereby exposed to the cooling air. The cooling air also dilutes the hot gas flow closest to the wall and thus reduces the temperature.

Past research on jets in crossflow have almost exclusively been focused on a single round jet issuing into the crossflow at a right angle to the wall. In effusion cooling, many jets are injected, and will interact and density effects are also important. This motivates a study of many rows of slanted jets issued into a crossflow. Furthermore, much of the data presented previously were 2D, and our knowledge of the topology of the true 3D mean velocity fields is thereby poor. Simultaneous measurements of all three velocity components in a large number of points in three-dimensional space are required to understand the effects of the flow field on the heat transfer to the wall. The mean velocity field itself brings about a good mixing of the coolant and the hot gas. This is obvious only in a 3D view of the flow field. The high turbulence levels found in the wake of a jet in crossflow also promote high heat transfer rates.

Another motivation for 3D measurements is the interesting features of a 3D flow separation event that were found in the wake of the jet in a preliminary (feasibility) study. A very complex flow field is created when the vortex from the 3D separation point interacts with a vortex generated on the sides of the injection hole. It is also interesting to study how these two vortices evolve downstream to create a counter-rotating vortex pair.

Bergles *et al.* (1976) studied the static and dynamic pressure in the

flow and the surface pressure distribution and made smoke visualizations, hot wire measurements and helium tracer concentration measurements (film cooling effectiveness) of a single perpendicular jet in crossflow for low blowing factors. Their conclusions were that flow reversal behind the jet could be found for U_{jet}/U_0 as small as 0.3. Furthermore, lower pressure was found in the wake than in front of the jet, associated with the deflection of the jet toward the wall. Bergles *et al.* writes "... that the satisfactory prediction of the flow and cooling effectiveness behind row of holes depends crucially on predicting correctly the detailed structure of the flow in the immediate vicinity of the holes". This is the primary motivation for the work described in this part of the thesis.

Colladay & Russell (1976) executed streak line visualizations of four slanted round jets in crossflow. The injection holes were drilled in a diamond pattern. The operational and design parameters in that study were close to the ones in the present study (parameters in this study in parenthesis): U_{jet}/U_0=0.8 (0.89), Re_{jet}=2165 (5800), $\delta x/d$ =5 (6), $\delta z/d$ =5 (4), b/d=2.6 (4) and α=30° (30°). They concluded that the injection angle should be as shallow as possible to decrease jet separation.

Moussa *et al.* (1977) and Eiff & Keffer (1997) investigated a single jet in crossflow issuing from a skirted pipe (cf. a smoke stack). Moussa *et al.* report rapid stretching and tilting of vorticity vectors near the injection. They further conclude that the turbulent vorticity is of the same order of magnitude as the mean vorticity at the pipe exit. Eiff & Keffer used a pattern recognition technique with multi-point hot wire probes to study the vortex shedding phenomenon and its coherent structures.

Foss (1980) made flow visualizations and surface oil streak visualizations of a single perpendicular jet in crossflow. Topological maps and dye streak images are presented for several velocity ratios.

Yavuzkurt *et al.* (1980a & 1980b) report on three-component hot wire measurements of full coverage film cooling flowfields under isothermal conditions with a 30° injection and blow factors, $\rho_{jet}U_{jet}/\rho_0U_0$, of 0.4 and 0.9. They did not experience flow reversal behind the jet for a mass flux ratio of 0.4.

Andreopoulos & Rodi (1984) made hot wire measurements of the flow field surrounding a single jet in crossflow issuing at a right angle to the wall. Small stream-wise gradients of streamwise velocity were found on the lee side of the jet. A low pressure region in the wake caused a motion toward the center plane and a vertical deflection of the jet. The inward motion of crossflow fluid led to a wall jet-type layer with high velocity. A counter-rotating vortex pair downstream of the jet injection was found for U_{jet}/U_0 =0.5. The turbulence measurements showed that the turbu-

lent kinetic energy, $\frac{1}{2}\overline{u_i u_i}$, and the Reynolds shear stress, $\overline{uv}$, are closely associated with $\partial U/\partial y$. The $\partial W/\partial z$ gradient was also important, but only at locations with a strong stream-line divergence or convergence. The $\overline{uw}$ shear stress was found to be related to $\partial U/\partial z$ and $\partial W/\partial y$. Finally, the $\overline{vw}$ shear stress was related to $\partial V/\partial z$ and $\partial W/\partial y$.

Coelho & Hunt (1989) presented an invicid vortex sheet model for the generation of the trailing vortices and the deflection of a single orthogonal jet in crossflow. They considered a two-dimensional cylindrical vortex sheet in the pipe. They suggested that pressure gradients, induced by the crossflow, generate axial and transverse vorticity in the pipe. Vorticity become concentrated to the wake position, which makes the vortex sheet kidney-shaped. The inclusion of turbulent entrainment in the model gave a deflecting jet.

Pietrzyk *et al.* (1990) measured vertical and stream-wise velocity components of a single row of injection holes by means of the LDA technique. The operational parameters were U_{jet}/U_0 =0.5 and ρ_{jet}/ρ_0=2. One of their findings was that the locations at which $\partial\overline{U}/\partial y$ is high coincide with the locations at which $\overline{uv}$ is high, which implies that the production of $\overline{uv}$ is primarly due to $\partial\overline{U}/\partial y$.

Fric & Roshko (1994) report smoke visualizations and present discussions on the origin of vorticity in the wake of the jet in crossflow. Adverse pressure gradients on the downstream lateral sides were found to provoke 'separation events' in the wall boundary layer, causing the upright wake vortices.

Kelso *et al.* (1996) give a comprehensive description of the topology of the flowfield around a single orthogonal jet in crossflow. Dye streak visualizations and hot wire measurements in the center plane and in a near wall plane (y/d =0.42) at Re=6200 and U_{jet}/U_0 =2.2 are presented. A description is given of how vortex rings in the pipe appear to tilt and bend to contribute to the vorticity in the counter-rotating vortex pair. Examples of vortex breakdown were seen in the counter-rotating vortex pair at the pipe outlet. A phenomenological map is also presented for the (U_{jet}/U_0,Re) space.

Thole *et al.* (1997) made flow field measurements of a single jet injected at 30° to the crossflow using laser-Doppler anemometry. The velocity and the density ratios were unity. Measurements were made near the entrance of the injection hole, inside the hole, at the exit and in the interaction region. The presence of crossflow at the entrance affected the jet behavior at the pipe exit. Separation inside the injection hole on the windward side and on the leeward side was found for high and low entrance crossflow Mach numbers, Ma_c, respectively. High turbulence levels in the jet were

found for Ma_c=0 (u'/U_{jet} =16%) and Ma_c=0.5 (u'/U_{jet} =21%) and low turbulence levels were found for Ma_c=0.3 (u'/U_{jet} =11%), where prime denotes the RMS value. The peak turbulence level in the wake of the jet at x/d =2 was $(\overline{u^2}+\overline{v^2})^{1/2}/U_0/2$=28% for the low Mach number case, i.e. stagnant plenum, and for Ma_c=0.5 the maximum level was 36%.

Chapter 8

Experimental set-up and techniques

The operational parameters in this study were $T_0 = T_c$=24°C, U_0=17.5 m/s, U_{jet}=15.5 m/s and the experiment was conducted in air. This means that $Re_d = \rho\, U_0\, d/\mu$=5800, U_{jet}^{max}/U_0=0.89 (U_0/U_c=80). The origin of the coordinate system used in this section is at the center of one of the injection holes in the third row. Figure 8.2 on the following page shows the measurement mesh. The area investigated was x/d ={−1.2, 10}, y/d ={0.06, 2} and z/d ={0, 2}. Measurements were made in 57×31×20=35340 points. A mapping of the velocity field in a complete xy-plane (1767 points) was completed in two days. Everywhere in the measurement mesh, the step size between the measurement points in the y-direction increased exponentially from 0.02d to 0.145d. In the separation region immediately downstream of the injection hole, the step size in the x-direction was 0.04d; further downstream, it increased exponentially to about 1.1d. The step size in the x-direction above the injection hole was 0.2d. The step size in the z-direction was 0.04d close to the center plane and near the orifice of the pipe (near z/d =0.5); further out, it was 0.2d.

8.1 Wind tunnel and test plate

A small wind tunnel suitable for experiments on effusion cooled walls was built as described in section 2.1 on page 7. The wind tunnel consists of two closed loops a main loop and a secondary loop, see figure 8.1. A number of gauze screens and a metal honeycomb were mounted in the most upwind position of the inlet duct. This screen arrangement differs from the one used in part I.

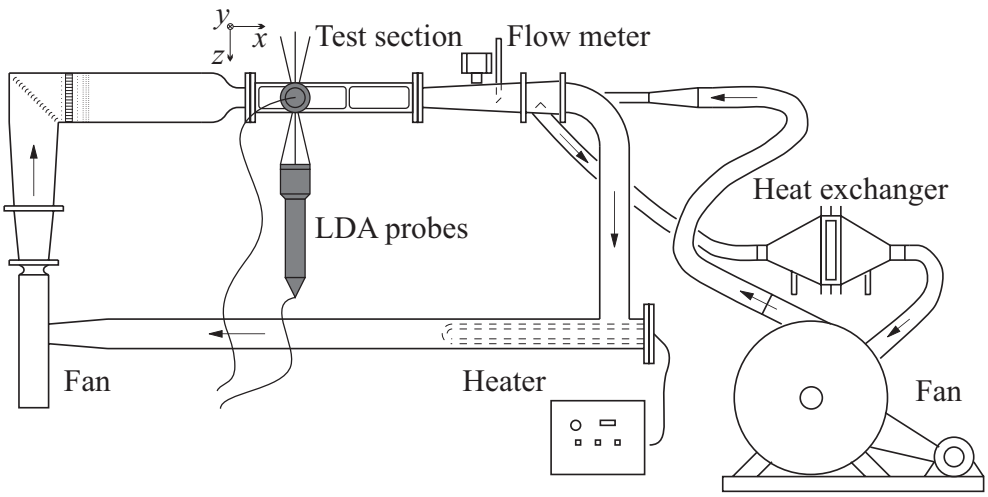

Figure 8.1: The wind tunnel and the LDA probes.

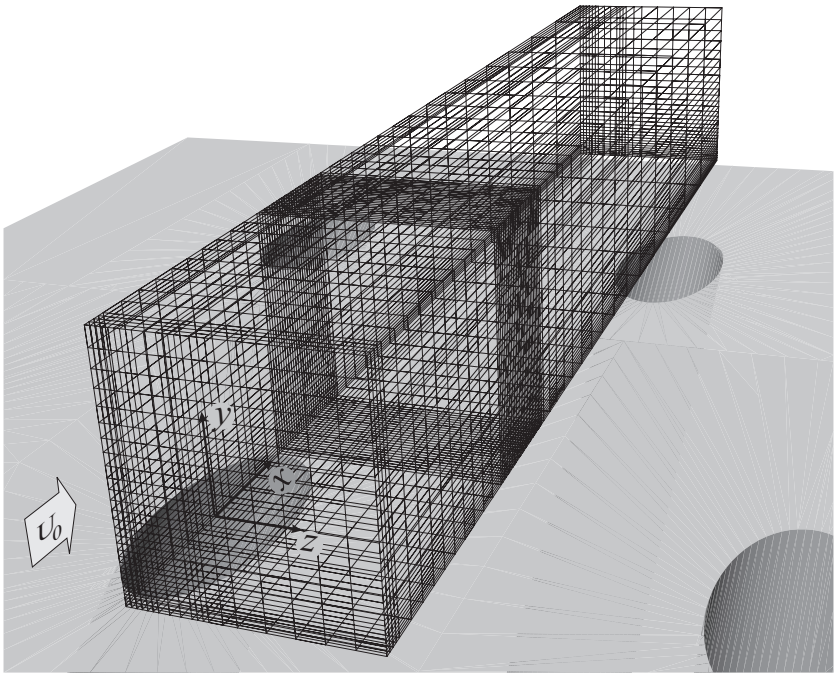

Figure 8.2: The measurement mesh at the third row of holes.

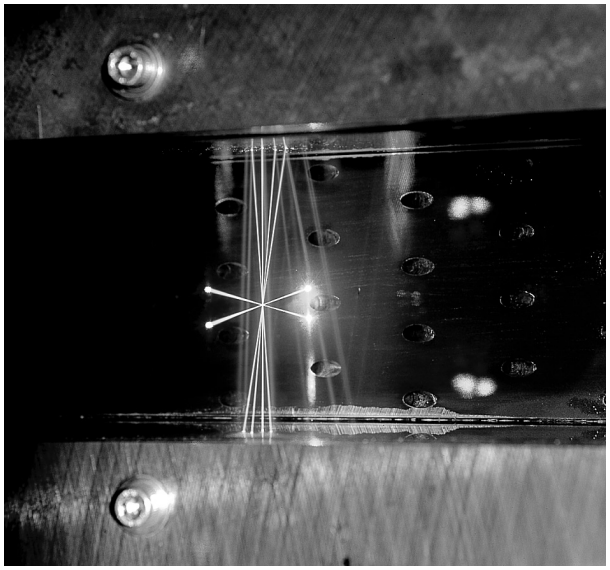

Figure 8.3: The photograph shows the three laser beam pairs of the LDA system.

The flow quality of the wind tunnel was investigated. The turbulence level in the free stream was 0.3% at the center of the test section above the studied injection hole according to LDA measurements. This number is quite low – a generally held opinion is that an LDA system does not usually measure lower turbulence levels than about 1% due to inherent noise. The free stream mean velocity variation was $\sim$ 0.5% (17.4 m/s–17.6 m/s) from experiment to experiment. The uniformness of the axial mean velocity across the inlet plane of the wind tunnel was 0.4%. A small swirl component, about 2% of U_0, was present near the wall. Efforts were made to eliminate this swirl by mounting different honeycomb and gauze screen arrangements in the inlet chamber. The problem was probably caused by the Görtler-type vortices originating on a concave section in the contraction. Owing to the design of the wind tunnel, this problem could not be dealt with during the limited time of this experiment.

The test plate was made of steel with a staggered injection hole arrangement, α=30°, $\delta x/d$ =6 and $\delta z/d$ =4. The injection hole diameter was 5.2 mm, see figure 2.4 on page 10.

8.2 Laser-Doppler anemometer

The laser-Doppler anemometer technique was chosen because of the small measurement volume obtainable and the possibility it offers of determin-

ing all three velocity components simultaneously. The hot wire technique will fail utterly in the jet in a crossflow situation with small scales, high turbulence levels, a high degree of three-dimensionality and reversed flow. The hot-wire technique is better suited to far field measurements. The literature has quite a few experiments on flows with a jet in crossflow using the LDA technique, e.g., Crabb *et al.* (1981), Pietrzyk *et al.* (1990) and Thole *et al.* (1997).

The LDA system worked in *side scatter* mode with three velocity channels. An Argon-ion laser was used and the 476 nm, 488 nm and 514.5 nm lines were used. The situation of the LDA system relative to the wind tunnel is shown in figures 8.1 on page 50 and 8.3 on the preceding page. A 310 mm front lens and a 1.94 beam expander was used. The laser beam diameter was 2.25 mm after the fiber, and thus the diameter of the measurement volume was 45 μm. The side scatter mode created an almost spherical measurement volume. An illustration of the size of the two overlapping measurement volumes is given in some of the figures, e.g. 9.18 on page 78 at $z/d = 0$ and y/d=-0.1. Note that the actual measurement volume is the intersection between the two ellipses. This gives a feeling of how small the measurement volume is compared to the injection hole (the wall is solid gray and the injection hole is the white space between) and compared to the variations in the velocity and the turbulence fields.

Three Dantec Burst Spectrum Analyzers (2 $\times$ 57N10 + 57N11) were used, working in burst mode and master coincidence mode on all three signal processors. In this mode, the Doppler burst signal is processed only when there is a signal on all three velocity channels simultaneously, which makes the post-process coincidence filtering a great deal easier. The spectrum analysers operated in 'one shot' mode, in which one complete memory buffer is filled with velocity data and then transferred to the computer. This allowed high data rates, above 1 kHz. The size of the memory buffer was 5000 samples, and that is the number of samples collected in each point. With a data validation of 90%-95%, this makes about 4500 valid samples in every point. This is a sufficient number of samples to obtain reliable first order statistical moments, whereas about ten times more samples are needed for accurate measurements of second order moments. A discussion concerning the number of independent samples is given in section 9.4.3 on page 85. It is shown there that the $\sim$4500 samples in each point are in fact independent samples.

8.2.1 Seeding

Scattering particles were added to the circulating air in the form of aerosol droplets from a smoke generator, SAFEX. The average diameter of the droplets is about 0.7 μm according to the manufacturer. They are thus small enough to follow the velocity fluctuations with high fidelity. The parameters that determine whether the particles can follow the velocity fluctuations are the density ratio between the fluid and the particle and the Stokes number, $[\mu/(\rho_f \omega d_p^2)]^{1/2}$. Durst *et. al* (1981) reported that silicone drops in air ($\rho_{oil}/\rho_{fluid} = 900$, which is close to the value of the aerosol used in this experiment) with a diameter of 0.8 μm have a relative amplitude response of 0.99 at 10 kHz. The corresponding response for 2.6 μm particles is at 1 kHz.

The seeding was also a motivation for choosing the operational parameter T_0/T_c=1. Aerosol particles are a suitable choice near room temperature. At elevated temperatures, solid particles such as SiC or TiO_2 must be used. With such particles, it is hard to reach high seeding levels, and thereby high data rates, as are required for the kind of extensive measurements that are presented here.

8.2.2 Alignment of the laser beams

Relevant principles of the LDA technique and useful formulas are given in appendix E on page 141. Section E.7 on page 155 shows the way in which the laser optics was adjusted.

To ensure good quality of the Doppler signal the crossing of all laser beams must take place at the focal point of the optical system receiving the scattered light. The alignment of the beams is usually made on an optical bench on which the probes are mounted in a holder. Laser light is fed backwards into the outlet end of the receiving fiber, and the location of the focal point is easily found using a small pinhole. The pinhole is adjusted in such a way that a maximum amount of light is transmitted through. If the lens package is not perfectly achromatic (low dispersive), laser beams with different wavelengths will focus at different locations. This is the case with the Dantec optics. A selection must be made of the focal point for the wavelength that is to be received by that specific probe. When the focus location has been found, all the laser beams are adjusted so that a maximum of light is transmitted.

The laser beams change their direction when refracted through the glass window of the test section. It is not certain that the best beam crossing is obtained when the laser probe is situated at the actual measurement

position with the adjustment from the optical bench. A better way to adjust the beam crossing is to put a 50 μm pinhole inside the test section and to make the adjustments *in situ*.

If a high temperature case had been investigated, it would have been necessary to use tempered glass with poor optical quality or quartz glass windows of the test section. Tempered glass has inherent stresses that can change the polarization of the laser beams. This is devastating to the laser-Doppler signal. The present test section has ordinary FLOAT glass (of good optical quality). An important problem to be solved, when making measurements with heated crossflow is that of the occurrence of phase differences where there is a change in refractive index owing to density gradients. These changes in phase will introduce noise in the signal (the location of the fringe pattern is changed).

8.2.3 Bias in LDA

Measurements using LDA can be biased when statistical quantities are computed. Even if each single sample is correct, the average may not be correct if proper averaging processes are not followed. Samples that are not statistically independent, or when the arrival of the seeding particles depends on the velocity field itself, bias the average. Section E.6 on page 153 describes several kinds of possible bias effects. The *velocity bias* was corrected by *transit time weighting* as described by George (1976). The side scatter mode creates a very small measurement volume and thus reduces the velocity gradient bias. It further makes near-wall measurements possible by reducing the scattered light from the wall. The test plate was painted with matte black NEXTEL velvet coating (the same as in the thermography measurements) and a fluorescent dye, *Rhodamine*, also helped to reduce wall reflections.

Chapter 9

Results and discussion

Section 9.2 to section 9.4.6 gives a kinematic description of the velocity field and its topology, the Reynolds stresses' fields and the vorticity fields of the investigated slanted jet in crossflow. Section 9.5 discusses the production of the Reynolds stresses. The pressure field is outlined in section 9.6, and the coupling between the velocity, Reynolds stresses and vorticity fields are also given in that section. The next section offers a short introduction to flow topology.

9.1 Introduction to topology

Three-dimensional flow fields can be very difficult to understand from two-dimensional pictures. There are topological tools, e.g. the concept of *critical points*, that facilitate the interpretation of plane drawings once the tools are understood. With some training it is possible to extrapolate the information from the 2D figures into 3D space. For a more complete description of critical points in flow fields, see Perry & Chong (1987) and Chong *et al.* (1989).

Critical points

In a general instantaneous velocity field, $u_i(\mathbf{x}_i, t)$, there may be points at which the slope of a streamline is indeterminate. Points at which all the spatial derivatives of u_i are zero are called *critical points* of u_i. The streamlines in the immediate vicinity of a critical point can be described by a linearization of the instantaneous velocity, u_i, around the critical point;

$$u_i = a_i + a_{ij}x_j + \ldots + H.O.T. \tag{9.1}$$

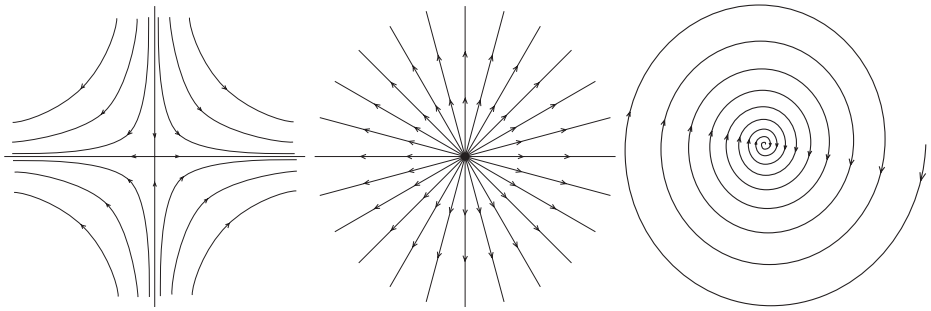

(a) Saddle point (b) Unstable node point (c) Stable focus point

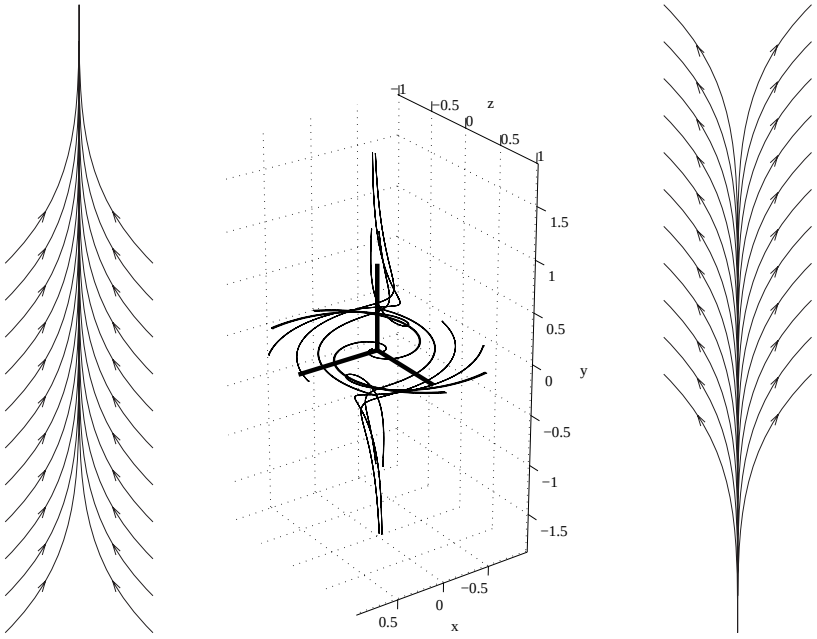

(d) NBL (e) Focus in 3D (f) PBL

Figure 9.1: Figures (a) through (c) show three different kinds of critical points. In (e) a focus with one real and two complex conjugate eigenvalues $\lambda_1 = 0.5$, $\lambda_{2,3} = 0.5 \pm i$, is drawn. Figure (d) shows a negative bifurcation line, i.e. a *separation line*, and figure (f) a positive bifurcation line, i.e. an *attachment line*.

where $a_{ij} = \partial u_i / \partial x_j$ is the rate of the deformation tensor (the sum of the rate of strain tensor, S_{ij}, and the rotation tensor, Ω_{ij}) and x_i is the space coordinate with its origin at the critical point. Note that a_i is zero. The behavior near the point of linearization is governed by the nature of the rate of the deformation tensor, a_{ij}, i.e. by its eigenvalues, λ, and eigenvectors. The eigenvalues of a_{ij} can be computed by the characteristic equation:

$$\lambda^3 + P\lambda^2 + Q\lambda + R = 0 \tag{9.2}$$

where $P = -\text{tr}[a_{ij}]$, $Q = 1/2(P^2 - \text{tr}[a_{ij}^2])$ and $R = -\text{det}[a_{ij}] = 1/3(-P^3 + 3PQ - \text{tr}[a_{ij}^3])$. If one eigenvalue is real and the other two a conjugate complex pair, a focus is seen. When all three eigenvalues are real, a saddle point-type of critical points is seen in two planes, and a node point is seen in the third plane, if the flow is incompressible. If the flow is compressible, Nodes in all three planes are possible. The three types of critical points for a plane are shown in figure 9.1.

The term *vortex* is often used without formal definition. Chong *et al.* (1989) defined regions with complex eigenvalues as belonging to a vortex core and claimed that streamlines will spiral around an axis that is at rest relative to the observer. Whether or not a bundle of vortex-lines is a vortex depends on the amount of perpendicular irrotational rate of strain to which it is subjected, i.e. whether or not the eigenvalues are complex. A different criterion of a vortex is given by Jeong & Hussain (1995). They define a region to belong to a vortex core when the median eigenvalue of $\mathbf{S}^2 + \mathbf{\Omega}^2$, denoted λ_2, is negative. This ensures that *two* eigenvalues of $\mathbf{S^2} + \mathbf{\Omega^2}$ are negative and a local minimum in pressure due to vortical motion occurs. A kinematic vorticity number, $||\mathbf{\Omega}||/||\mathbf{S}||$, which is zero for irrotational flow and infinite for solid body rotation, has also been introduced in the literature.

For a flow field to be kinematically possible, there can only be a certain number of saddle points for a given number of node points. According to the Poincaré-Bendixson theorem, there can only be two more node points than saddle points on a sphere. Hunt *et al.* (1978) gives a relation for a two-dimensional section of the flow

$$\left(\sum N + \frac{1}{2}\sum N'\right) - \left(\sum S + \frac{1}{2}\sum S'\right) = 1 - n, \tag{9.3}$$

where $\sum N$ is the sum of the nodes and the foci, $\sum N'$ is the sum of the half-nodes (nodes on the boundaries), $\sum S$ is the sum of the saddles, $\sum S'$ is the sum of the half-saddles (like stagnation points on the boundaries) and n is the connectedness of the surface. For a surface with obstacles and no holes, n is 1; if there is one hole in the surface, n is 2 etc.

An *attachment line* or positive bifurcation line, see figure 9.1, is a line on a surface (can occur within the fluid away from boundaries) from which streamlines are repelled. Owing to continuity, the fluid must be replaced, and this is accomplished by streamlines in the wall normal plane attaching to the surface. In the same way, a *separation line* or negative bifurcation line, is a line to which streamlines are asymptotically attracted. The continuity also is fulfilled in a similar way near a separation event.

9.2 Mean velocity field

Kelso *et al.* (1996) reported a topological map of the velocity field of a single jet emanating ortogonally into a crossflow at high velocity ratios. A very complex 3D field was found; in front of the jet, several horse shoe vortices were visible, while in the wake several critical points, such as foci, nodes and saddle points, were present. In the experiment described here, a less complex flow field was found but with the same general character. Foss (1980) reported several topological maps for single jet injection normal to the crossflow. Especially interesting is the map for the U_{jet}/U_0 =0.9 case reported by Foss. That velocity ratio is the same as in the present work. The two cases differ, however, in that the present work contains many interacting jets and the jet injection angle is 30°. While many similarities were found there were also some differences.

9.2.1 Topological description of the measured mean velocity field

Stream-tubes are drawn in figures 9.4 on page 64 and 9.5 on page 65 to give a picture of the topology of the measured mean velocity field. All 3D figures were made using the EnSight program. Interpretations of the flow field in terms of its topology are given in figures 9.2 on the facing page and 9.3 on page 63.

In the measurements illustrated in figures 9.4 and 9.5, it is clear that a focus is present in the wake of the jet on each side of the center plane. An unstable node/saddle point is found downstream of the focus. A vortex is present on each side of the pipe exit which develops far downstream to form the counter-rotating vortex pair (often referred to as the CVP in the literature).

The velocity field in the present study bears many resemblances to the measurements of Kelso *et al.* (1996). The two velocity fields seem to have the same topological features. A major difference is that the focus seen in

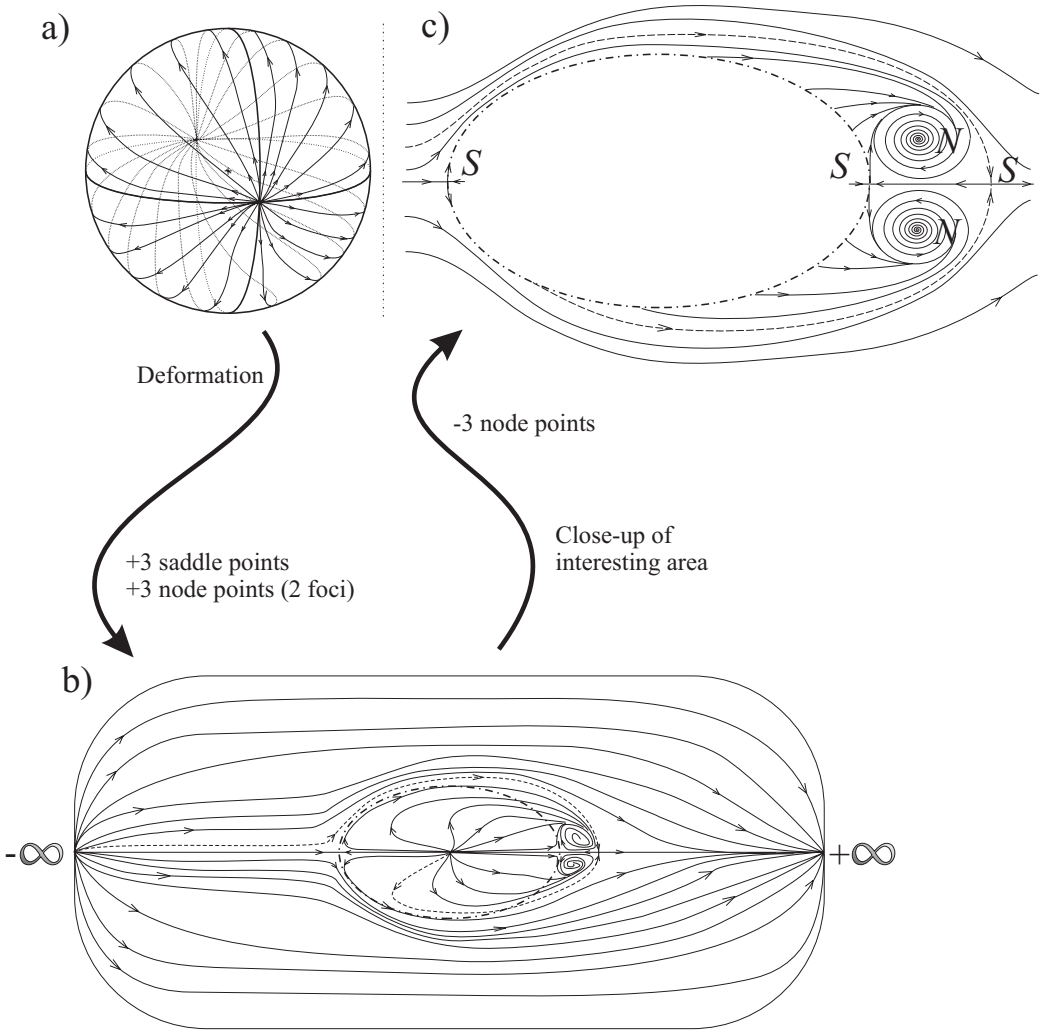

Figure 9.2: The upper figure shows that the flow on the sphere has two more nodes than saddles to be kinematically possible. The lower figure shows a deformed sphere with a deep cavity (the ellipse) with an unstable node at the bottom. It also gives an interpretation of the topology of the measured velocity field. Note that the figure below has the separatrix (dashed line to the saddle point) drawn differently on either side of the center line. The author is not sure where the separatrix connects. The measurements indicate that the top side version is more likely to be correct.

the measurements by Kelso *et al.* seem to rotate in the opposite direction as compared to the focus presented here. The measurement points of Kelso *et al.* are too few for precise stream-line tracing, which could explain the dissimilarity.

It is important for the understanding of the heat transfer to know the topology of the flow near the wall. By using knowledge of the flow field close to the wall from the measurements and the topological rules the asymptotic wall mean flow topology can be reconstructed. If we here consider a flat plate with a pipe junction, the difference between the number of nodes and the number of saddles is -1, cf. Hunt *et al.* (1978) and figure 9.2c. This can also easily be seen if we consider a sphere, see figure 9.2a. In such a case there are two more nodes than saddles. It is now possible to deform the sphere into the case of a flat plate with a pipe junction by the addition of three nodes (one node and two foci) and three saddles. Figure 9.2b shows an interpretation (in fact two) of the measured flow field. One unstable node is placed at the bottom of a deep cavity (the injection hole), two foci are placed behind the orifice and the three saddles are placed on the center line in front of the pipe exit and on either side of the foci. The line that connects with the saddle in the most downstream position separates fluid from different regions. A line like this is called a *separatrix*. It is difficult to tell from the measurements from which of the critical points the separatrix originates. There are four choices: the node at $-\infty$, the most upstream saddle, the node in the pipe or the saddle next to the foci. The last one is unlikely. Perry & Chong (1987) reported that saddle-to-saddle connections are extremely rare. Judging from the measurements, the first choice is the most probable, but it is still difficult to tell. In figure 9.2b, two different cases are drawn on either side of the center line. In the upper case (which is supported by the measurements), fluid from the crossflow can enter the focus, while in the case in the lower part of the figure, the most near-wall fluid must come from the jet. *It is thus important to the heat transfer where the separatrix connects*. If we count the nodes and the saddles in figures 9.2c and 9.3, according to equation 9.3, the sum is -1. As n=2, the sum should be -1 and the flow in that plane is thus kinematically correct described. A similar topological map is given in Coelho & Hunt (1989). As mentioned before Foss (1980) gives a topology map for U_{jet}/U_0 =0.9 and perpendicular jet injection. That map and the one described here bear many similarities but also have some features that are not similar. Foss reports several foci near the hole exit in the wake. The present study showed only one focus on each side of the center plane. Further, Foss observed one more saddle point in front of the jet and a stable node point in the wake, which somewhat complicated the picture near the hole exit at x/d =1.

The presence of saddle points in the wake implies an increased mixing of the two gas streams. Two particles that are close may take very different paths depending on the side of the separatrix on which they are located. This is one explanation for the good mixing characteristics of a jet issued into a crossflow.

Another explanation is offered by the concept of *chaotic advection*. Two skewed vortices (e.g. two orthogonal vortices separated by a distance) might show chaotic advection behavior. In the wake of the jet, there is one vortex from the focus and one vortex from each side of the jet. These two vortices are skewed and may show chaotic mixing properties. It is unlikely that the effect is large because the two vortices align rather quickly downstream.

It seems as though the two co-rotating vortices, from the focus and from the side of the pipe, spiral around each other for a short distance, see figures 9.3 on page 63, 9.5 on page 65 and 9.10 on page 70. They align further downstream and only one vortex is distinguishable. Chen *et al.* (1999) describe how two co-rotating vortices spiral together and merge at a point downstream, a merger. The vortex from the focus is exposed to a large straining motion from the side vortex and the jet.

The velocity field in Kelso *et al.* (1996) showed a number of 'horse-shoe' vortices in front of the jet. These were not observed in this investigation. It is possible that there exists such a vortex, but it is not obvious from the measurements. Vortices at the sides of the jet were found after x/d =0. A guess is that the side vortices either connect in front of the jet very close to the wall to form a horse-shoe vortex , below the measurement box (y/d <0.06), or connect inside the injection hole[1]. It should be noted that the experiment in Kelso *et al.* (1996) was at a much higher jet to crossflow velocity ratio and normal injection to the wall. The jet in their experiment was more like a surface mounted cylinder (the jet in crossflow case *is* different from the surface mounted cylinder case).

Yavuzkurt *et al.* (1980a) suggested that 'the jets reattach to the surface somewhere between 2.5 and 7 hole diameters downstream of their injection location'. The measurements presented in this study hint that there is a saddle point 1.8d downstream of the hole center that can be interpreted as a 'reattachment point'. The term 'reattach' is somewhat misleading in the sense that there is a separation line all the way downstream of x/d =1.8

[1]The topological map given in figure 9.2 may then have to include more nodes and saddles very close to the upstream saddle to account for the vortex system, cf. Kelso *et al.* (1996). As it is not clear (to the author) how to do this, these critical points were not introduced. There should probably be an attachment line with the a horse-shoe shape in front of the jet.

and a 3D separation (focus) upstream of x/d =1.8. The separation of the jet from the surface explains the high heat transfer, also seen by Crawford *et al.* (1976). In addition to this there are instationary events such as vortex shedding, see e.g. section 9.4.3, that also increase the heat transfer. For example, Yavuzkurt *et al.* (1980a) report that the best cooling performance is obtained for $\rho_{jet}U_{jet}/\rho_0 U_0$=0.4.

Stream-wise mean velocity $\overline{U}$

Figure 9.7 on page 67 plots the dimensionless stream-wise velocity component, $\overline{U}/U_0$, in the center plane.. A local maximum velocity is found at x/d =1 and y/d =0.5. This was also found by Yavuzkurt *et al.* (1980a) for $U_{jet}/U_0 = 0.9$, Andreopoulos & Rodi (1984) (referred to as a 'cover effect') and LeBrocq, Launder & Priddin (1971) for U_{jet}/U_0 =0.5 and 45° injection. There is a retardation of the fluid, a blockage effect, immediately in front of the jet, see also figure 9.6 on page 66. There are streaks of high speed stream-wise velocity at the sides of the pipe near the wall (below the side vortex). In the wake of the jet there is a back-flow region with negative $\overline{U}/U_0$, associated with the foci.

Figure 9.7 infers that the jet from the first row penetrates a distance of about 1.5 diameters into the crossflow. Yavuzkurt *et al.* (1980a) also reported that the jets penetrate to y/d =1.5.

Bergles *et al.* (1976) reported that the velocity distribution at the hole exit can be very non-uniform if the velocity ratio, U_{jet}/U_0, is low. The experiments reported in this thesis showed a very uniform velocity distribution in the exit plane which can be expected at higher velocity ratios, U_{jet}/U_0. Thole *et al.* (1997) reported that depending on the entrance crossflow Mach number the exit velocity profile can be very skewed. The skewness was reported to affect jet penetration and turbulence levels. A difference compared with the measurements here is that Thole *et al.* used a shorter injection hole with L/d=6 whereas the current test plate has L/d=8 injection holes, where L is the length of an injection hole. Longer injection holes has longer time to readjust from a separation at the entrance which can explain why no skewed velocity profile was found.

There is a locally large mean velocity gradient, 25000 s^{-1} (10 m/s change in 0.4 mm), in the shear layer of the jet in the wake. A comparison can be made with a turbulent boundary layer. Estimate the friction velocity in the pipe, u_*, by $\overline{U}_{jet}^{max}/25$=0.6 m/s. The mean velocity gradient $(\partial\overline{U}/\partial y)|_{wall} = u_*^2/\nu$, near the wall is then 25000 s^{-1}. We can see from this that the strongest mean velocity gradient in the leeward shear layer is of the same order of magnitude as the largest mean velocity gradient in

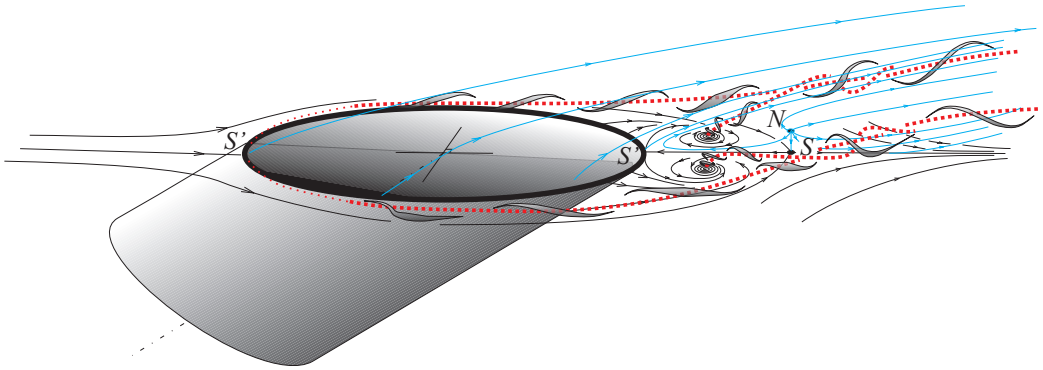

Figure 9.3: Interpretation of the measured velocity field and its topology.

a turbulent boundary layer with the same free stream velocity. If we use U_0 in the calculation, we instead get 32000 s^{-1}. Contrary to these findings, Yavuzkurt *et al.* (1980a) found small velocity gradients, except close to the wall, and low shear stress and turbulent kinetic energy.

Wall normal mean velocity $\overline{V}$

The wall normal velocity component is plotted in figure 9.8 on page 68. In the injection hole, the $\overline{V}$ component is $U_{jet} \sin 30^\circ / U_0$=0.45. A large gradient of this velocity component is found in the shear layer between the focus region and the jet. An island of elevated $\overline{V}$ is found at x/d =2.5 and y/d =0.25. Negative $\overline{V}$ is found at the sides of the jet near the wall, associated with the side vortex.

Lateral mean velocity $\overline{W}$

For positive z the $\overline{W}$ component is positive in front of the jet and negative behind and at the sides of the jet. The maximum lateral velocity component level, $\overline{W}/U_0$, found in the measurements was 38% at x/d =1.6, y/d =0.06 and z/d =0.4. The maximum level found by Yavuzkurt *et al.* (1980a) was 20% on the center line, z/d =0. This gives rise to some doubt as to whether those hot wire measurements are reliable.

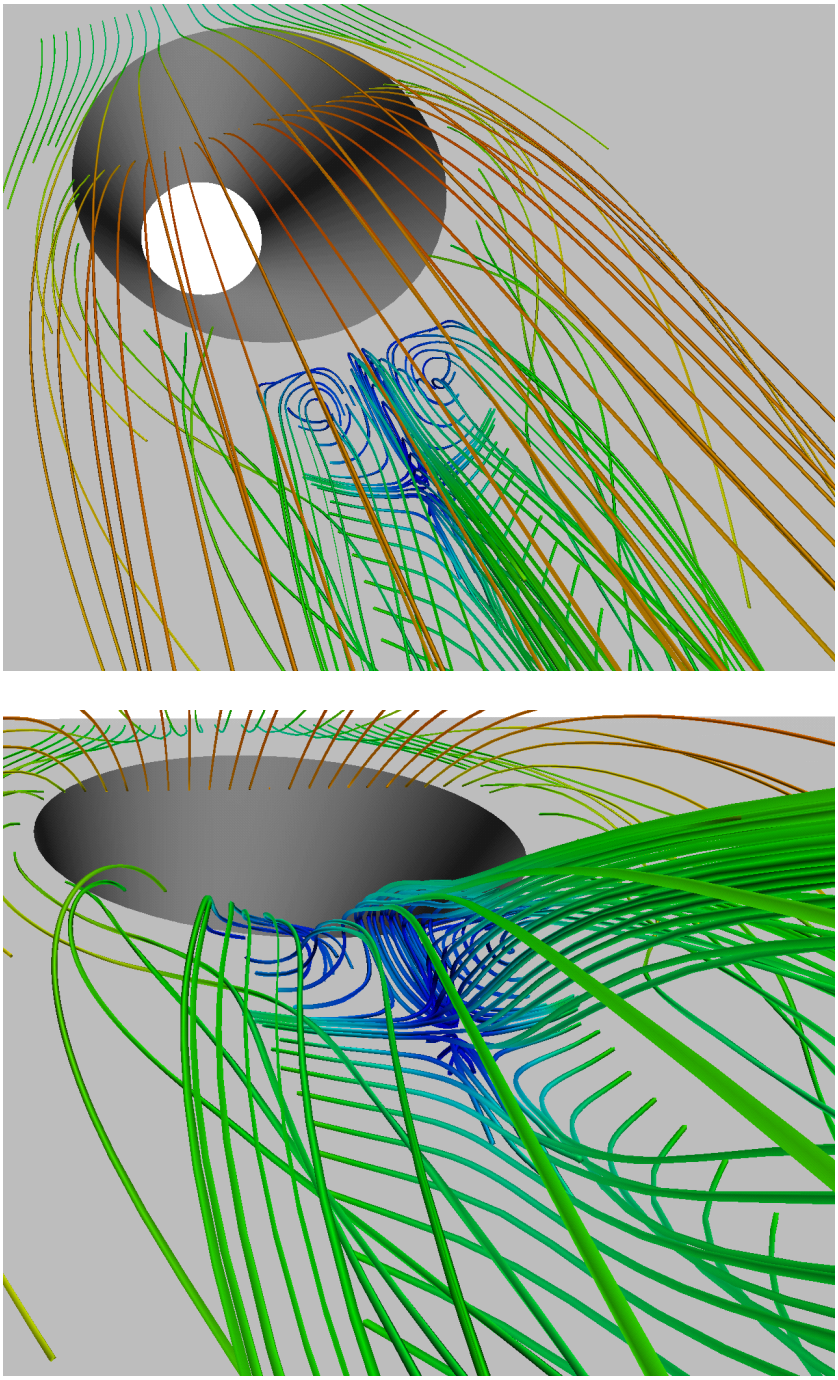

Figure 9.4: The flow is from the top left corner. Stream tubes are colored by the velocity magnitude. The counter rotating foci are shown aft of the pipe orifice. The unstable node/saddle point (stagnation point) is also visible. There is a separation line downstream of that point.

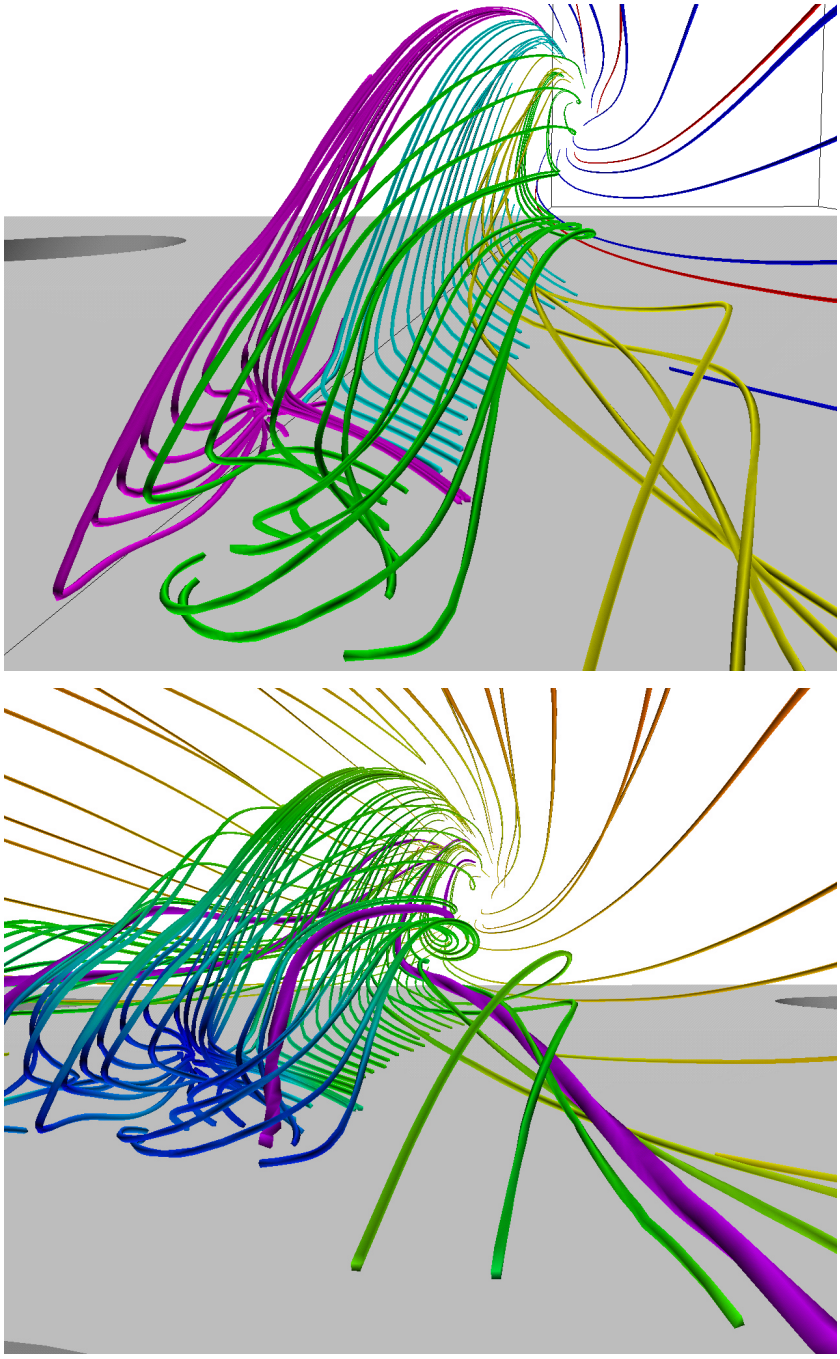

Figure 9.5: The lower left corners in the figures are located downstream of the jet, and the flow farther downstream is shown. *Top:* The stream tubes from different regions are colored separately by; red – crossflow, blue – jet, green – focus, yellow – side vortex, magenta – node/saddle point and cyan – separation line. *Bottom:* Large stream tubes shown in magenta are located in vortex cores. Small stream tubes are colored to show the velocity magnitude.

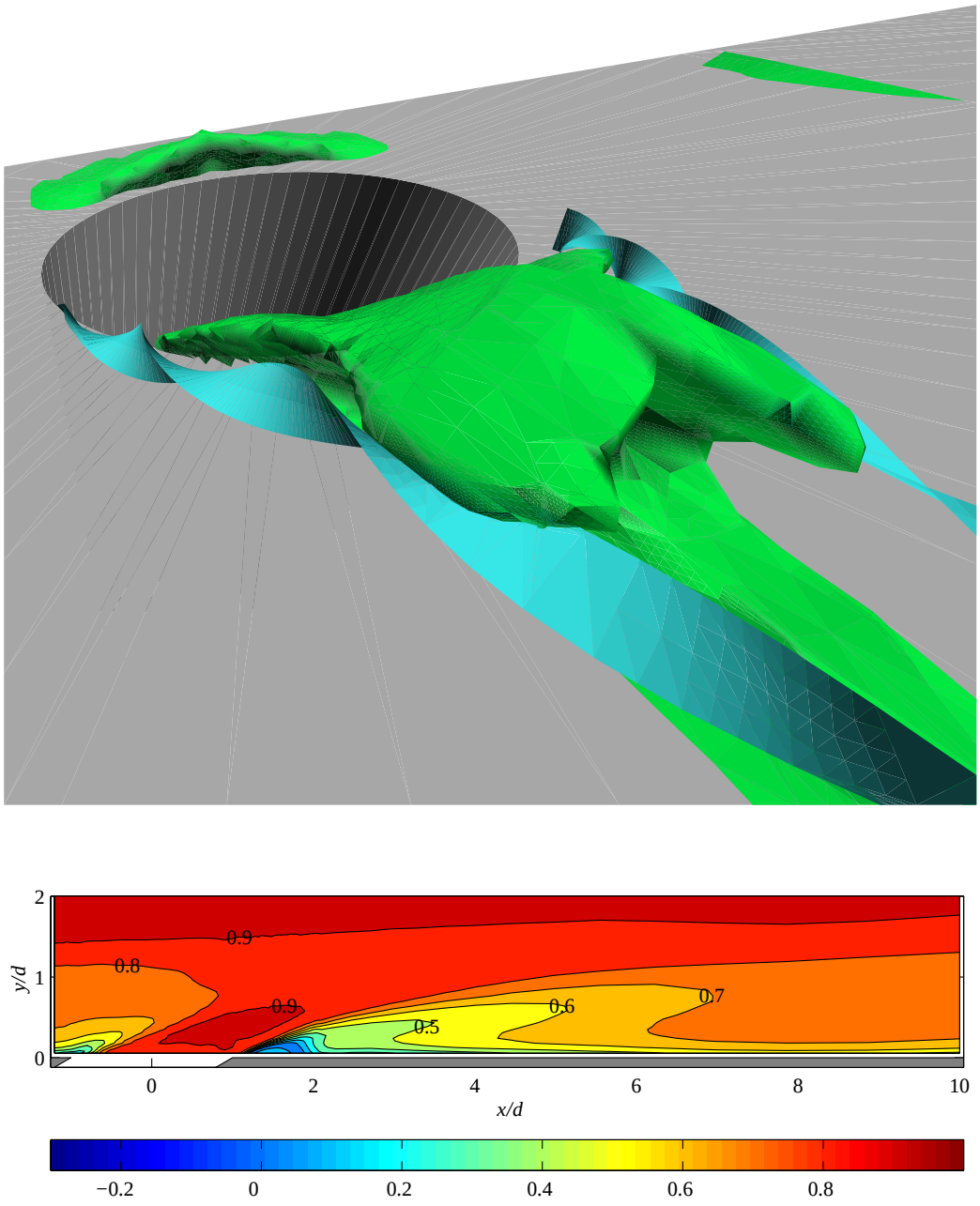

Figure 9.6: *Top:* An isosurface of the velocity magnitude $|\mathbf{V}|/U_0$=0.45 is shown and a stream ribbon in the side vortex is shown at the side of the jet. *Bottom:* Dimensionless velocity magnitude, $|\mathbf{V}|/U_0$, in the center plane, z/d =0.

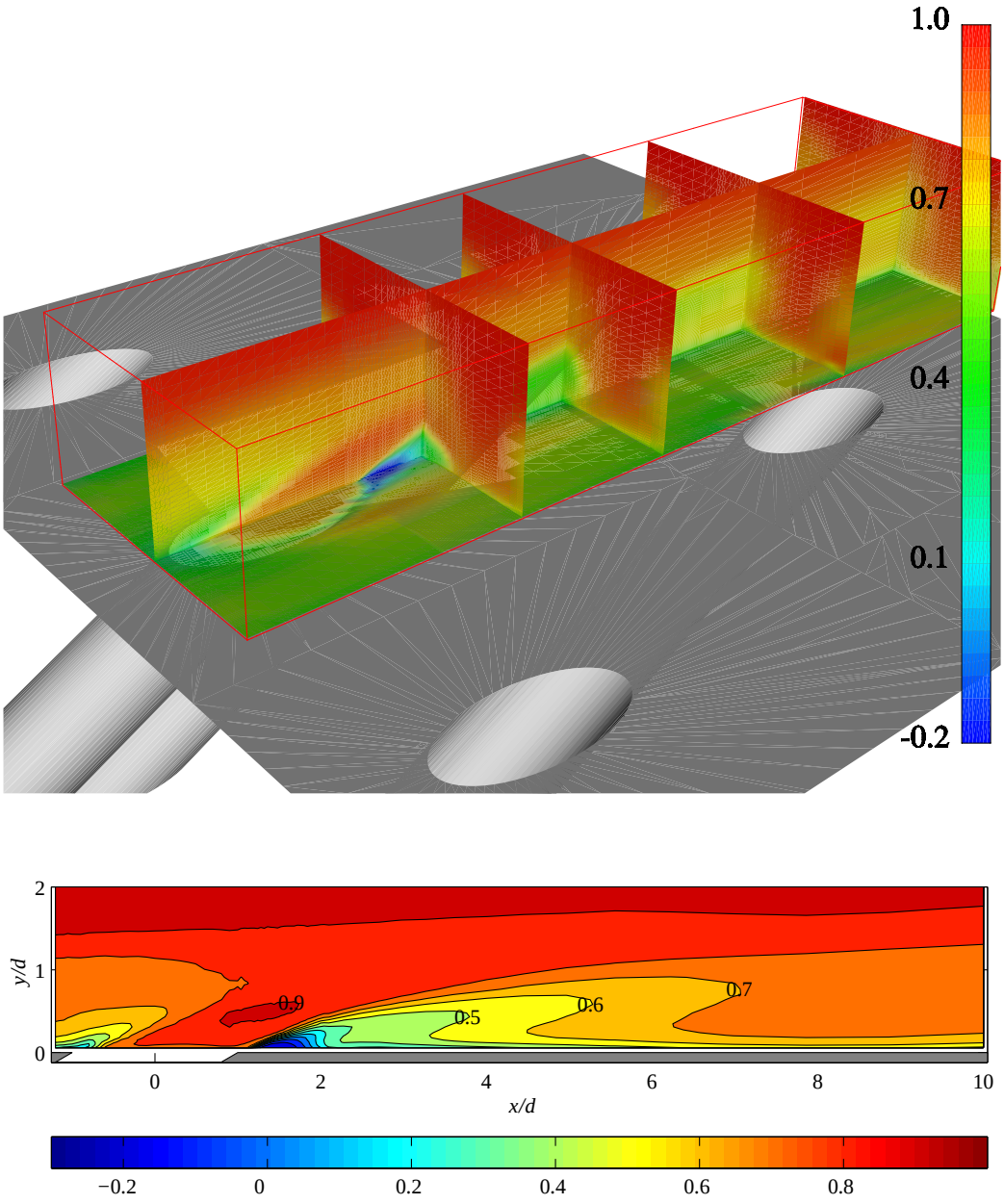

Figure 9.7: *Top:* The stream-wise velocity component, $\overline{U}/U_0$, in the planes x/d ={2,4,7,10}, y/d =0.06 and z/d =0. *Bottom:* $\overline{U}/U_0$, in the center plane, z/d =0.

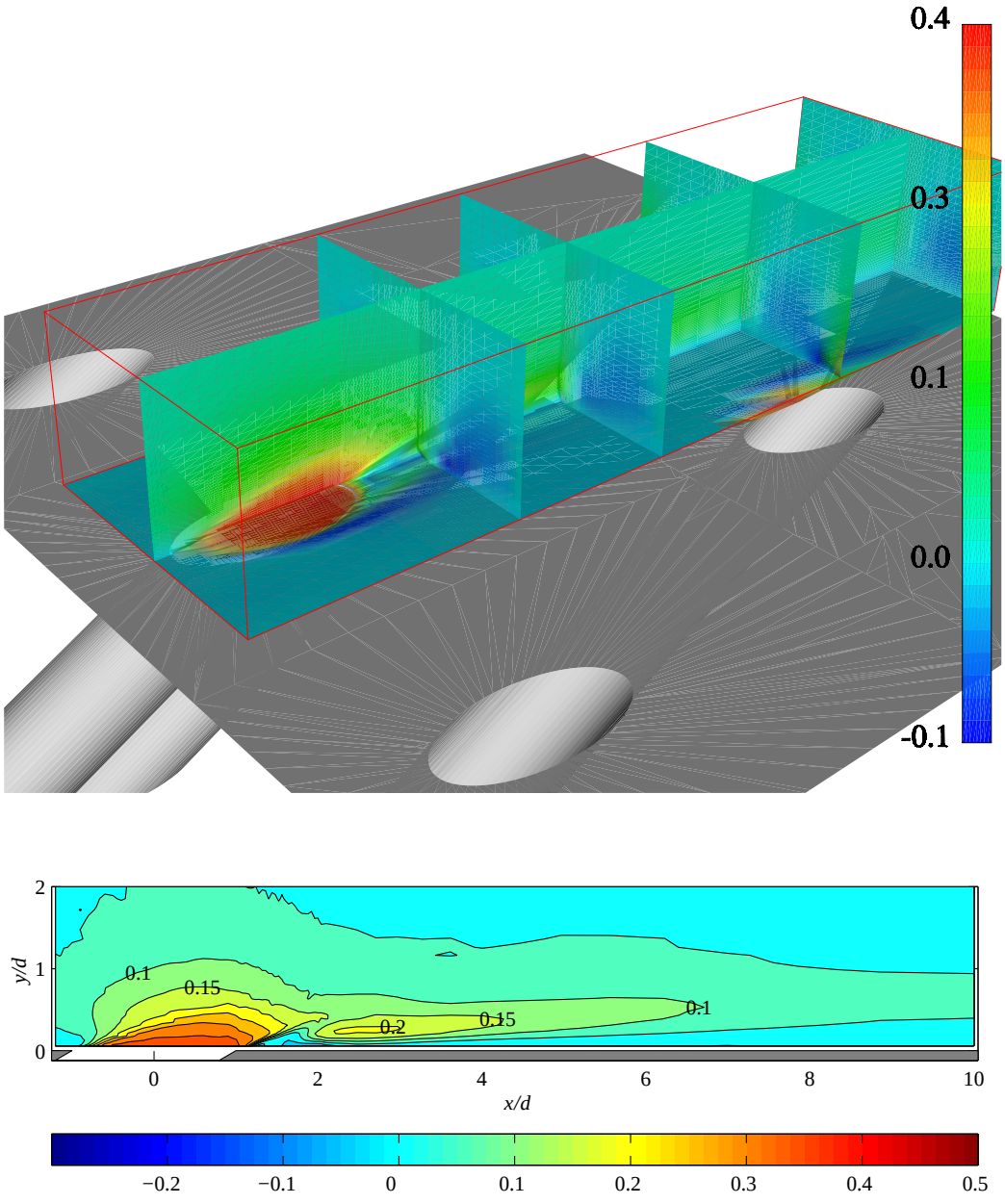

Figure 9.8: *Top:* The wall normal velocity component, $\overline{V}/U_0$, in the planes x/d ={2,4,7,10}, y/d =0.06 and z/d =0. *Bottom:* $\overline{V}/U_0$ in the center plane, z/d =0.

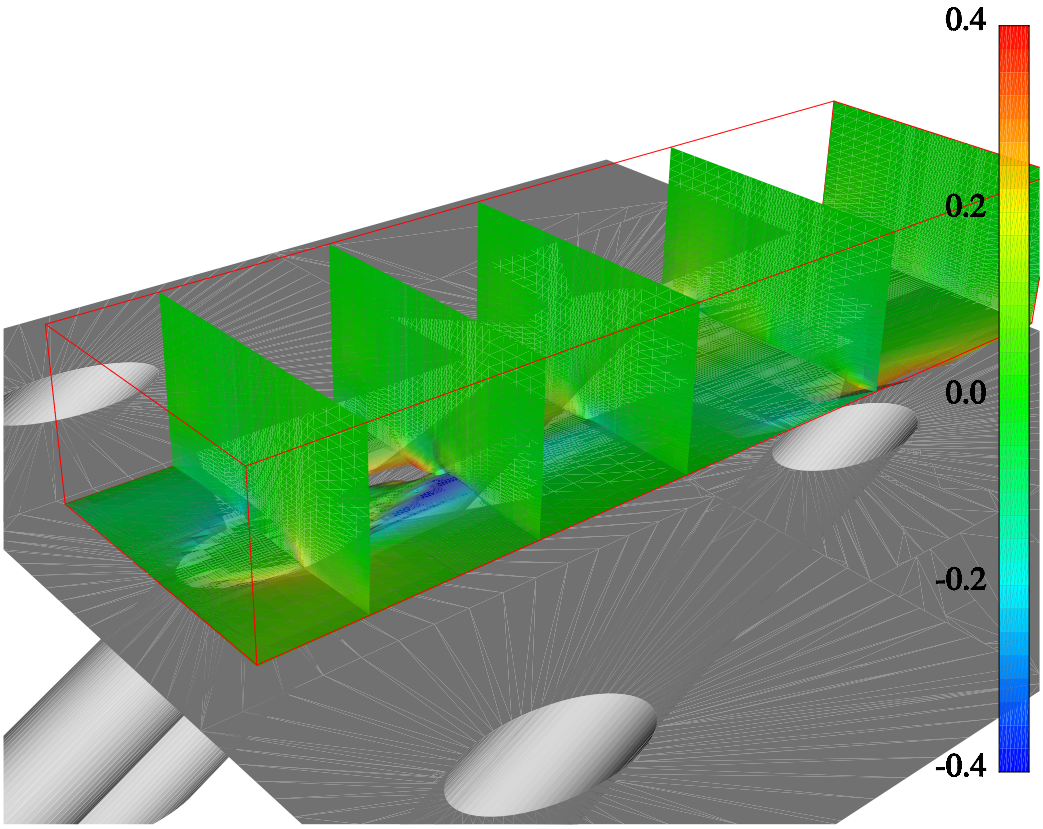

Figure 9.9: The lateral velocity component, $\overline{W}/U_0$, in the planes x/d ={0,2,4,7,10}, y/d =0.06 and z/d =0.

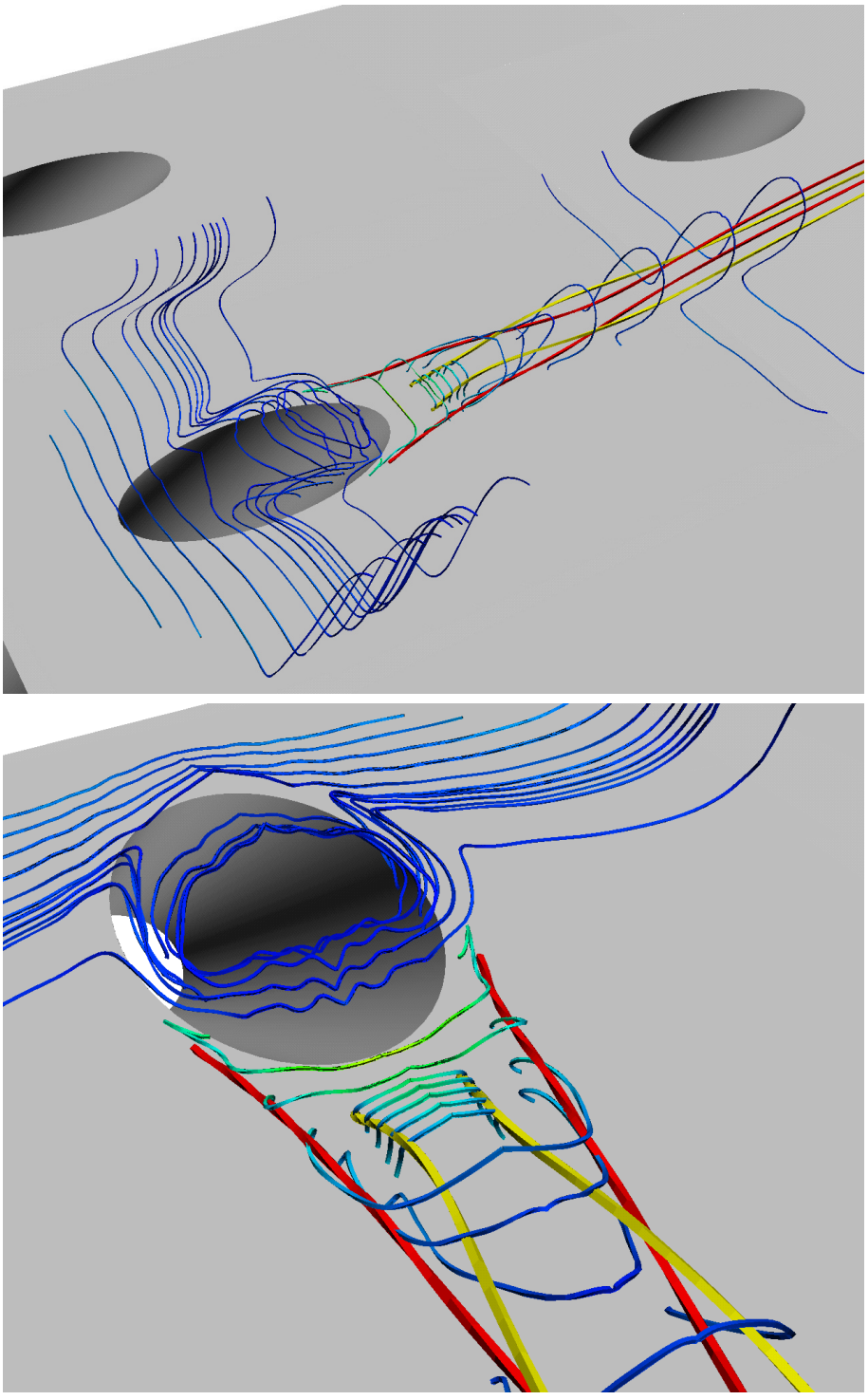

Figure 9.10: The vortex lines (in blue) are shaded by vorticity magnitude and the stream tubes in the vortex cores are red and yellow. *Top:* The flow is from left to right. *Bottom:* The flow is from the top left corner to the lower right corner.

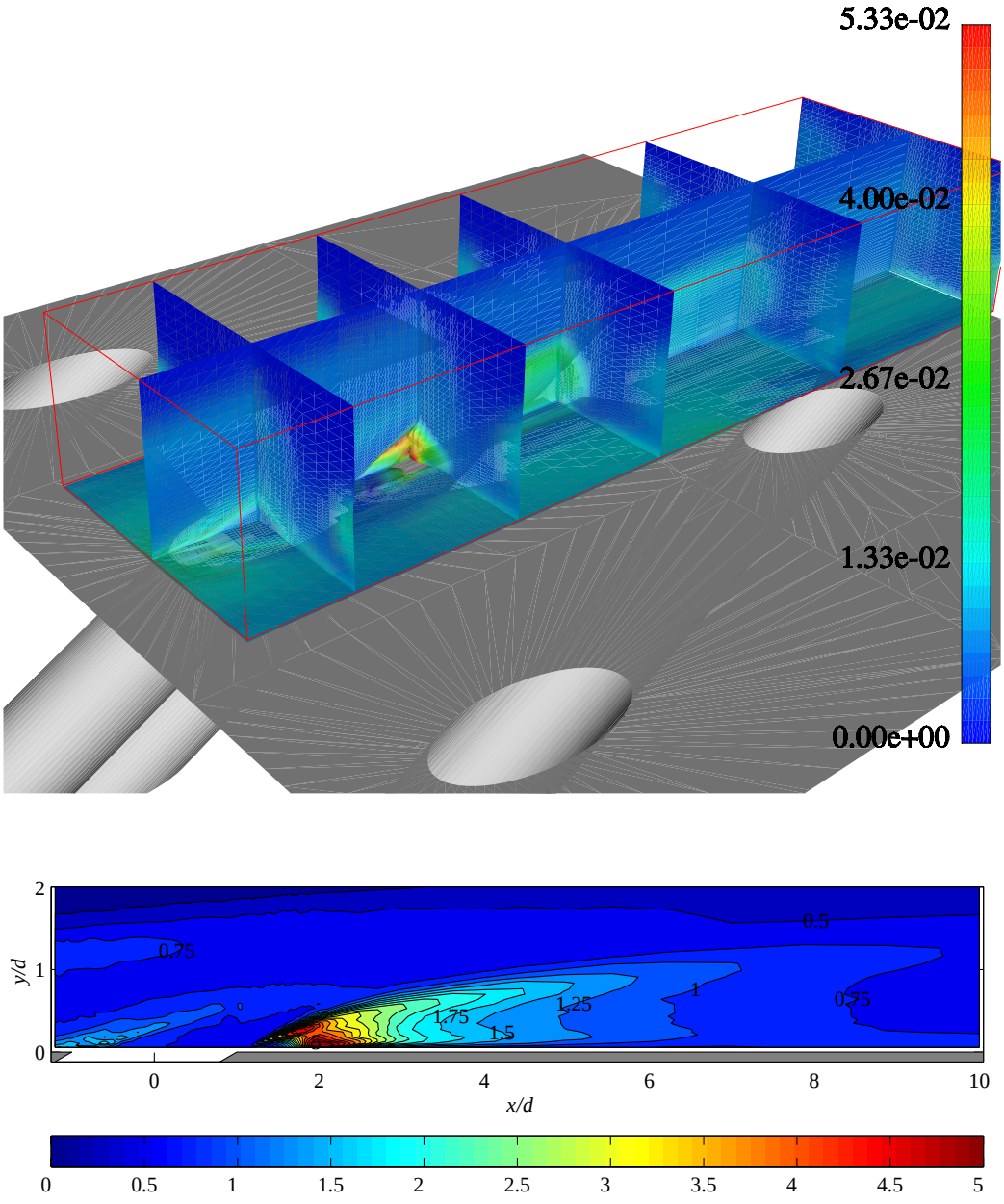

Figure 9.11: *Top:* The dimensionless turbulent kinetic energy, $\frac{1}{2}\overline{u_i u_i}/U_0^2$, in the planes x/d ={0,2,4,7,10}, y/d = 0.06 and z/d =0. *Bottom:* $\frac{1}{2}\overline{u_i u_i}/U_0^2$ [%], in the center plane, z/d =0.

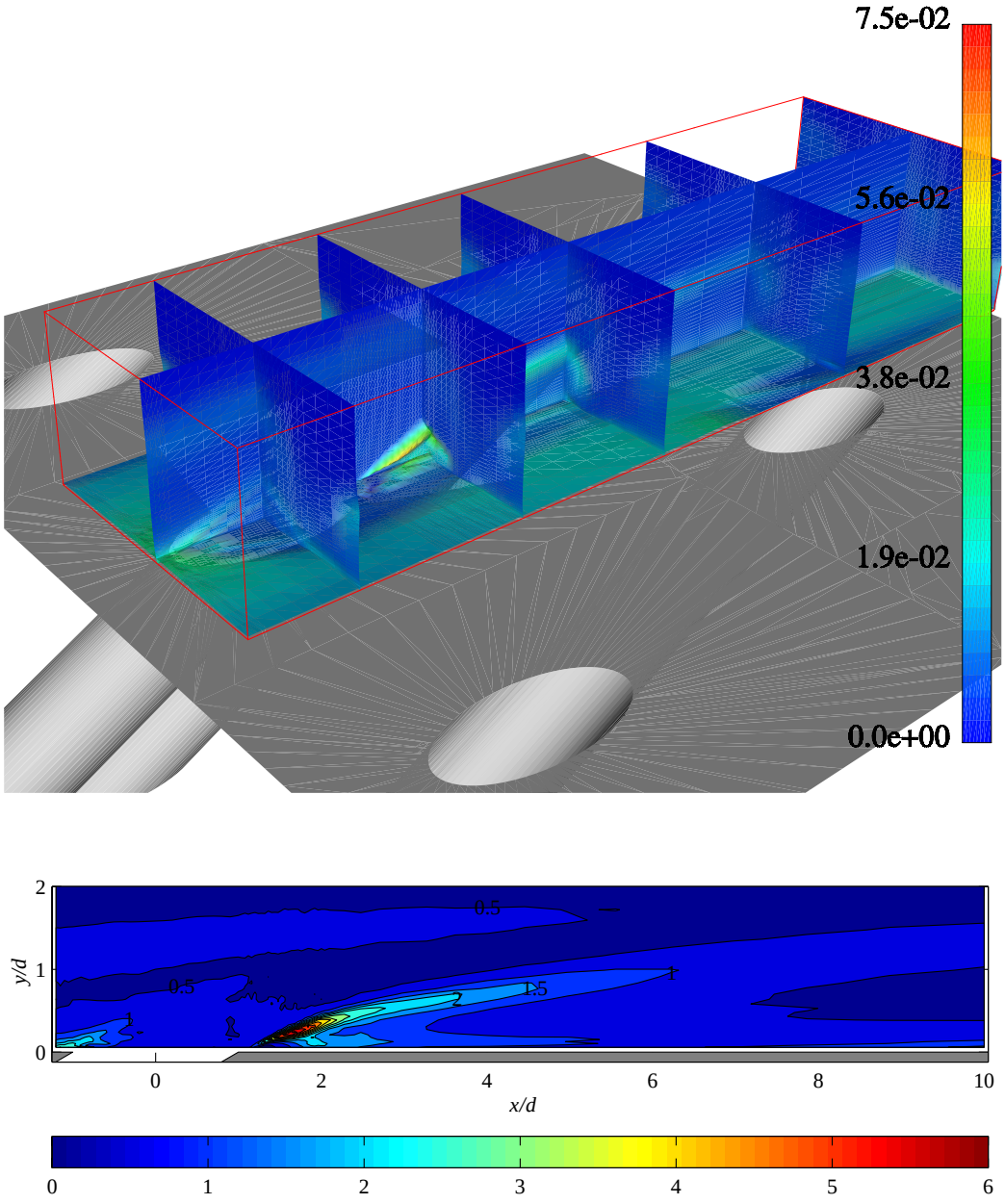

Figure 9.12: *Top:* The Reynolds normal stress, $\overline{u^2}/U_0^2$, in the planes x/d ={0,2,4,7,10}, y/d = 0.06 and z/d =0. *Bottom:* $\overline{u^2}/U_0^2$ [%] in the center plane, z/d =0.

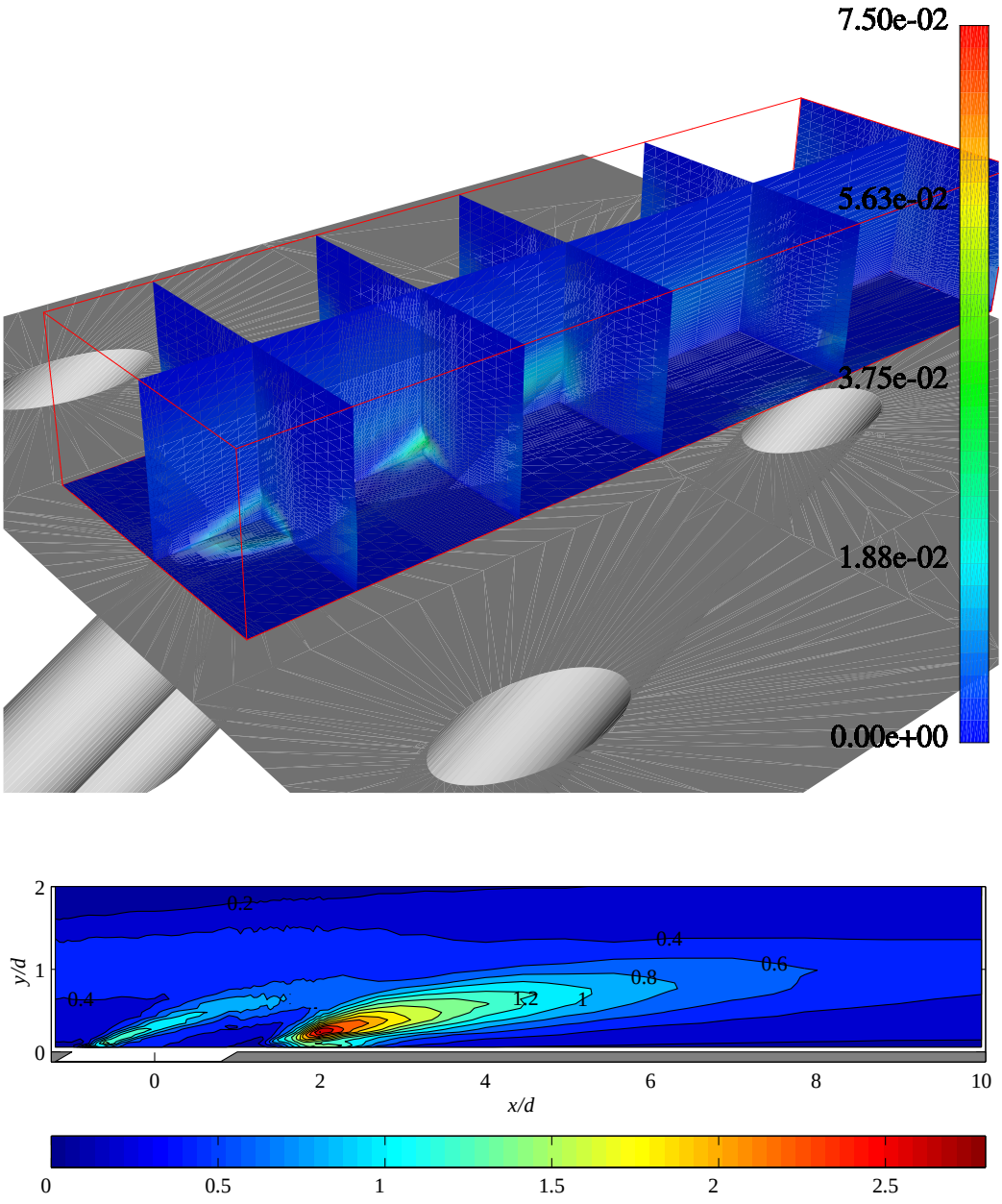

Figure 9.13: *Top:* The Reynolds normal stress, $\overline{v^2}/U_0^2$, in the planes x/d ={0,2,4,7,10}, y/d = 0.06 and z/d =0. *Bottom:* $\overline{v^2}/U_0^2$ [%] in the center plane, z/d =0.

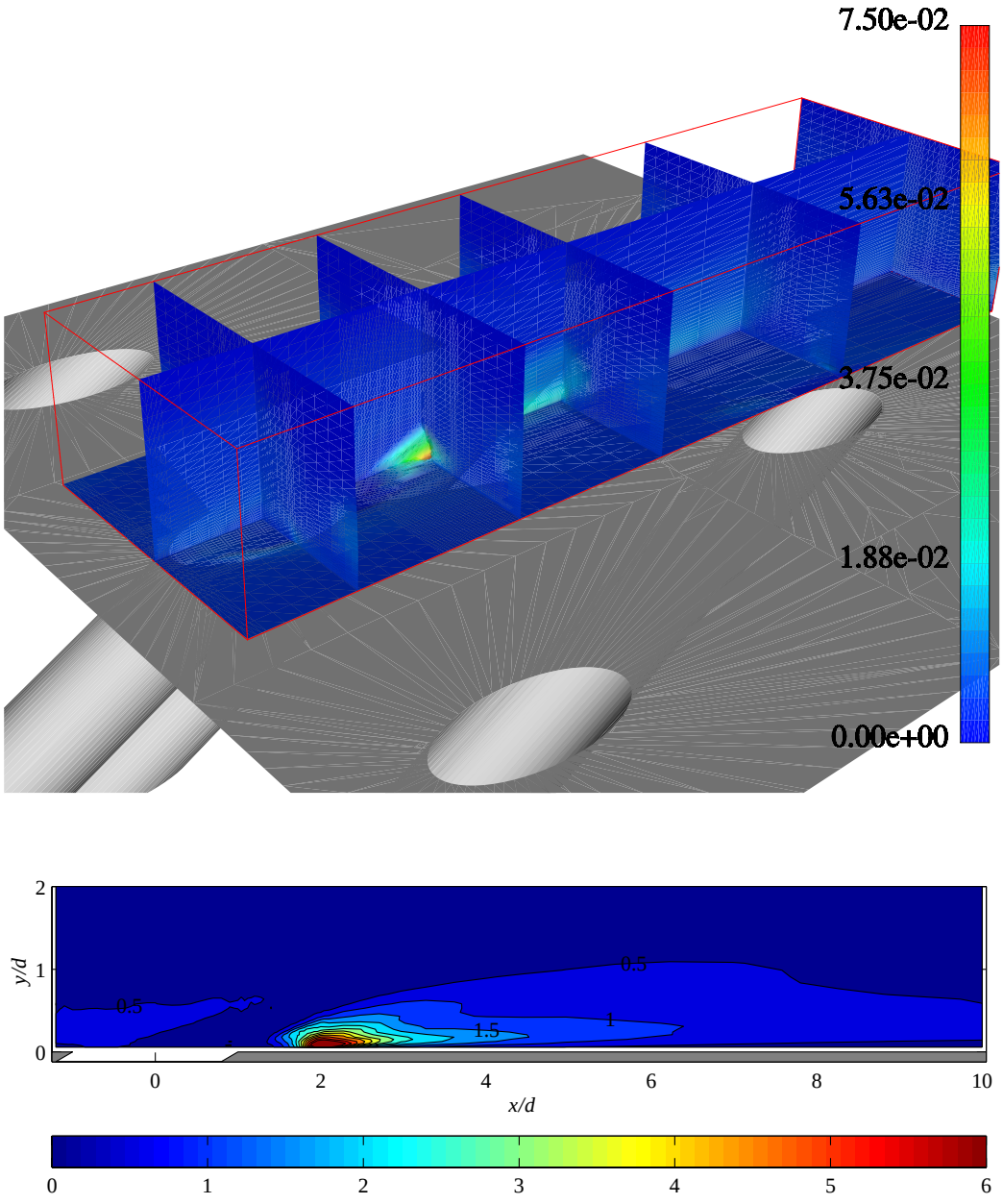

Figure 9.14: *Top:* The Reynolds normal stress, $\overline{w^2}/U_0^2$, in the planes x/d ={0,2,4,7,10}, y/d = 0.06 and z/d =0. *Bottom:* $\overline{w^2}/U_0^2$ [%] in the center plane, z/d =0.

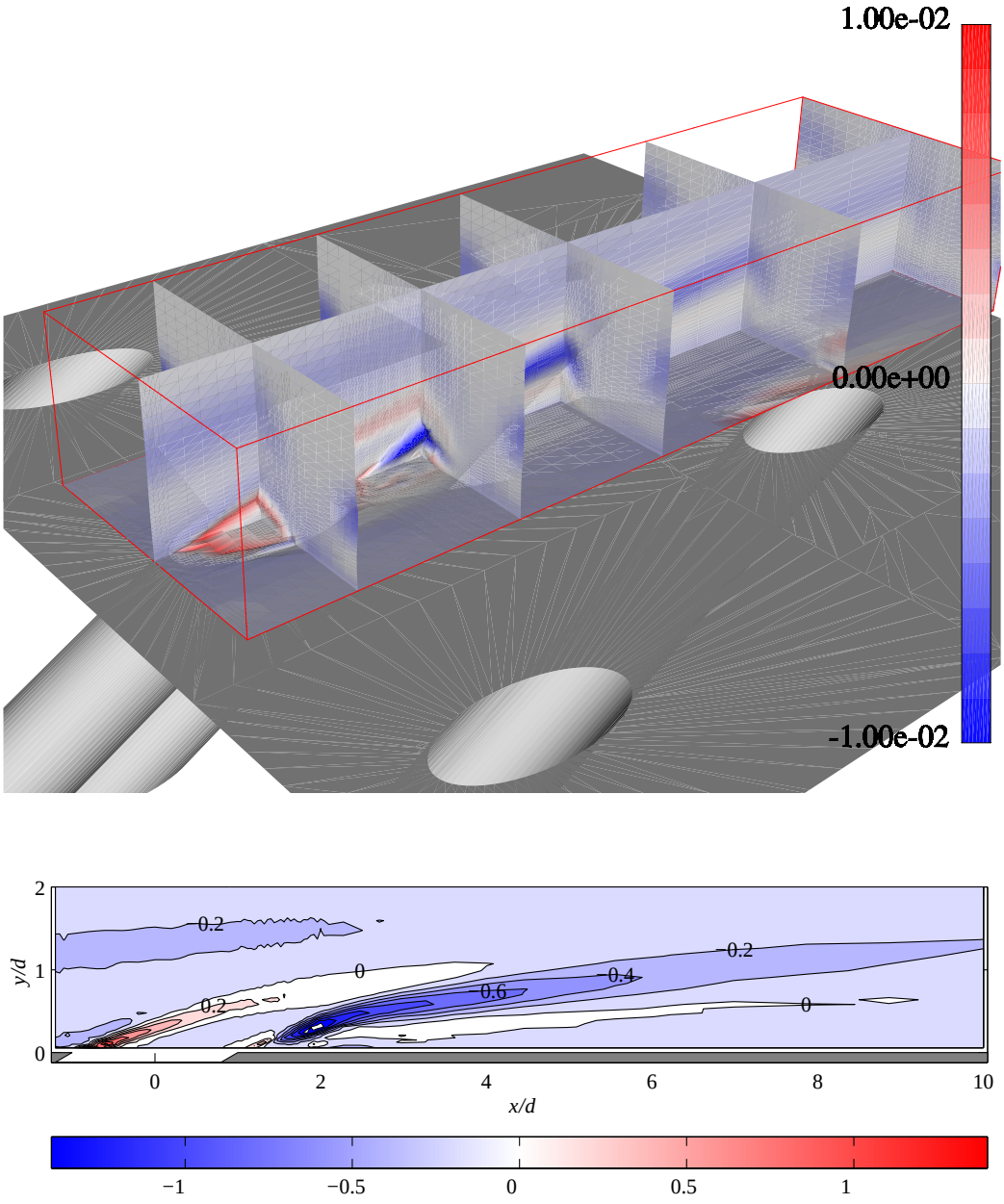

Figure 9.15: *Top:* The Reynolds shear stress, $\overline{uv}/U_0^2$, in the planes x/d ={0,2,4,7,10}, $y/d = 0.06$ and z/d =0. *Bottom:* $\overline{uv}/U_0^2$ [%] in the center plane, z/d =0.

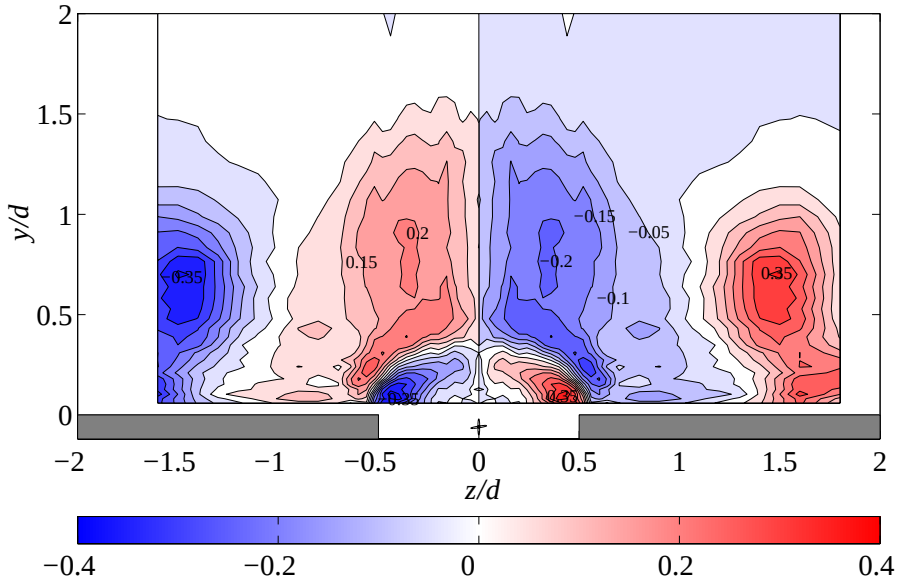

(a) x/d =0

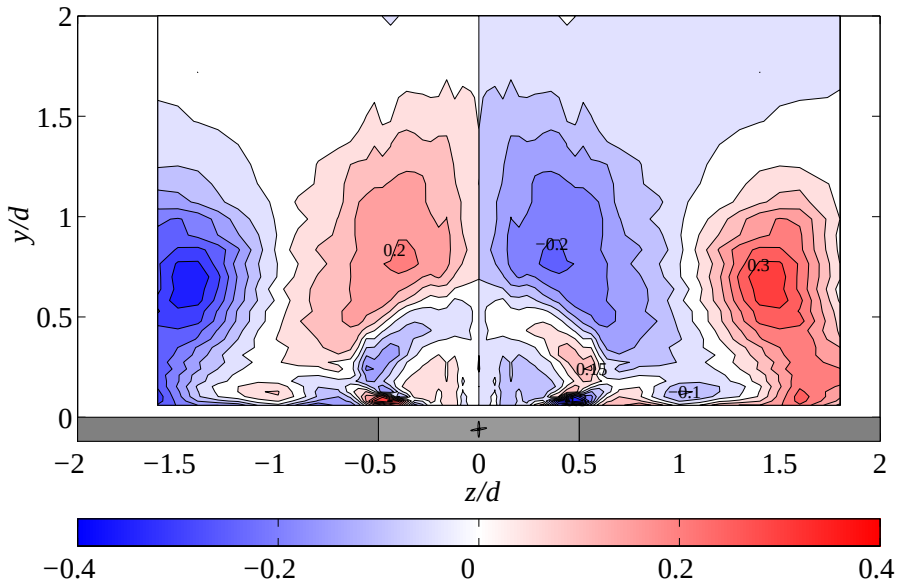

(b) x/d =1

Figure 9.16: The Reynolds shear stress, $\overline{uw}/U_0^2$ [%], in the x/d =0 and x/d =1 planes. The intersection of the two ellipses at y/d =-0.1 and z/d =0 shows the size of the measurement volume. *Note* that the left side gives a mirror image of the right side for clarity.

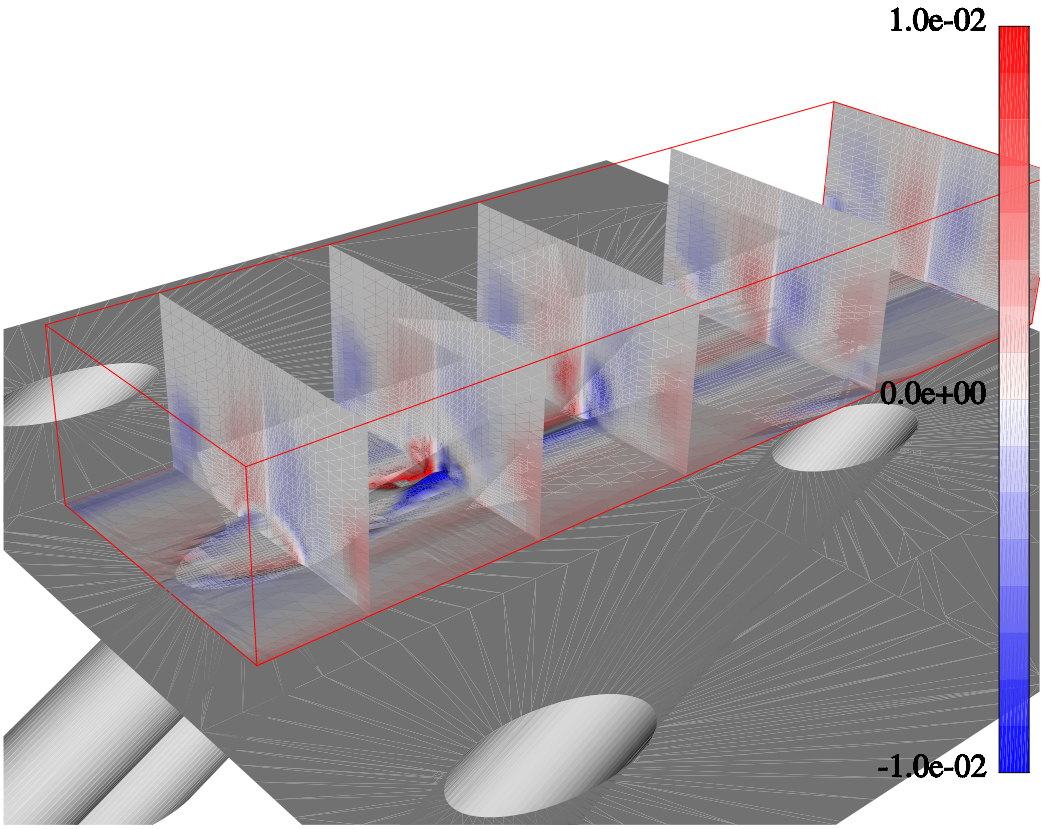

Figure 9.17: The Reynolds shear stress, $\overline{uw}/U_0^2$, in the planes x/d ={0,2,4,7,10} and y/d =0.06.

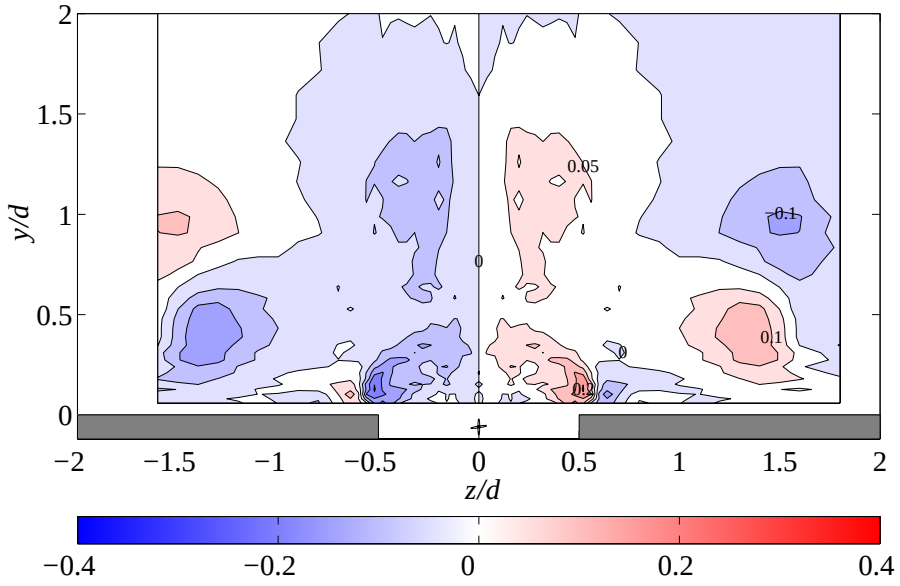

(a) x/d =0

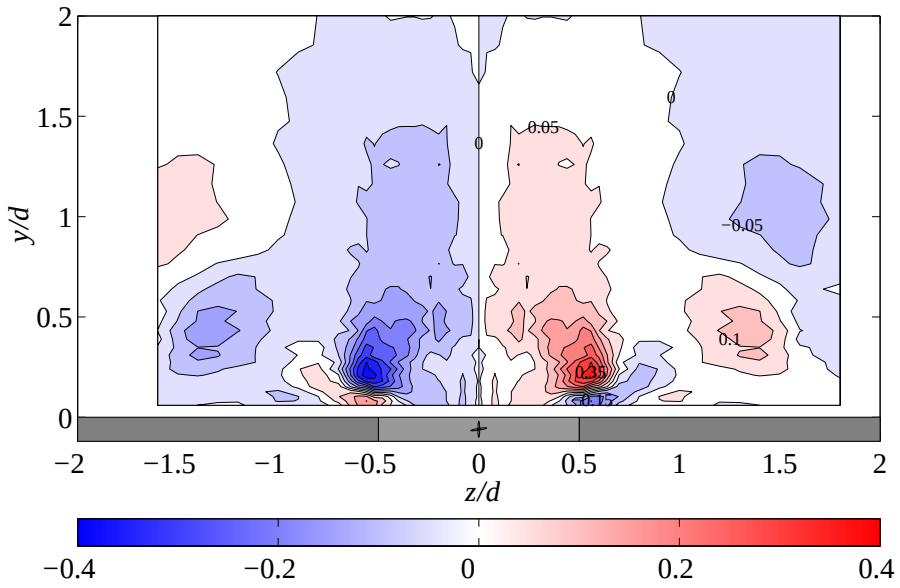

(b) x/d =1

Figure 9.18: The Reynolds shear stress, $\overline{vw}/U_0^2$ [%], in the x/d =0 and x/d =1 planes. The intersection of the two ellipses at y/d =-0.1 and z/d =0 shows the size of the measurement volume. *Note* that the left side gives a mirror image of the right side for clarity.

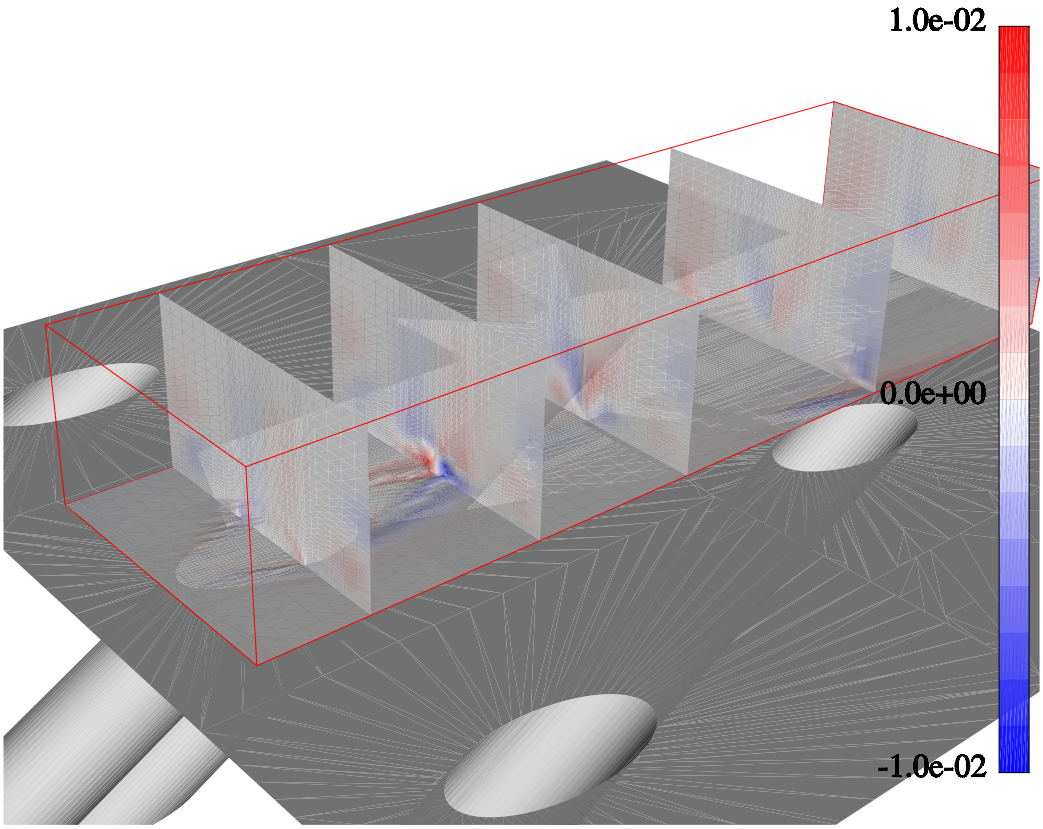

Figure 9.19: The Reynolds shear stress, $\overline{vw}/U_0^2$, in the planes x/d ={0,2,4,7,10} and y/d =0.06

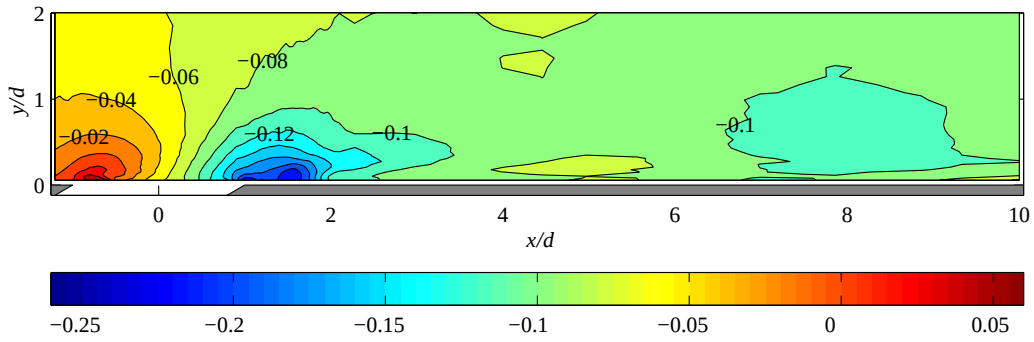

Figure 9.20: The pressure coefficient, C_P, in the center plane, z/d =0.

9.3 Mean vorticity field

The source of vorticity in the wake of the jet in crossflow is poorly understood. The only sources of vorticity are stretching, turning and, to a minor extent, diffusion of vorticity from the flat plate boundary layer and the vorticity in the injection hole boundary layer. There is thus a fundamental difference between a jet in crossflow and a surface mounted cylinder. Another difference is that the 'horse shoe' vortex of the surface mounted cylinder has the opposite rotation to that of the jet in crossflow. Fric & Roshko (1994) suggest that the vorticity in the wake of the jet comes from the flat plate boundary layer.

The mean vorticity field is illustrated in figure 9.10 on page 70 by vortex lines, which are lines parallel to the local mean vorticity vector. The vorticity field is computed by differentiation of the measured velocity field using second order central differences. The measurement points are to sparse in some locations (far downstream) for a good estimation of the vorticity. It is only intended to give a general picture of the vorticity field and to see whether it was possible to make such measurements. Vortex lines, in the same way as streamlines, have their own set of critical points and must fulfill continuity, i.e. they must be closed, just as stream lines. Figure 9.10 shows some instances of parallel stream lines and vortex lines. This type of flow is referred to as *Beltrami flow* and is quite rare. Moussa *et al.* (1977) report Beltrami flow in the near-jet region.

The mean vorticity field was actually found to be less complex than the velocity field. We can see from figure 9.10 that, upstream of the injection hole within the boundary layer, the direction of the vorticity vector is mainly in the negative z-direction, as expected. Inside the pipe there are rings of closed vortex lines, as expected in pipe flow. It is interesting to see that the vortex lines from the boundary layer are raised and circle around

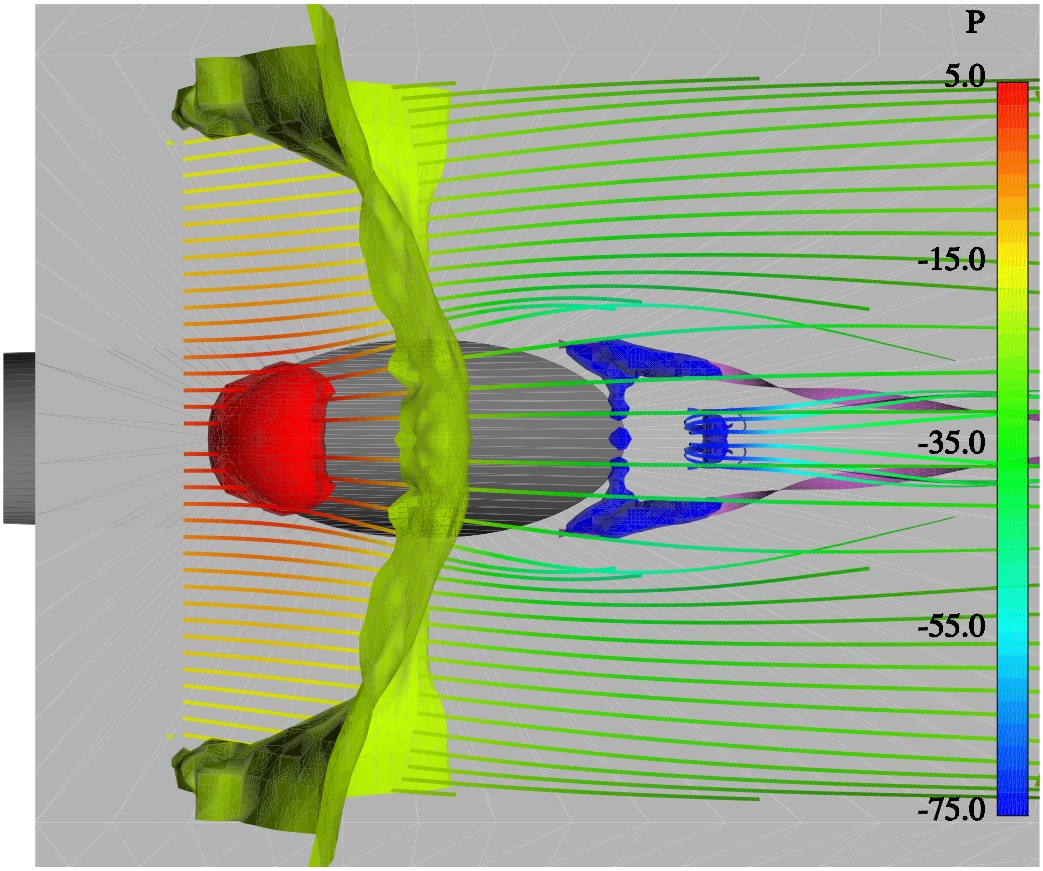

Figure 9.21: View from above. The pressure field illustrated by isobars for P={5,-20,-75}Pa.

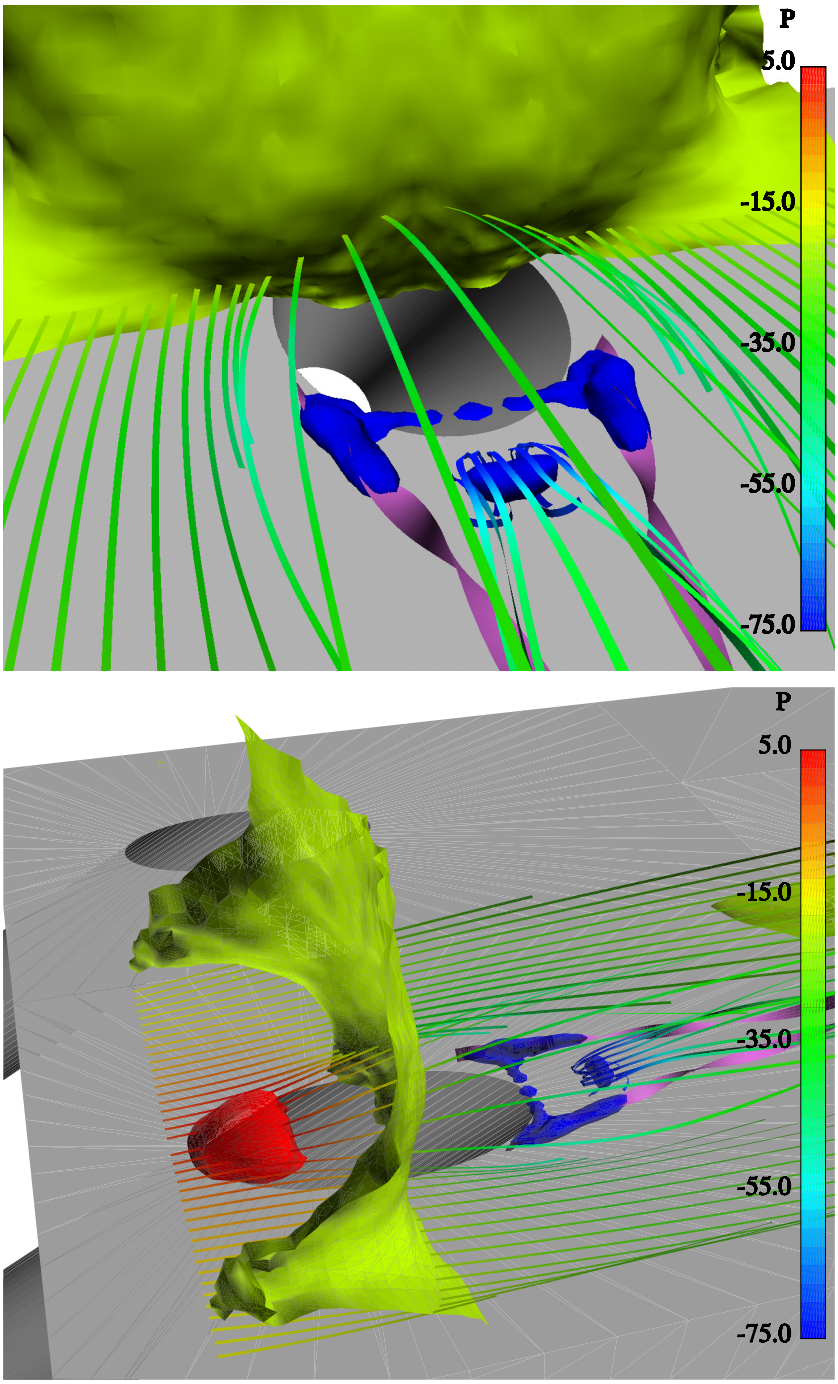

Figure 9.22: The pressure field illustrated by isobars for P={5,-20,-75}Pa. *Top:* View from a downstream position. *Bottom:* Side view, flow is from left to right.

the vortex line rings. The boundary layer vorticity is also turned downstream at the sides of the issuing jet, hereby creating positive Ω_x vorticity for positive z. It seems as though the boundary layer vortex lines circle around the circular vortex lines at the rear of the pipe orifice. The wake of the jet is dominated by low speed fluid surrounded by high speed fluid. This means that the vortex lines in this area look like arcs or 'hair pins'.

A source of vorticity in the counter-rotating vortex pair is stream-wise vorticity, Ω_x, in the pipe at the sides. Another source of Ω_x is a hypothetical vortex sheet between the crossflow and the pipe flow, as pointed out by Foss (1980). Imagine a uniform velocity in the y-direction in the jet and a uniform velocity in the x-direction in the crossflow outside of the jet flow. The imagined vortex sheet between the jet and the crossflow contains Ω_x and Ω_y vorticity.

The equation for the mean vorticity, Ω_i, in a turbulent field reads:

$$U_j \frac{\partial \Omega_i}{\partial x_j} = \frac{\partial}{\partial x_j} \left(\overline{\omega_j u_i} - \overline{u_j \omega_i} \right) + \Omega_j \frac{\partial U_i}{\partial x_j} + \nu \frac{\partial^2 \Omega_i}{\partial x_j \partial x_j}, \tag{9.4}$$

where ω_i is the fluctuating vorticity. The $(\overline{\omega_j u_i})_{,j} = \overline{\omega_j s_{ij}}$ term is the stretching and turning by fluctuations in the strain rate and $(\overline{u_j \omega_i})_{,j} = \overline{u_j \partial \omega_i / \partial x_j}$ is the mean transport of fluctuating vorticity by fluctuations in velocity, an analogue to the Reynolds stresses. Stretching and turning of mean vorticity by the mean field is done by the $\Omega_j \partial U_i / \partial x_j$ term. In equation 9.4, the term $\Omega_j \partial U_i / \partial x_j$ was computed and compared to find out which of the terms that are responsible for the turning and stretching of mean vorticity. This comparison may give insight into how boundary layer vorticity and pipe vorticity interact and how vorticity in the wake arises. The turbulent terms containing correlations of fluctuating velocity and fluctuating vorticity are impossible to measure with the LDA system used.

The boundary layer vorticity is turned in the downstream direction at the sides of the issuing jet after x/d =0 near the wall by $\Omega_z \partial U / \partial z$ and $\Omega_y \partial U / \partial y$, hereby creating positive Ω_x vorticity. Positive $\Omega_z \partial U / \partial z$ and positive $\Omega_y \partial U / \partial y$ are found at this position. Negative $\Omega_y \partial U / \partial y$ is, however, found in the same region but closer to the jet. It seems as $\Omega_z \partial U / \partial z$ is somewhat greater than $|\Omega_y \partial U / \partial y|$. Stretching of Ω_x by the $\Omega_x \partial U / \partial x$ term is observed in the same region but further downstream.

9.4 Reynolds stresses, $\overline{u_i u_j}$

Before the publication of Andreopoulos & Rodi (1984), no reliable measurements of turbulent shear stresses had been reported. Yavuzkurt *et al.* (1980a) reported finding an almost isotropic turbulent field. The measurements presented here clearly indicate that this is not the case everywhere in the turbulence field. Turbulence field measurements are important for the modeling of turbulent stresses and heat and mass fluxes.

Turbulent kinetic energy $\frac{1}{2}\overline{u_i u_i}$

The dimensionless turbulent kinetic energy, $\frac{1}{2}\overline{u_i u_i}\ /U_0^2$, is plotted in figure 9.11 on page 71. Large values are found in the leeward shear layer (the leeward shear layer starts at x/d =1 and the windward shear layer starts at x/d =-1) and gradually decrease further downstream in the wake. The turbulence level in the windward shear layer is considerably lower because the velocity ratio is close to unity. Samuel & Joubert (1965) observed that the closer the blowing ratio is to unity, the lower the turbulent mixing is for 2D injection. There are two maxima of $\frac{1}{2}\overline{u_i u_i}$ in the center plane, one maximum at x/d =2 and y/d =0.08 near the node point and one maximum at x/d =1.8 and y/d =0.2 in the leeward shear layer. The maximum turbulence level, 25%, is found at x/d =2 and y/d =0.08. It is interesting to see a very low level of turbulence between the pipe exit and a position upstream of x/d =1.5 close to the wall. An explanation might be that the fluid here is subjected to an irrotational strain rate which gives a negative contribution to the production. Profiles of $\frac{1}{2}\overline{u_i u_i}$ in the y-direction for x/d >2 in the center plane showed a double maximum, contrary to the observations of Yavuzkurt *et al.* (1980a).

9.4.1 Reynolds normal stress $\overline{u^2}$

Normal stress $\overline{u^2}$ is plotted in figure 9.12 on page 72. Large values are found in the shear layer on the lee side at x/d =1.5-2. Very low values of $\overline{u^2}$ are observed in the windward shear layer. The phenomenological map in Kelso *et al.* (1996) suggests no occurrence of roll-up of vortices in this shear layer for U_{jet}/U_0 <1. In downstream positions in yz-planes, the highest $\overline{u^2}$ values are found in kidney shaped regions. This can be explained by low velocity in the wake and higher velocity at the sides and above in the crossflow. In figure 9.12 there is a band of higher $\overline{u^2}$ above the studied jet. This is a remnant of the upstream jet. The $\overline{u^2}$ profiles have a double

maximum shape in the wake. One maximum is found near the wall and the other is in the trajectory of the earlier mentioned 'kidney shape'. In a near-wall plane, y/d =0.06, the $\overline{u^2}$ correlation is lower around the injection hole, under the side vortex, as compared to the $\overline{u^2}$ level elsewhere in that plane. These areas of low $\overline{u^2}$ persist downstream and are visible as bands for at least 5-6 hole diameters. Elevated $\overline{u^2}$ correlations in the y/d =0.06 plane were found downstream of the foci on either side of the center plane.

The maximum level of $u'/U_0 = (\overline{u^2}/U_0^2)^{1/2}$ was found to be 25% in the center plane, x/d =1.68 and y/d =0.24. This is interesting, because it is about the highest value that is usually found in *any* turbulent flow based on the same free stream velocity. Andreopoulos & Rodi (1984) report u'/U_{jet}=0.3 (cf. above u'/U_{jet}=28%). The lowest level, 4% of u'/U_0 in the wake of the jet, was found just below the emanating jet in the focus close to the injection hole.

9.4.2 Reynolds normal stress $\overline{v^2}$

The normal stress, $\overline{v^2}$, is plotted in figure 9.13 on page 73. A comparison between the $\overline{u^2}$ plot (9.12) and the $\overline{v^2}$ plot (9.13) shows that the $\overline{v^2}$ field is similar to the $\overline{u^2}$ field. The differences are that the areas with high $\overline{v^2}$ values are broader and the magnitude is lower. The windward shear layer also has higher $\overline{v^2}$ intensity compared to the $\overline{u^2}$ intensity. The maximum value, 16%, of v'/U_0, was found at x/d =2.0 and y/d =0.24 in the center plane. A very low level, 2%, of v'/U_0 was found at x/d =1.2, y/d =$\sim$0.06 and z/d =$\pm$0.21.

9.4.3 Reynolds normal stress $\overline{w^2}$

Normal stress $\overline{w^2}$ is plotted in figure 9.14 on page 74. Compared to $\overline{u^2}$, the $\overline{w^2}$ component is more dominant below the node point in the wake of the jet, at x/d =2.0, y/d =0.08 and z/d =0. No significant $\overline{w^2}$ component (compared to $\overline{u^2}$) is present in the windward and leeward shear layers. The $\overline{w^2}$ component seems to be prominent in the entire wake. The high values indicate much movement laterally close to the wall. This enhances the heat transfer and probably sweeps in hot air from the sides, thereby destroying the protective film. The highest value of w'/U_0 was 27% at x/d =2.0, y/d =$\sim$0.08 and z/d =0. A very low w'/U_0 level, 1%, was found at x/d =1.14, y/d =$\sim$0.06 and z/d =$\pm$0.22.

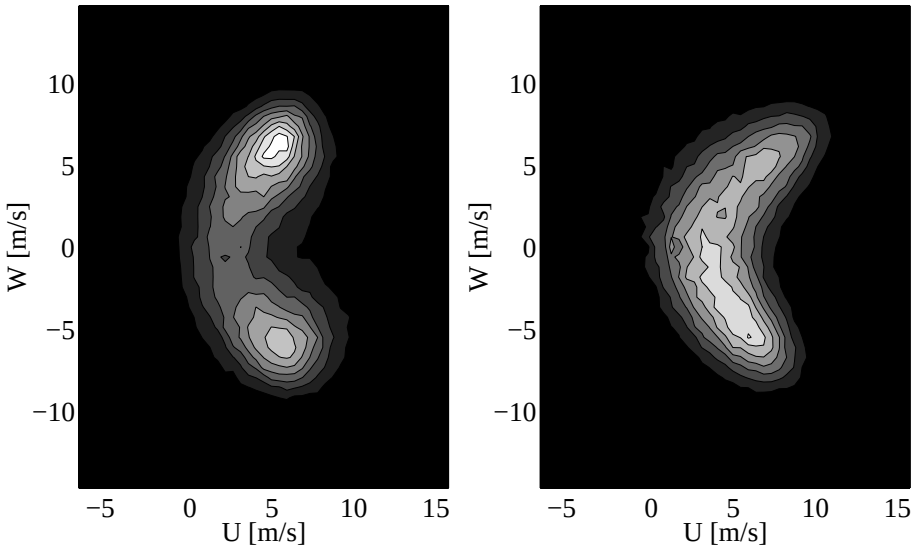

Figure 9.23: Joint PDF of (U,W) in the center plane, x/d =2 and y/d =0.06. The left figure has no weight and the right figure has velocity magnitude weight.

A particular measurement was made at x/d =2, y/d =0.06 in the center plane with 160000 samples. At this point the joint probability density function, PDF, of U and W was found to have as boomerang shape, see figure 9.23. This shape suggests a large $\overline{uw^2}$ component. Any lateral movement (z-direction) is also coupled with positive stream-wise movement (x-direction) and vice versa. There are large values of $\overline{uw^2}$ along the whole center plane in the wake, with areas of negative $\overline{uw^2}$ at the sides. This can be interpreted as a turbulent transport of $\overline{uw}$ by w fluctuations.

It can be seen in figure 9.23 how the velocity bias correction affects the PDF. In the left figure (with no weight) there is more of a flip-flop behavior whereas, in the right figure, obtained with velocity magnitude weighting, there is more of a uniform distribution. The figure indicates that high velocity ($\sim$10 m/s) fluid from the sides sweeps into the wake. The phenomenological map in Kelso *et al.* (1996) does not give an indication of any events of upright (y-direction) vortex shedding in the wake for U_{jet}/U_0 <1.

The autocorrelations were also computed at the point mentioned above, showing that the integral time scale, $\mathcal{T}_u$, was $\sim$ 0.33 ms, $\mathcal{T}_v$ was $\sim$0.21 ms and $\mathcal{T}_w$ was $\sim$ 0.43 ms. The autocorrelation for W, see figure 9.24 on the facing page, showed a weak second peak, almost like a plateau, between 1 ms and 1.8 ms, but little correlation was found after 2 ms. Remember that 5000 samples were taken at 100-1000 Hz at every measurement point.

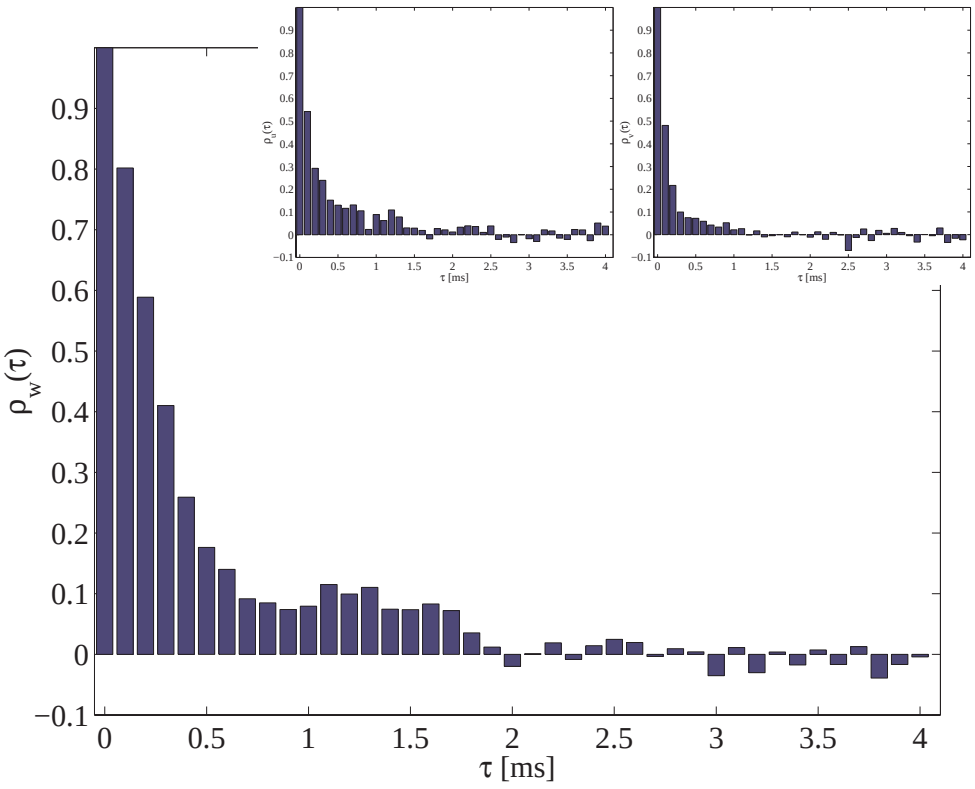

Figure 9.24: Autocorrelation coefficient for w at x/d =2 and y/d =0.06. The top figure at the top left is the autocorrelation coefficient for u and the top right figure is the autocorrelation coefficient for v.

A measurement in one point was usually completed in 10-20 seconds. An averaged time between samples calculated from this data rate is 2-4 ms. The integral time scales indicate that a sufficient number of independent samples were taken, at least in this point.

9.4.4 Reynolds shear stress $\overline{uv}$

Shear stress $\overline{uv}$ is plotted in figure 9.15 on page 75. This figure shows that positive values are present in the windward shear layer and also, interestingly enough, in a band close to the wall on the lee side of the pipe exit, continuing far downstream. This shear stress has its origin in the boundary layer in the pipe. Immediately above the windward shear layer is a small band of negative $\overline{uv}$ from the oncoming flat plate boundary layer. A band of negative $\overline{uv}$ from the upstream jet is visible above the studied jet. In a yz-plane this band has a bent shape, like a banana. There are large negative values of $\overline{uv}$ in the leeward shear layer. Positive values are found for a short distance downstream at the sides (higher z positions) of this band of negative $\overline{uv}$. In the far field downstream, the banana-formed band (in the yz-plane) of negative $\overline{uv}$ dominates.

9.4.5 Reynolds shear stress $\overline{uw}$

Figures 9.16 on page 76 (x =0 and x =1 planes) and 9.17 on page 77 show shear stress $\overline{uw}$. (Note that measurements were made only for z/d >0.) Owing to symmetry, $\overline{uw}$ is zero on the center plane, z =0. Negative $\overline{uw}$ correlations are seen in a band like an arc in the yz-plane in the windward shear layer between x/d =-1 and $x/d \approx 0$ at the sides of the jet for positive z, and positive $\overline{uw}$ correlations are seen for negative z. Further downstream, between $x/d \approx 0$ and $x/d \approx 1$ for positive z, positive $\overline{uw}$ correlations are seen between the jet and the negative band of $\overline{uw}$. A very narrow band of strong negative $\overline{uw}$ correlations for positive z-values starts behind $x/d \approx 1$. This band grows downstream and evolves into 'kidney-shaped' regions in the yz-plane. For positive z, there is a kidney shaped region with negative $\overline{uw}$ that is anti-symmetric with regard to the center plane. The orientations of these kidney shaped bands are rotated 90 degrees as compared to the kidney shaped $\overline{uv}$ band described previously. The $\overline{uw}$ bands from the upstream jet are visible above the studied jet.

9.4.6 Reynolds shear stress $\overline{vw}$

Shear stress $\overline{vw}$ is plotted in figures 9.18 on page 78 (x =0 and x =1 planes) and 9.19 on page 79. Shear stress $\overline{vw}$ is also anti-symmetric with regard to the z =0 plane in the same way as $\overline{uw}$. The windward shear layer shows no region of high $\overline{vw}$. After $x/d \approx 0$ positive $\overline{vw}$ is found near the hole orifice for positive z. This region elevates as the x-coordinate is increased. After approximately x/d =1.5, a region with negative $\overline{vw}$ starts under the region mentioned before. The culmination of the negative $\overline{vw}$ region occurs just after the node/saddle point. Further downstream, the positive $\overline{vw}$ region grows again while the negative region diminishes. In total, four lobes of $\overline{vw}$ are found in the yz-plane far downstream.

9.5 Production of Reynolds stresses

The production of $\overline{u_i u_j}$ is denoted P_{ij}.

$$P_{ij} = -\overline{u_i u}_k \frac{\partial \overline{U}_j}{\partial x_k} - \overline{u_j u}_k \frac{\partial \overline{U}_i}{\partial x_k} \tag{9.5}$$

More explicitly, we have, with the most dominating terms in boxes:

$$\begin{cases} P_{11} = -\boxed{2\overline{u^2}\,\frac{\partial \overline{U}}{\partial x}} - \boxed{2\overline{uv}\,\frac{\partial \overline{U}}{\partial y}} - 2\overline{uw}\frac{\partial \overline{U}}{\partial z} \\ P_{22} = -2\overline{uv}\frac{\partial \overline{V}}{\partial x} - \boxed{2\overline{v^2}\,\frac{\partial \overline{V}}{\partial y}} - 2\overline{vw}\frac{\partial \overline{V}}{\partial z} \\ P_{33} = -2\overline{uw}\frac{\partial \overline{W}}{\partial x} - 2\overline{vw}\frac{\partial \overline{W}}{\partial y} - \boxed{2\overline{w^2}\,\frac{\partial \overline{W}}{\partial z}} \\ P_{12} = -\boxed{\overline{u^2}\,\frac{\partial \overline{V}}{\partial x}} - \overline{uv}\frac{\partial \overline{V}}{\partial y} - \overline{uw}\frac{\partial \overline{V}}{\partial z} - \overline{uv}\frac{\partial \overline{U}}{\partial x} - \boxed{\overline{v^2}\,\frac{\partial \overline{U}}{\partial y}} - \overline{vw}\frac{\partial \overline{U}}{\partial z} \\ P_{13} = -\overline{u^2}\frac{\partial \overline{W}}{\partial x} - \overline{uv}\frac{\partial \overline{W}}{\partial y} - \boxed{\overline{uw}\,\frac{\partial \overline{W}}{\partial z}} - \overline{uw}\frac{\partial \overline{U}}{\partial x} - \overline{vw}\frac{\partial \overline{U}}{\partial y} - \boxed{\overline{w^2}\,\frac{\partial \overline{U}}{\partial z}} \\ P_{23} = -\overline{uv}\frac{\partial \overline{W}}{\partial x} - \boxed{\overline{v^2}\,\frac{\partial \overline{W}}{\partial y}} - \overline{vw}\frac{\partial \overline{W}}{\partial z} - \overline{uw}\frac{\partial \overline{V}}{\partial x} - \overline{vw}\frac{\partial \overline{V}}{\partial y} - \boxed{\overline{w^2}\,\frac{\partial \overline{V}}{\partial z}}. \end{cases} \tag{9.6}$$

All the terms in P_{ij} aft of the jet in the center plane z/d =0 are plotted in figures 9.25 on the following page to 9.27 on page 92. Note that all terms including $\overline{uw}$, $\overline{vw}$, $\partial \overline{U}/\partial z$ and $\partial \overline{V}/\partial z$ are zero in the z/d =0 plane due to the symmetry condition. Production term P_{ij} in the wake in the center plane z/d =0 is plotted in figure 9.28 on page 93. It is noted that a significant

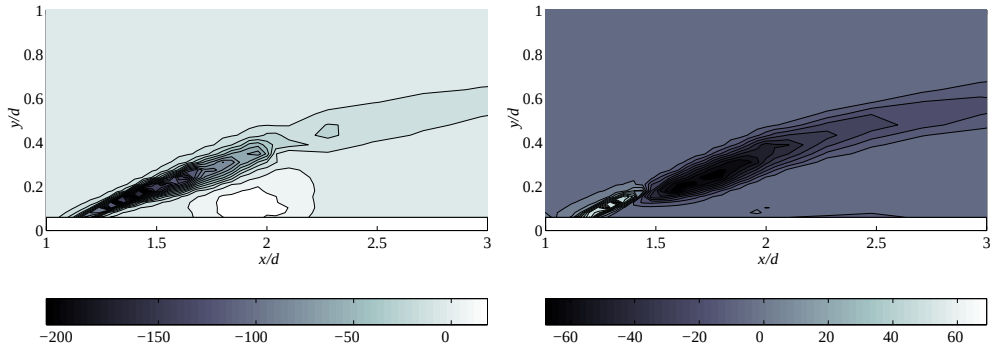

(a) $\overline{u^2}\,\frac{\partial \overline{U}}{\partial x}$ (in the P_{11} term) (b) $\overline{uv}\,\frac{\partial \overline{U}}{\partial y}$ (in the P_{11} term)

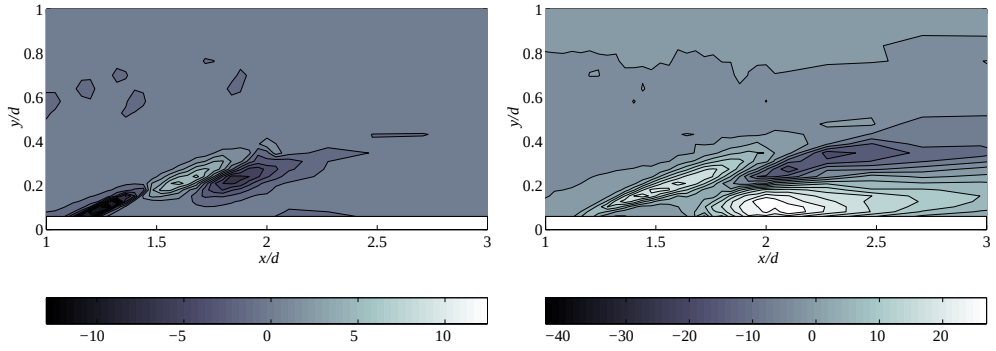

(c) $\overline{uv}\,\frac{\partial \overline{V}}{\partial x}$ (in the P_{22} term) (d) $\overline{v^2}\,\frac{\partial \overline{V}}{\partial y}$ (in the P_{22} term)

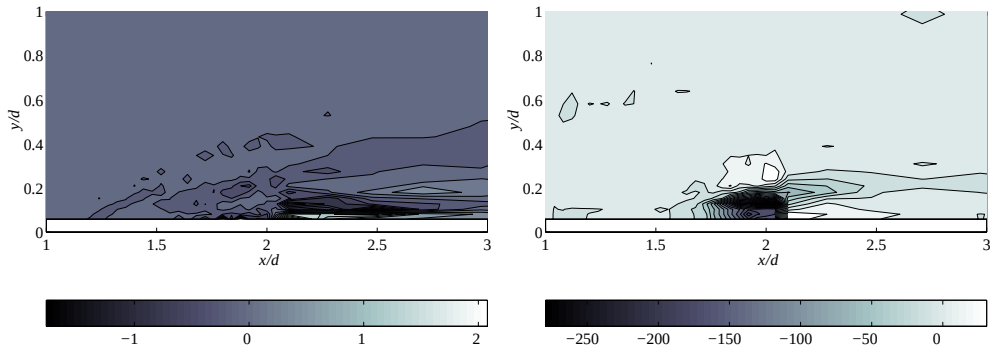

(e) $\overline{vw}\,\frac{\partial \overline{W}}{\partial y}$ (in the P_{33} term) (f) $\overline{w^2}\,\frac{\partial \overline{W}}{\partial z}$ (in the P_{33} term)

Figure 9.25: Production terms in the z/d =0 plane after the injection hole. The rear edge of the injection hole is located at x/d =1.

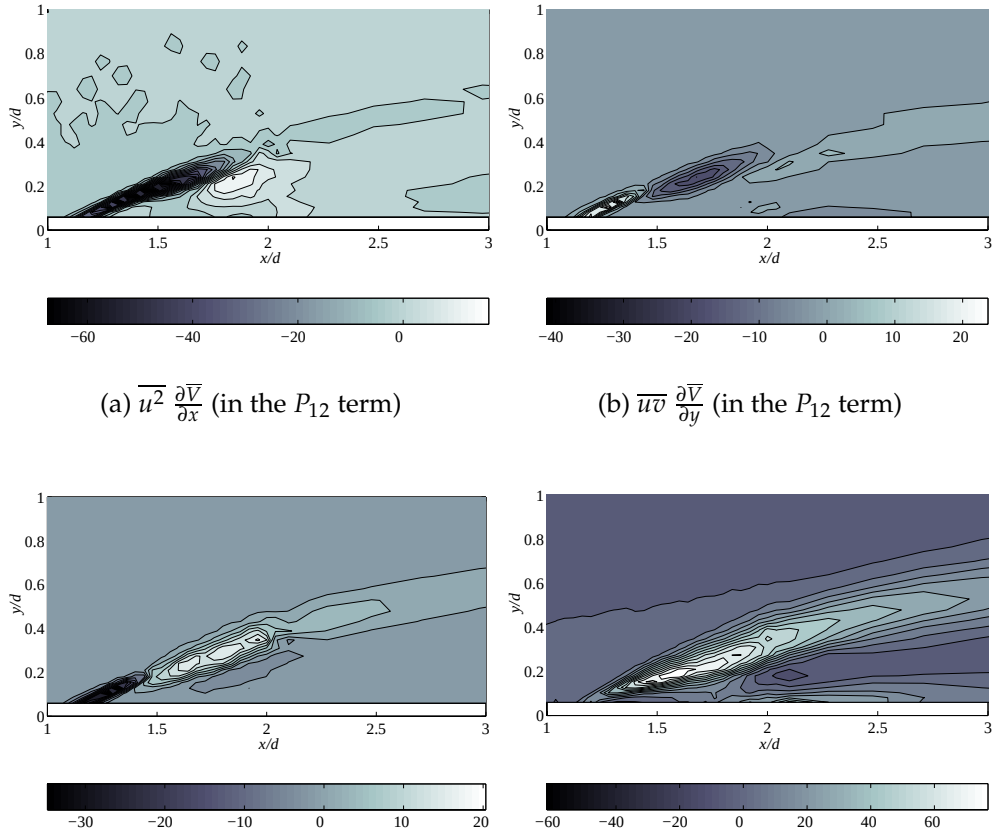

(a) $\overline{u^2}\,\frac{\partial \overline{V}}{\partial x}$ (in the P_{12} term)

(b) $\overline{uv}\,\frac{\partial \overline{V}}{\partial y}$ (in the P_{12} term)

(c) $\overline{uv}\,\frac{\partial \overline{U}}{\partial x}$ (in the P_{12} term)

(d) $\overline{v^2}\,\frac{\partial \overline{U}}{\partial y}$ (in the P_{12} term)

Figure 9.26: Production terms in the z/d =0 plane after the injection hole. The rear edge of the injection hole is located at x/d =1.

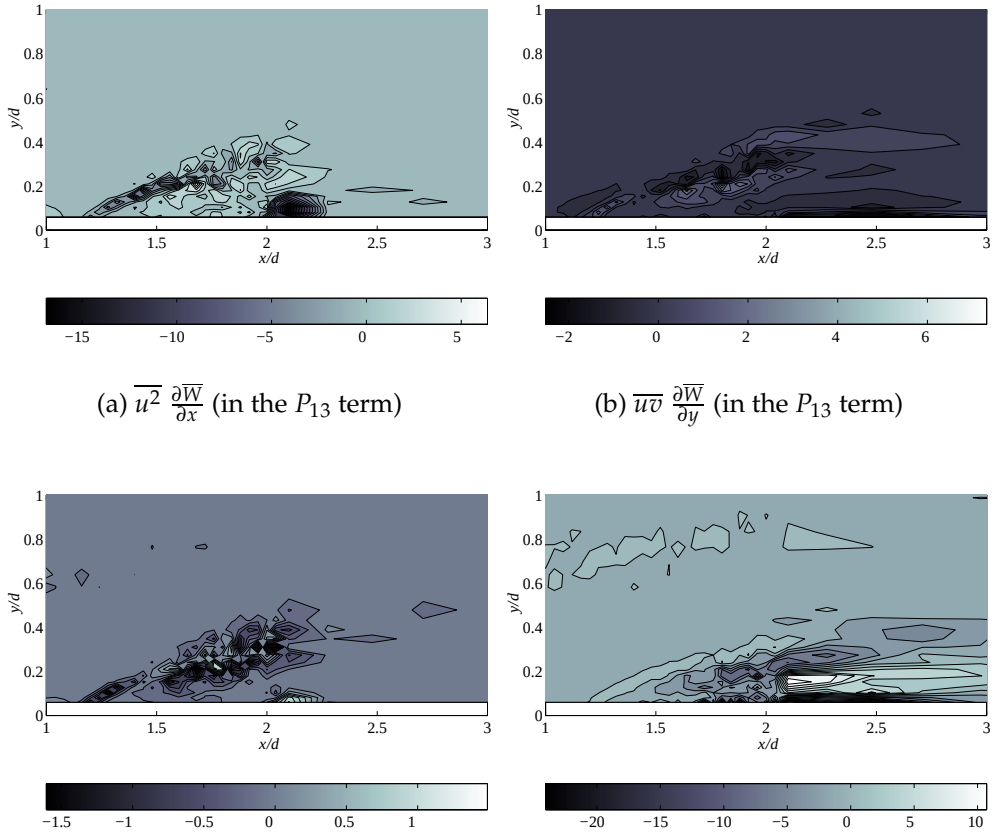

(a) $\overline{u^2}\,\frac{\partial \overline{W}}{\partial x}$ (in the P_{13} term)

(b) $\overline{uv}\,\frac{\partial \overline{W}}{\partial y}$ (in the P_{13} term)

(c) $\overline{uv}\,\frac{\partial \overline{W}}{\partial x}$ (in the P_{23} term)

(d) $\overline{v^2}\,\frac{\partial \overline{W}}{\partial y}$ (in the P_{23} term)

Figure 9.27: Production terms in the z/d =0 plane after the injection hole. The rear edge of the injection hole is located at x/d =1.

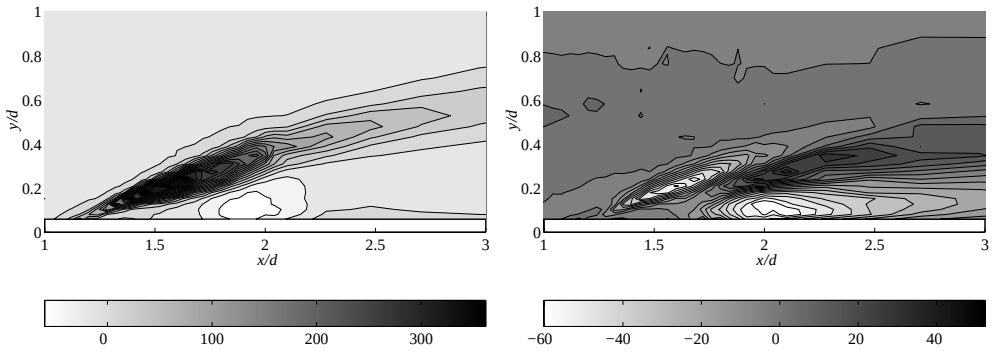

(a) P_{11}

(b) P_{22}

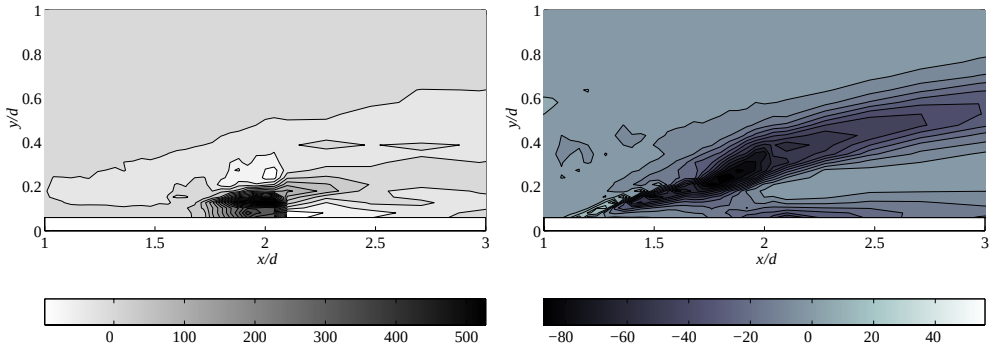

(c) P_{33}

(d) P_{12}

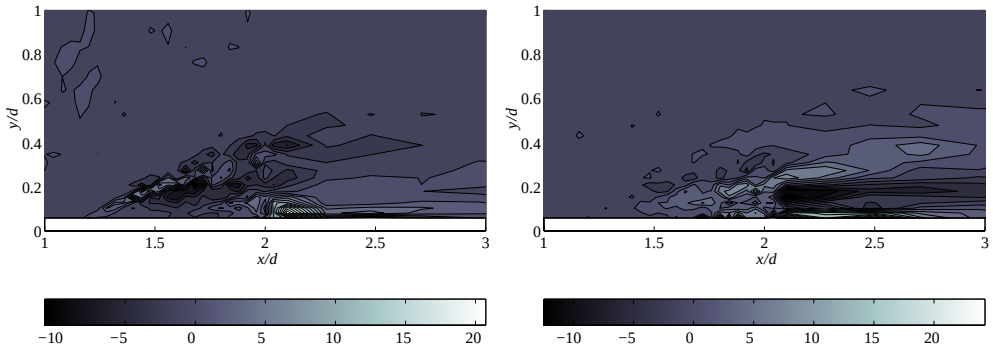

(e) P_{13}

(f) P_{23}

Figure 9.28: Production of normal and shear stresses in the z/d =0 plane after the injection hole. The rear edge of the injection hole is located at x/d =1.

contribution to the production of $\overline{u_i u_j}$ is always due to the term containing the mean velocity derivative $\partial \overline{U}_i / \partial x_j$, with corresponding indices i and j.

The production of Reynolds normal stress $\overline{u^2}$ seems to be dominated by two terms, $\overline{u^2}\ \partial \overline{U}/\partial x$ and $\overline{uv}\ \partial \overline{U}/\partial y$, in the leeward shear layer under the jet in the wake. The $\overline{u^2}\ \partial \overline{U}/\partial x$ term is negative in the leeward shear layer and slightly negative near the node point at x/d =1.8-2. The $\overline{uv}\ \partial \overline{U}/\partial y$ term has positive values (negative production of $\overline{uv}$) from x/d =1 to x/d =1.45 in the leeward shear layer. At x/d =1.45, the $\overline{uv}\ \partial \overline{U}/\partial y$ term changes into positive values. The P_{11} term is positive in the leeward shear layer with a maximum at x/d =1.6 and y/d =0.22. A minimum with negative values was found at x/d =1.9 and y/d =0.1.

The $\overline{v^2}\ \partial \overline{V}/\partial y$ term is the most important for the production of the $\overline{v^2}$ stress. The $\overline{uv}\ \partial \overline{V}/\partial x$ term is negative in the leeward shear layer close to the orifice. Further out in the shear layer at x/d =1.45 and y/d =0.18, the term changes sign and becomes negative.

The $\overline{w^2}\ \partial \overline{W}/\partial z$ term is the most important one for the production of normal stress $\overline{w^2}$.

The production of $\frac{1}{2}\overline{u_i u_i}$ was primarily positive and dominated in regions of high shearing and after the foci, near the unstable node/saddle point.

The production terms of shear stress $\overline{uv}$ in the center plane are plotted in figure 9.26 on page 91. The dominating terms are $\overline{u^2}\ \partial \overline{V}/\partial x$ and $\overline{v^2}\ \partial \overline{U}/\partial y$, but the $\overline{uv}\ \partial \overline{V}/\partial y$ and $\overline{uv}\ \partial \overline{U}/\partial x$ terms are not negligible. Andreopoulos & Rodi (1984) write that gradient $\partial \overline{U}/\partial y$ is closely related to $\overline{uv}$ and $\frac{1}{2}\overline{u_i u_i}$. Pietrzyk *et al.* (1990) and Thole *et al.* (1997) drew the same conclusion.

The production of shear stress $\overline{uw}$ in the center plane is shown in figure 9.27a and 9.27b on page 92. In the z/d =0 plane, the $\overline{uv}\ \partial \overline{W}/\partial y$ and the $\overline{u^2}\ \partial \overline{W}/\partial x$ terms were dominant in the production of $\overline{uw}$. Andreopoulos & Rodi report that terms containing gradients $\partial \overline{U}/\partial z$ and $\partial \overline{W}/\partial y$ dominate the production of $\overline{uw}$.

Finally, the production of shear stress $\overline{vw}$ in the center plane is shown in figure 9.27c and 9.27d. Little contribution was encountered from the $\overline{uv}\ \partial \overline{W}/\partial x$ term to the production of the $\overline{vw}$ correlation. Andreopoulos & Rodi found gradients $\partial \overline{V}/\partial z$ and $\partial \overline{W}/\partial y$ to be important. This is the same result as reported in this thesis.

9.5.1 Validity of the Boussinesq assumption

The intention of this section is to examine whether the stresses and the main strain rate have opposite signs, as assumed in eddy viscosity modeling and in the Boussinesq assumption. Andreopoulos & Rodi (1984) report that this does not hold in the wake of the jet and that models such as the $k-\varepsilon$ and $k-\omega$ are incapable of predicting the jet in the crossflow flow field ($\nu_t = \text{const} \cdot k^2/\varepsilon$). In agreement with their conclusion, it can be seen in the measurements reported in this thesis that $\overline{uv}$ and $\partial\overline{U}/\partial y + \partial\overline{V}/\partial x$ have in fact the *same* sign in the leeward shear layer near the hole exit, see figure 9.15 on page 75 (near x/d =1, y/d =0.06 and z/d =0). In this shear layer, $\partial\overline{U}/\partial y + \partial\overline{V}/\partial x$ is strictly positive but $\overline{uv}$ changes sign from positive near the hole exit to negative further out.

9.6 Pressure field

A very useful parameter for the understanding of the physical processes in the flowfield is the pressure gradient vector field. This vector parameter directly relates to the forces the fluid is subjected to. The density is almost constant for T_0/T_c=1 and it is possible to deduce the pressure field if all components of the velocity gradients and Reynolds stress gradients are known. This is impossible if density differences are present and no recordings of the density fluctuations are made. It is apparent in the literature that the jet in crossflow is believed to be dominated by pressure forces. All terms in the Reynolds averaged Navier-Stokes equation were estimated from the measurements and balanced in order to acquire an indirect measurement of the mean pressure gradients. These gradients were integrated to obtain the mean pressure field. The integration was done by minimizing the difference between gradients estimated from measurements and a first order finite difference, in a least squares meaning. This is described in appendix D.

The advection terms, $\overline{U}_j\overline{U}_{i,j}$, and the turbulent stress terms, $\overline{u_iu}_{j,j}$, in the Reynolds averaged Navier-Stokes equation were compared. It was clear from this that the main contribution to the pressure gradient was often the advection terms. The viscous terms were found to be small compared with the other terms. The turbulent stress gradients were large in the shear layer of the jet in the wake, of the same order of magnitude as the advection terms, but always less than the advection terms. The balance between advection terms and the turbulent stress terms is the origin of the pressure gradient.

Mean pressure gradient in the x-direction

In the windward shear layer, the $\overline{U}\partial\overline{U}/\partial x$ term dominated, with large positive values, except a small area close to the wall upstream of the jet with negative values. In this shear layer $\overline{V}\partial\overline{U}/\partial y$ was negative, with an area of positive values above (higher y/d). The leeward shear layer showed negative values of $\overline{U}\partial\overline{U}/\partial x$ and positive values of $\overline{V}\partial\overline{U}/\partial y$. The turbulent stresses were largest in the leeward shear layer. Here $\partial\overline{u^2}/\partial x$ was in two bands, one negative and a positive one above. The appearance in the case of $\partial\overline{uv}/\partial y$ was similar with an additional region of positive/negative values in the upwind shear layer. Finally, $\partial\overline{uw}/\partial z$ was found to be negative in a large band close to the wall after the maximum of $\overline{w^2}$ (after x/d =2).

Mean pressure gradient in the y-direction

Large positive $\overline{U}\partial\overline{V}/\partial x$ values were observed in the upstream shear layer, and large negative values in the leeward. The opposite picture was found for $\overline{V}\partial\overline{V}/\partial y$. The last advection term, $\overline{W}\partial\overline{V}/\partial z$, was negative in front of the jet close to the wall for positive z. This term changed sign further downstream, in the wake. A small contribution to $\partial\overline{P}/\partial y$ was found to arise from the turbulent stresses. The most dominant turbulent stress was $\partial\overline{v^2}/\partial y$, in the shear layer. A positive band was found in both shear layers underneath (lower y/d) a negative band.

Mean pressure gradient in the z-direction

An area with positive $\overline{U}\partial\overline{W}/\partial x$ was found in front of the jet for positive z close to the wall. This area was immediately followed by an area closer to the pipe orifice with negative values.

Mean pressure field

There is a high pressure region in front of the jet, that is marked red in figures 9.21 on page 81 and 9.22 on page 82. The high pressure deflects the cross flow fluid around the jet and causes the jet to deflect downward. At a somewhat lower pressure, indicated by a yellow isosurface in figures 9.21 and 9.22, it is obvious from the figures that there is a low pressure region in the counter-rotating vortex pair. The low pressure in the counter-rotating vortex pair acts as an opposing force to the centrifugal force, the *cyclostrophic balance*. When the pressure is further decreased, indicated by blue isosurfaces, we can see that the lowest pressure is in the side vortex and the foci, in order to balance the centrifugal forces. There is also a low

pressure region at the pipe exit, causing the jet to deflect downward. The counter-rotating vortex pair counteracts this effect by its upward motion owing to induction of the vortex pair. Andreopoulos & Rodi (1984) also conclude this. Negative pressure coefficient, C_P, values as low as -0.3 occur on the lee side of the jet. Bergles *et al.* (1976) reported a pressure coefficient of -2 in the wake. A rather unusual definition of the pressure coefficient was however used. Expressed in the same way as here the pressure coefficient reported by Bergles *et al.* was -0.48. An explanation for the difference can be that Bergles *et al.* studied an orthogonal jet in crossflow, which requires a higher pressure force for the deflection of the jet.

It is interesting to see that there is an overall pressure drop in the test section. The highest pressure levels were found in the most upstream positions and the lowest in the most downstream positions.

Chapter 10

Conclusions

A complete mapping of the 3D velocity and turbulence fields was made in a volume around a jet in the third row of holes on an effusion cooled plate. The operational parameters were: isothermal conditions at 24°C, Re_{jet}=5800, U_{jet}^{max}/U_0=0.89 and the design parameters; injection angle, α=30° and hole diameter, d=5.2 mm. The three velocity components and the complete turbulent stress tensor were measured in 35340 points around and behind the jet. Such a complete experimental mapping of the velocity field and turbulence field has not, to the best of the knowledge of the author, been presented before. It is possible to draw conclusions from these measurements as to the structure of the topology of the mean flow field and the structure of the turbulence fields.

1. Two counter-rotating foci were found in the wake of the jet. An unstable node/saddle point was found at x/d =1.78 and y/d =0.09 on the center plane. A similar critical point should exist on the wall just below. The saddle points are partly responsible for the good mixing properties of the jet in crossflow. A vortex at each side of the jet was found. This vortex and the focus vortex spiral around each other for a short distance. They align further downstream to create the counter-rotating vortex pair.

2. The coolant and crossflow fluid mix very efficiently in the mean flow field. The presence of saddle points in the wake, and two co-rotating vortices on each side of the center plane, enhance the mixing capabilities. This is not advantageous from a film-cooling perspective. It must be advantageous to use low jet velocities so that the jet does not separate from the wall and so that the formation of vortices is minimal. This is clearly the conclusion in part I where the 'almost' transpiration cooling situation with small $\delta x/d$ and many holes proved

to be very effective. In these cases the jet velocities were very low.

3. High local turbulence levels, 25%, were found in the wake of the jet close to the wall. Here, the joint PDF of (U,W) showed that high-speed crossflow fluid sweeps in from the sides below the jet. Pietrzyk *et al.* (1990) and Thole *et al.* (1997) reported that $\partial\overline{U}/\partial y$ was great in areas where $\overline{uv}$ was great. The present study supports this except that a change in sign of $\overline{uv}$ in the leeward shear layer near the hole exit was seen. Great negative values of $\overline{u^2}\,\partial\overline{V}/\partial x$ was found near the pipe orifice ($\overline{v^2}\,\partial\overline{U}/\partial y$ is positive here), which also contributed to the production of $\overline{uv}$.

4. The boundary layer vorticity is turned in the stream-wise direction at the sides of the jet. Closed vortex-lines were found in the pipe. In the far wake, the vortex lines formed arcs. Beltrami flow was found at the sides of the injection hole.

5. The Reynolds equation was balanced and the pressure gradients were estimated. A numerical scheme was constructed to calculate the pressure field. Regions of high pressure were found in front of the jet and low pressure regions were found in the cores of the vortices. A pressure coefficient of -0.3 was found. An overall pressure drop was observed in the test section.

10.1 Future work

1. Detailed investigation of the flow field for $\rho_{jet}U_{jet}/\rho_0 U_0$=0.4, which has shown better film cooling performance.

2. Measurements with density effects, T_0/T_c=1.5-2, which introduces new physical effects. In effusion cooling of combustion chamber walls, the density ratio is usually around 2.

3. Simultaneous measurements (LIF +LDA) of temperature or density and velocity in order to estimate the temperature/velocity correlations, $\overline{\theta u_i}$, and the Reynolds stresses, $\overline{\rho u_i u_j}$.

4. Use of more global measurement techniques such as flow visualization or PIV to be able to study the instantaneous events. Surface oil streak visualization can be made for a better understanding of the topology, even inside the holes. The way which the topology changes with the blowing ratio can also be studied in this way.

5. Use of the LDA data presented here for validation of numerical simulations of film cooling and jet in crossflow. The data can be used to make models for film cooling boundary conditions e.g. source term modeling for the inclusion of coolant in film cooling, as described in the thesis of Dahlander (2001). The thermographical data in part I have been used by Dahlander (1999).

Bibliography

ANDREOPOULOS, J. & RODI, W. 1984 Experimental investigation of jets in a crossflow. *Journal of Fluid Mechanics* **138**, 93–127.

ADRIAN, R. J. 1996 Ch 4 - Laser velocimetry. In *Fluid Mechanics Measurements, Second Edition*, Editor R. J. Goldstein, pp. 175–299.

BAZDIDI-TEHRANI, F. & ANDREWS, G. E. 1994 Investigation of the effect of variable density ratio. *Journal of Engineering for Gas Turbines and Power* **116**, 587–596.

BERGLES, G., GOSMAN, A. D. & LAUNDER, B. E. 1976 The near-field character of a jet discharged normal to a main stream. *Trans. ASME C: J. Heat Transfer* **98**, 373–378.

CHEN, A. L., JACOB, J. D. & SAVAŞ, Ö 1999 Dynamics of corotating vortex pairs in the wake of flapped airfoils. *Journal of Fluid Mechanics* **382**, 155–193.

CHO, H. H. & GOLDSTEIN, R. J. 1995 Heat (Mass) transfer and film cooling effectiveness with injection through discrete holes: Part I - Within holes and on the back surface. *Journal of Turbomachinery* **117**, 440–450.

CHO, H. H. & GOLDSTEIN, R. J. 1995 Heat (Mass) transfer and film cooling effectiveness with injection through discrete holes: Part II - On the exposed surface. *Journal of Turbomachinery* **117**, 451–460.

COELHO, S. L. V. & HUNT, J. C. R. 1989 The dynamics of the near field of strong jets in crossflows. *Journal of Fluid Mechanics* **200**, 95–120.

COLLADAY, R. S. & RUSSELL, L. M. 1976 Streakline flow visualization of discrete hole film cooling for gas turbine applications. *Journal of Heat Transfer* **98**, 245–250.

CHONG, M. S., PERRY, A. E. & CANTWELL B. J. 1989 A general classification of three-dimensional flow fields. In *Topological Fluid Dynamics*. Proceedings of the IUTAM Symposium, Cambridge, 13-18 August 1989.

CRABB, D., DURÃO, D. F. G. & WHITELAW, J. H. 1981 A round jet normal to a crossflow. *Journal of Fluids Engineering* **103**, 142–153.

CRAWFORD, M. E., KAYS, W. M & MOFFAT, R. J. 1976 Heat transfer to a full-coverage film-cooled surface with 30-deg. slant hole injection. Stanford Univ., *Mech. Engrg. Dept. Rep.* HMT-25.

DAHLANDER, PETTER 1999 Numerical simulation of effusion-cooled plates using an injection model. ISABE conference, Florence, Italy - September 5-10, 1999, *IS-218*.

DAHLANDER, PETTER 2001 PhD thesis to appear. Department of Thermo and Fluid Dynamics, Chalmers University of Technology. Göteborg, Sweden.

DURST, F., MELLING, A., & WHITELAW, J. H. 1981 Principles and Practice of Laser-Doppler Anemometry, Second Edition. *Academic Press*.

DURST, F., MARTINUZZI, R., SENDER, J. & THEVENIN, D. 1992 LDA-measurements of mean velocity, RMS-values and higher order moments of turbulence intensity fluctuations in flow fields with strong velocity gradients. *6^{th} International Symposium on Applications of Laser Techniques to Fluid Mechanics*, July 20^{th}-23^{rd}, 1992, Lisbon, Portugal.

ECKERT, E. R. G. & LIVINGOOD, J. N. B. 1954 Comparison of effectiveness of convection-, transpiration-, and film-cooling methods with air as coolant. *NACA Rep.* 1182.

ECKERT, E. R. G. 1984 Analysis of film cooling and full coverage film cooling of gas turbine blades. *Journal of Engineering for Gas Turbines and Power* **106**, 206–213.

ECKERT, E. R. G. & CHO, H. H. 1994 Transition from transpiration to film cooling. *Int. J. Heat Mass Transfer* **37**(1), 3–8. Corrigenda in **38**(1), 183.

EIFF, O. S. & KEFFER, J. F. 1997 On the structure in the near-wake region of an elevated turbulent jet in a crossflow. *Journal of Fluid Mechanics* **333**, 161–195.

FOSS, J. F. 1980 Interaction region phenomena for the jet in cross-flow problem. *SFB 80/E/161*, Universität Karlsruhe.

FOSTER, N. W. & LAMPARD, D. 1980 The flow and film cooling effectiveness following injection through a row of holes. *Journal of Engineering for Power* **102**, 584–588.

FRIC, T. F. & ROSHKO, A. 1994 Vortical structure in the wake of a transverse jet. *Journal of Fluid Mechanics* **279**, 1–47.

FRIEDRICHS, S., HODSON, H. P. & DAWES, W. N. 1996 Distribution of film-cooling effectiveness on a turbine endwall measured using the ammonia and diazo technique. *Journal of Turbomachinery* **118**(4), 613–621.

GEORGE JR., WILLIAM K. 1976 Limitations to measuring accuracy inherent in the laser Doppler signal. *Proceedings of the LDA-Symposium, Copenhagen 1975*

GOLDSTEIN, R. J. & STONE, L. D. 1997 Row-of-hole film cooling of curved walls at low injection angles. *Journal of Turbomachinery* **119**, 574–579.

GRITSCH, M., SCHULZ, A. & WITTIG, S. 1998 Adiabatic wall effectiveness measurements of film-cooling holes with expanded jets. *Journal of Turbomachinery* **120**(3), 549–556.

GRITSCH, M., SCHULZ, A. & WITTIG, S. 1998 Discharge coefficient measurements of film-cooling holes with expanded exits. *Journal of Turbomachinery* **120**(3), 557–563.

GUSTAFSSON, K. M. BERNHARD 1998 An experimental study of the surface temperature of an effusion-cooled plate using infrared thermography. Thesis for the degree of Licentiate in Engineering. *Publication no. 98/9*. Department of Thermo and Fluid Dynamics, Chalmers University of Technology. Göteborg, Sweden.

HOWELL, JOHN R. A. 1982 In *A Catalog of Radiation Configuration Factors*. McGraw-Hill Book Company.

HUNT, J. C. R., ABELL, C. J., PETERKA, J. A. & WOO, H. 1978 Kinematic studies of the flows around free or surface-mounted obstacles; applying topology to flow visualization. *Journal of Fluid Mechanics* **86**(1), 179–200.

JEONG, J. & HUSSAIN, F. 1995 On the identification of a vortex. *Journal of Fluid Mechanics* **285**, 69–94.

KELSO, R. M., LIM, T. T. & PERRY, A. E. 1996 An experimental study of round jets in a cross-flow. *Journal of Fluid Mechanics* **306**, 111–144.

LEBROCQ, P. V., LAUNDER, B. E. & PRIDDIN, C. H. 1971 Discrete hole injection as means of transpiration cooling – An experimental study. *Imp. Coll. Rep.* HTS/71/37.

LEONTIEV, A. I. 1999 Heat and mass transfer problems for film cooling. *Journal of Heat Transfer* **121**(3), 509–527.

LIGRANI, P. M. & RAMSEY, A. E. 1997 Film cooling from spanwise-oriented holes in two staggered rows. *Journal of Turbomachinery* **119**, 562–567.

MARTINY, M., SCHULZ, A. & WITTIG, S. 1995 Full-coverage film cooling investigations: Adiabatic wall temperatures and flow visualization. ASME International Mechanical Engineering Congress & Exposition San Francisco - November 12-17, 1995 95-WA/HT-4.

MCLAUGHLIN, D. K. & TIEDERMAN, W. G. 1973 Bias correction for individual realization of laser anemometer measurements in turbulent flows. *The Physics of Fluids* **16**(12), 2082–2088.

MODEST, MICHAEL F. 1993 *Radiative Heat Transfer*. McGraw-Hill, Inc.

MOUSSA, Z. M., TRISCHKA, J. W. & ESKINAZI, A. 1977 The near field in the mixing of a round jet with a cross-stream *Journal of Fluid Mechanics* **80**, 49–80.

PERRY, A. E. & CHONG, M. S. 1987 A description of eddying motions and flow patterns using critical-point concepts. *Annual Review of Fluid Mechanics* **19**, 125–155.

PIETRZYK, J. R., BOGARD, D. G. & CRAWFORD, M. E. 1990 Effects of density ratio on the hydrodynamics of film cooling. *Journal of Turbomachinery* **112**(39), 437–443.

RYDHOLM, HANS A. 1995 Effusion cooling of combustor walls - An experimental investigation of the velocity and temperature fields of cold jets injected into a hot cross flow. Thesis for the degree of Licentiate in Engineering. *Publication no. 95/7*. Department of Thermo and Fluid Dynamics, Chalmers University of Technology. Göteborg, Sweden.

SALCUDEAN, M. , GARTSHORE, I., ZHANG, K. & MCLEAN, I. 1994 An experimental study of film cooling effectiveness near the leading edge of a turbine blade. *Journal of Turbomachinery* **116**, 71–79.

SAMUEL, A. E. & JOUBERT, P. N. 1965 Film cooling of an adiabatic flat plate in zero pressure gradient in the presence of a hot mainstream an cold tangential secondary injection. *Journal of Heat Transfer* **87**, 409–419.

SASAKI, M., TAKAHARA, K., KUMAGAI, T. & HAMANO, M. 1979 Film cooling effectiveness for injection from multirow holes. *Journal of Engineering for Power* **101**, 101–108.

THOLE, K. A., GRITSCH, M., SCHULZ, A. & WITTIG, S. 1997 Effect of crossflow at the entrance to a film-cooling hole. *Journal of Fluids Engineering* **119**, 533–540.

YAVUZKURT, S., MOFFAT, R. J. & KAYS, W. M. Full-coverage film cooling. Part 1. Three-dimensional measurements of turbulence structure. *Journal of Fluid Mechanics* **101**, 129–158.

YAVUZKURT, S., MOFFAT, R. J. & KAYS, W. M. Full-coverage film cooling. Part 2. Prediction of the recovery-region hydrodynamics. *Journal of Fluid Mechanics* **101**, 159–178.

Nomenclature

a_{ij}	rate of deformation tensor [1/s]
A	area [m^2]
b	thickness of test plate [m]
B	width of test section [m]
c	speed of light in vacuum [m/s]
C_P	pressure coefficient $(P - P_{ref})/(\frac{1}{2}\rho U_0^2)$
c_p	specific heat at constant pressure [J/(kg·K)]
c_v	specific heat at constant volume [J/(kg·K)]
d	diameter of injection holes [m]
E	blackbody emitted heat flux [W/m^2]
$\mathbf{E}_{0l}$	illuminating electric vector [V/m]
e_{ij}	rate of strain tensor [1/s]
F_{ij}	view factor
h	Planck's constant [J·s]
H	the irradiated heat flux [W/m^2]
H_1	height of the test section [m]
H_2	height of the plenum chamber [m]
$I_{b\eta}$	blackbody intensity at wavenumber η [$W/(m^2 \cdot m^{-1} \cdot sr)$]
I_η	intensity at wavenumber η [$W/(m^2 \cdot m^{-1} \cdot sr)$]
J	leaving heat flux [W/m^2]
k	Boltzmann's constant [J/K]
k	$\frac{1}{2}\overline{u_i u_i}$
L	the length of the test section or the length of the injection pipe[m]
m	an integer
M	mass flux ratio $\rho_{jet} U_{jet}/\rho_0 U_0$
Ma	Mach number
n	an integer

$\widehat{\mathbf{n}}$	normal unit vector
$\vec{n}$	normal unit vector
P	first invariant of a_{ij}
$\overline{P}$, p	pressure [Pa]
P_{ij}	production of $\overline{u_i u}_j$
Pr	Prandtl number
q_j	heat flux vector due to conduction [W/m^2]
q_j^r	heat flux vector due to radiation [W/m^2]
Q	second invariant of a_{ij}
R	gas constant [J/(kg·K)]
R	third invariant of a_{ij}
Re	Reynolds number
r_{ij}	distance between surface dA_i and surface dA_j
S_{ij}	rate of strain tensor [1/s]
S_λ	parameter in Sutherland's law for thermal conductivity [K]
S_μ	parameter in Sutherland's law for viscosity [K]
$\widehat{\mathbf{s}}$	direction unit vector
t	time [s]
T	temperature [K] or [°C]
$\mathcal{T}_u$	integral time scale of u. $\mathcal{T}_u = \int_0^{+\infty} \rho_u(\tau) d\tau$ where $\rho_u(\tau)$ is the autocorrelation coefficient for u.
$\mathcal{T}_v$	integral time scale of v. $\mathcal{T}_v = \int_0^{+\infty} \rho_v(\tau) d\tau$ where $\rho_v(\tau)$ is the autocorrelation coefficient for v.
$\mathcal{T}_w$	integral time scale of w. $\mathcal{T}_w = \int_0^{+\infty} \rho_w(\tau) d\tau$ where $\rho_w(\tau)$ is the autocorrelation coefficient for w.
u_i	velocity in direction x_i [m/s]
u_*	friction velocity $(\tau_w/\rho)^{1/2}$ [m/s]
u	stream-wise velocity component [m/s]
v	wall normal velocity component [m/s]
$\mathbf{V}$	velocity vector [m/s]
w	span-wise velocity component [m/s]
x_i	spatial coordinate [m]
x	stream-wise coordinate [m]
y	wall normal coordinate [m]
z	span-wise coordinate [m]

Greek letters

$\bar{\cdot}$	ensamble average (weighted)

α	injection angle
β_i	angle between the normal unit vector and a ray leaving the surface dA_i
β_η	extinction coefficient, $\sigma_{s\,\eta} + \kappa_\eta$ [m^{-1}]
δ_{ij}	Kronecker's delta function
$D_{e^{-2}}$	diameter of a Gaussian laser beam
$d_{e^{-2}}$	diameter of a focused Gaussian laser beam at the focal point
δx	spacing between injection holes in the stream-wise direction [m]
δy	spacing between injection holes in the span-wise direction [m]
Δ	local rate of expansion (dilatation) *or* difference
ε	dissipation of $\frac{1}{2}\overline{u_i u_i}$
ϵ	total diffuse hemispherical emissivity
ϵ_η	spectral directional emissivity at wavenumber η
η	wavenumber [m^{-1}]
η_w^{max}	film cooling effectiveness parameter based on maximum span-wise surface temperature
κ	specific heat ratio (c_p/c_v)
κ_η	absorption coefficient at wavenumber η [m^{-1}]
λ	thermal conductivity [W/(m· K)] *or* eigenvalue
μ	dynamic viscosity [Pa·s]
ν	frequency [Hz]
ν_T	turbulent viscosity
ω	fluctuating part of the vorticity
ω_η	single scattering albedo, $\sigma_{s\,\eta}/\beta_\eta$, at wavenumber η
Ω	solid angle [sr]
Ω_i	mean vorticity in the i-direction
Ω_{ij}	rotation tensor [1/s]
Φ	phase
ρ	density [$\mathrm{kg/m}^3$]
ρ^D	total diffuse hemispherical reflectivity
ρ''_η	spectral bidirectional reflection function
$\rho(\tau)$	autocorrelation coefficient
σ	Stefan-Boltzmann constant [$\mathrm{W/(m^2 \cdot K^4)}$]
$\sigma_{s\,\eta}$	scattering coefficient at wavenumber η [m^{-1}]
τ	time difference [s] or [ms]

τ_{ij}	viscous stress tensor [Pa]
τ_{η}	optical thickness at wavenumber η

Subscripts

$+,-$	either side of a boundary
0	the hot mainstream
$0l$	illuminating
1	a position on the test plate wall
amb	ambient room condition
$center$	center of the injection holes
c	cooling gas in the plenum chamber
E	east node
e	east face of the control volume
f	a face of the control volume
IR	infrared camera measurement with ϵ set to 1.00
jet	the state in the injection holes
li	scattered
N	north node
n	north face of the control volume
off	distance from x=0 to the leading edge of the first row of injection holes
P	a point P
ref	reference state in Sutherland's law, 273 K
S	shift
s	to the solid matrix of the test plate
T	top node
t	top face of the control volume
w	test plate wall

Superscripts

D	indicates diffuse
max	maximum in span-wise direction
$\star$	indicates a dimensionless variable

Part III

Appendices

Appendix A

Calculation of the view factors

The view factor between rectangle elements appears in the correction of the measured wall temperature. In the actual correction calculation, the formula for perpendicular rectangles was simplified using Mathematica® and was exported to FORTRAN 77. The view factor for parallel rectangles was approximated as described in section 3.3 on page 18.

A.1 Rectangle to rectangle in perpendicular planes

The formulas are given in Howell (1982), and the geometry is shown in figure A.1 on the following page.

$$\begin{aligned} \alpha_{li} &= (\xi_l^2 + x_i^2)^{1/2} \\ \beta_{jk} &= y_j - \eta_k \end{aligned} \tag{A.1}$$

$$F_{ij} = \frac{1}{(x_2 - x_1)(y_2 - y_1)} \sum_{l=1}^{2} \sum_{k=1}^{2} \sum_{j=1}^{2} \sum_{i=1}^{2} \Big[(-1)^{i+j+k+l} G(\alpha_{li}, \beta_{jk}) \Big] \tag{A.2}$$

$$\begin{aligned} G(\alpha_{li}, \beta_{jk}) = \frac{1}{2\pi} \Big\{ & \alpha_{li} \beta_{jk} \arctan \frac{\beta_{jk}}{\alpha_{li}} - \\ & - \frac{1}{2} (\alpha_{li}^2 - \beta_{jk}^2) \ln (\alpha_{li}^2 + \beta_{jk}^2)^{1/2} + \\ & + \frac{1}{4} \beta_{jk}^2 \big[1 - 4 \ln \beta_{jk} \big] + \frac{1}{2} \alpha_{li}^2 \ln \alpha_{li} \Big\} \end{aligned} \tag{A.3}$$

A.2 Rectangle to rectangle in parallel planes

The formulas are given in Howell (1982) and the geometry is shown in figure A.2 on the next page.

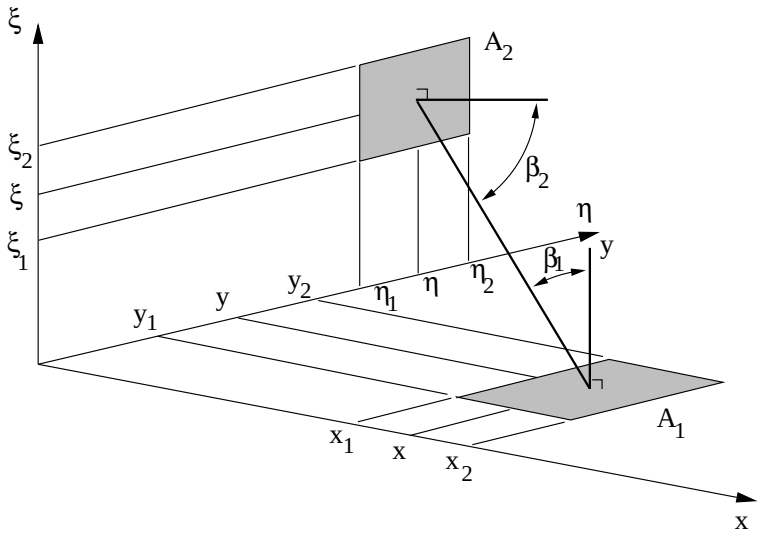

Figure A.1: Radiative exchange between two parallel rectangular surfaces.

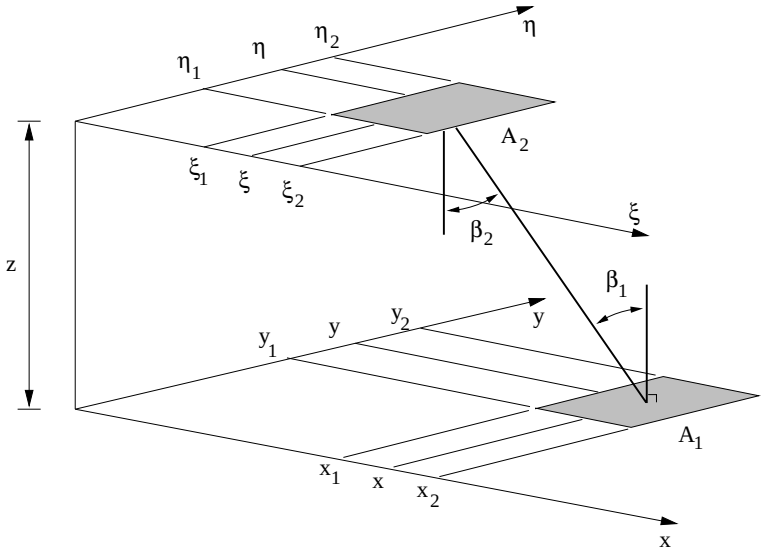

Figure A.2: Radiative exchange between two perpendicular rectangular surfaces.

$$\begin{aligned} X &= x/z \\ Y &= y/z \\ N &= \eta/z \\ S &= \xi/z \end{aligned} \tag{A.4}$$

$$\begin{aligned} \alpha_{li} &= S_l - X_i \\ \beta_{jk} &= N_k - Y_j \end{aligned} \tag{A.5}$$

$$F_{ij} = \frac{1}{(X_2 - X_1)(Y_2 - Y_1)} \sum_{l=1}^{2} \sum_{k=1}^{2} \sum_{j=1}^{2} \sum_{i=1}^{2} \left[(-1)^{i+j+k+l} G(\alpha_{li}, \beta_{jk}) \right] \tag{A.6}$$

$$\begin{aligned} G(\alpha_{li}, \beta_{jk}) = \frac{1}{2\pi} \Big\{ & \alpha_{li} (1 + \beta_{jk}^2)^{1/2} \arctan \frac{\alpha_{li}}{(1 + \beta_{jk}^2)^{1/2}} - \\ & - \beta_{jk} \arctan \beta_{jk} + \beta_{jk} (1 + \alpha_{li}^2)^{1/2} \arctan \frac{\beta_{jk}}{(1 + \alpha_{li}^2)^{1/2}} - \\ & - \alpha_{li}^2 \ln \alpha_{li} + \frac{1}{2} \ln(1 + \beta_{jk}^2) - \frac{1}{2} \ln[1 + \alpha_{li}^2 + \beta_{jk}^2] \Big\} \end{aligned} \tag{A.7}$$

Appendix B

Derivation of wall temperature correction equations

B.1 Wall temperature correction algorithm

In these derivations, the walls are considered gray and diffuse. The leaving heat flux, J_1, from an area element, A_1, on the test plate is the sum of emitted heat flux, $\epsilon_1 E_1$, and reflected irradiated heat flux, $\rho_1^D H_1$. J_1 is measured by the infrared camera with the emissivity set to 1.00.

$$J_1 = \epsilon_1 E_1 + \rho_1^D H_1$$

where

$$H_1 = \frac{1}{A_1} \sum_i F_{i1} A_i J_i = \frac{1}{A_1} \sum_i F_{i1} A_i \left(\epsilon_i E_i + \rho_i^D H_i \right)$$

$$\Rightarrow J_1 = \epsilon_1 E_1 + \frac{\rho_1^D}{A_1} \sum_i F_{i1} A_i \left(\epsilon_i E_i + \rho_i^D H_i \right)$$

where

$$H_i = \frac{1}{A_i} \sum_j F_{ij} A_j J_j$$

Product $\rho_1^D \rho_i^D$ is small ($\sim 0.02^2$), and thus the contribution of H_i is neglected.

$$\Rightarrow J_1 \approx \epsilon_1 E_1 + \frac{\rho_1^D}{A_1} \sum_i F_{i1} A_i \epsilon_i E_i$$

The blackbody emission is sought.

$$E_1 \approx \frac{J_1}{\epsilon_1} - \frac{\rho_1^D}{\epsilon_1 A_1} \sum_i F_{i1} A_i \epsilon_i E_i$$

Stefan-Boltzmann's law gives the heat flux at a given temperature. It is assumed that $\epsilon_1 = \epsilon_i = \epsilon$.

$$\sigma T_1^4 \approx \frac{\sigma T_{IR}^4}{\epsilon_1} - \frac{\rho_1^D}{A_1} \sum_i F_{i1} A_i \sigma T_i^4 \tag{B.1}$$

which is rewritten as

$$T_1 \approx \left(\frac{T_{IR}^4}{\epsilon_1} - \frac{\rho_1^D}{A_1} \sum_i F_{i1} A_i T_i^4 \right)^{1/4}$$

B.2 Error estimate algorithm

In eq. B.1, the following replacements are made $T_1 \rightarrow T_1 + \Delta T_1$, $T_{IR} \rightarrow T_{IR} + \Delta T_{IR}$, $T_i \rightarrow T_i + \Delta T_i$, $\epsilon \rightarrow \epsilon + \Delta\epsilon$, $\rho \rightarrow \rho + \Delta\rho$.

$$(T_1 + \Delta T_1)^4 \approx \frac{(T_{IR} + \Delta T_{IR})^4}{(\epsilon + \Delta\epsilon)} - \frac{\left(\rho_1^D + \Delta\rho^D\right)}{A_1} \sum_i F_{i1} A_i \left(T_i + \Delta T_i\right)^4$$

All quadratic and higher order terms are neglected, assuming that $\Delta T_1/T_1$, $\Delta T_{IR}/T_{IR}$ and $\Delta T_i/T_i$ are small compared to unity.

$$\begin{aligned} \left(T_1^4 + 4\Delta T_1 T_1^3\right) \approx & \frac{\left(T_{IR}^4 + 4\Delta T_{IR} T_{IR}^3\right)}{(\epsilon + \Delta\epsilon)} - \\ & - \frac{\left(\rho_1^D + \Delta\rho^D\right)}{A_1} \sum_i F_{i1} A_i \left(T_i^4 + 4\Delta T_i T_i^3\right) \end{aligned}$$

Subtraction of eq. B.1 and rearrangement yields

$$\begin{aligned} 4T_1^3 \left(\epsilon + \Delta\epsilon\right) \Delta T_1 \approx & \; 4T_{IR}^3 \Delta T_{IR} - \\ & - \frac{\rho^D \epsilon}{A_1} \sum_i F_{i1} A_i 4\Delta T_i T_i^3 - \\ & - \frac{\epsilon\Delta\rho^D + \rho^D\Delta\epsilon + \Delta\rho^D\Delta\epsilon}{A_1} \sum_i F_{i1} A_i \left(T_i^4 + 4\Delta T_i T_i^3\right) \end{aligned}$$

Finally, we get, if $\Delta\rho^D\Delta\epsilon$ is neglected,

$$\begin{aligned} |\Delta T_1| &\approx \left| \frac{T_{IR}^3 \Delta T_{IR}}{T_1^3 (\epsilon + \Delta\epsilon)} \right| + \\ &+ \left| \frac{\rho^D \epsilon}{T_1^3 (\epsilon + \Delta\epsilon) A_1} \sum_i F_{i1} A_i \Delta T_i T_i^3 \right| + \\ &+ \left| \frac{\epsilon \Delta\rho^D + \rho^D \Delta\epsilon}{4 T_1^3 (\epsilon + \Delta\epsilon) A_1} \sum_i F_{i1} A_i \left(T_i^4 + 4 \Delta T_i T_i^3 \right) \right| \end{aligned} \tag{B.2}$$

Appendix C

Derivation of dimensionless parameters

C.1 Governing equations

Continuity equation:

$$\frac{\partial \rho}{\partial t} + \frac{\partial}{\partial x_j}\left(\rho u_j\right) = 0 \tag{C.1}$$

Navier-Stokes equation:

$$\frac{\partial}{\partial t}\left(\rho u_i\right) + \frac{\partial}{\partial x_j}\left(\rho u_i u_j + p\delta_{ij} - \tau_{ij}\right) - \rho g_i = 0 \tag{C.2}$$

Energy equation for the fluid:

$$\begin{aligned}&\frac{\partial}{\partial t}\left(\rho\left(c_v T + \tfrac{1}{2}u_k u_k\right)\right) + \\ &+\frac{\partial}{\partial x_j}\left(\rho u_j\left(c_v T + \tfrac{1}{2}u_k u_k\right) + u_j p + q_j - u_i \tau_{ij}\right) = 0\end{aligned} \tag{C.3}$$

Energy equation for the solid:

$$\rho_s \frac{\partial c_{p_s} T}{\partial t} - \frac{\partial}{\partial x_i}\left(\lambda_s \frac{\partial T}{\partial x_i}\right) = 0 \tag{C.4}$$

C.2 Additional equations

The viscous stress tensor is given by:

$$\tau_{ij} = 2\mu\left(e_{ij} - \frac{1}{3}\Delta\delta_{ij}\right) \tag{C.5}$$

where δ_{ij} is Kronecker's delta function and the rate of strain tensor, e_{ij}, is given by:

$$e_{ij} = \frac{1}{2}\left(\frac{\partial u_i}{\partial x_j} + \frac{\partial u_j}{\partial x_i}\right) \tag{C.6}$$

The dilatation is given by:

$$\Delta = \frac{\partial u_k}{\partial x_k} \tag{C.7}$$

The heat flux vector is given by:

$$q_j = -\lambda \frac{\partial T}{\partial x_j} \tag{C.8}$$

The equation of state is given by:

$$p = \rho R T \tag{C.9}$$

The temperature dependence of the viscosity and thermal conductivity of air is fairly well described by Sutherland's law:

$$\mu \approx \mu_{ref}\left(\frac{T}{T_{ref}}\right)^{3/2}\left(\frac{T_{ref} + S_\mu}{T + S_\mu}\right) \tag{C.10}$$

$$\lambda \approx \lambda_{ref}\left(\frac{T}{T_{ref}}\right)^{3/2}\left(\frac{T_{ref} + S_\lambda}{T + S_\lambda}\right) \tag{C.11}$$

$$c_v = c_p - R \tag{C.12}$$

A linear dependence is assumed in the specific heat.

$$c_p \approx c_{p_c} + \left(\frac{\partial c_p}{\partial T}\right)_c T \tag{C.13}$$

$$c_{p_s} \approx c_{p_{s,ref}} + \left(\frac{\partial c_{p_s}}{\partial T}\right)_{ref} T \tag{C.14}$$

$$\rho_s \approx \text{constant, as the volumetric expansion of the solid is small} \tag{C.15}$$

$$\lambda_s \approx \lambda_{s,ref} + \left(\frac{\partial \lambda_s}{\partial T}\right)_{ref} T \tag{C.16}$$

C.3 Boundary conditions

The boundary conditions at the side walls in the plenum chamber are given by (see figure C.1 on page 127):

$$\left.\begin{array}{r} x = 0 \text{ and } x = L \\ 0 < y < H_2 \\ 0 < z < B \end{array}\right\} \Rightarrow \left\{\begin{array}{l} u_i = 0 \\ T = T_c \\ \rho = \rho_c \end{array}\right.$$

The boundary conditions at the inlet in the mainstream duct are given by:

$$\left.\begin{array}{r} x = 0 \\ H_2 + b < y < H_1 + H_2 + b \\ 0 < z < B \end{array}\right\} \Rightarrow \left\{\begin{array}{l} u = U_0 \\ v = w = 0 \\ T = T_0 \\ \rho = \rho_0 \end{array}\right.$$

The boundary conditions at the outlet in the mainstream duct are given by:

$$\left.\begin{array}{r} x = L \\ H_2 + b < y < H_1 + H_2 + b \\ 0 < z < B \end{array}\right\} \Rightarrow \left\{\begin{array}{l} \frac{\mathrm{D}u_i}{\mathrm{D}t} = 0 \\ \\ \frac{\mathrm{D}T}{\mathrm{D}t} = 0 \end{array}\right.$$

The boundary conditions at the side walls in the mainstream duct are given by:

$$\left.\begin{array}{r} 0 < x < L \\ 0 < y < H_1 + H_2 + b \\ z = 0 \text{ and } z = B \end{array}\right\} \Rightarrow \left\{\begin{array}{l} u_i = 0 \\ \frac{\partial T}{\partial z} = 0 \end{array}\right.$$

The boundary condition at the inlet of the plenum chamber is given by:

$$\left.\begin{array}{r} 0 < x < L \\ y = 0 \\ 0 < z < B \end{array}\right\} \Rightarrow \left\{\begin{array}{l} v = U_c \\ u = w = 0 \\ T = T_c \\ \rho = \rho_c \end{array}\right.$$

The boundary conditions at the top wall of the mainstream duct are given by:

$$\left.\begin{array}{r} 0 < x < L \\ y = H_1 + H_2 + b \\ 0 < z < B \end{array}\right\} \Rightarrow \left\{\begin{array}{l} u_i = 0 \\ \frac{\partial T}{\partial y} = 0 \end{array}\right.$$

The boundary conditions at the top and bottom side of the test plate, except where the injection holes are located, are given by:

$$\left.\begin{array}{r} 0 < x < L \\ y = H_2 \text{ and } y = H_2 + b \\ (x - x_{center})^2 \sin^2(\alpha) + (z - z_{center})^2 \not< \frac{d^2}{4} \\ \left\{\begin{array}{l} x_{center} = (n-1)\delta x + d/(2\sin\alpha) \\ \quad + x_{off} + (y - b - H_1)\cot(\alpha) \\ z_{center} = (m-1)\delta z + d/2 \\ \quad + (1 - (-1)^n)\delta z/4 - z_{off} \\ n = 1, 2, 3, \ldots, \text{number of rows} \\ m = 1, 2, 3, 4 \end{array}\right. \\ 0 < z < B \end{array}\right\} \Rightarrow \left\{\begin{array}{l} u_i = 0 \\ \\ T_+ = T_- \\ \\ \left(\lambda \frac{\partial T}{\partial y}\right)_+ = \\ = \left(\lambda \frac{\partial T}{\partial y}\right)_- \end{array}\right.$$

where x_{off} is the distance from $x = 0$ to the leading edge of the first row of holes. In the same way, z_{off} is the distance from $z = 0$ to the edge of the hole. The boundary conditions at the injection hole walls are given by:

$$\left.\begin{array}{r} 0 < x < L \\ y = H_2 \text{ and } y = H_2 + b \\ (x - x_{center})^2 \sin^2(\alpha) + (z - z_{center})^2 = \frac{d^2}{4} \\ \left\{\begin{array}{l} x_{center} = (n-1)\delta x + d/(2\sin\alpha) + \\ \quad + x_{off} + (y - b - H_1)\cot(\alpha) \\ z_{center} = (m-1)\delta z + d/2 \\ \quad + (1 - (-1)^n)\delta z/4 - z_{off} \\ n = 1, 2, 3, \ldots, \text{number of rows} \\ m = 1,\ 2,\ 3,\ 4 \end{array}\right. \\ 0 < z < B \end{array}\right\} \Rightarrow \left\{\begin{array}{l} u_i = 0 \\ \\ T_+ = T_- \\ \\ \vec{n}_+ \cdot (\lambda \nabla T)_+ = \\ = \vec{n}_- \cdot (\lambda \nabla T)_- \end{array}\right.$$

C.4 Equations in dimensionless form

The primary scaling variables are U_c, d, T_c and ρ_c. Point c refers to a point at the inlet of the cooling air.

C.4.1 Dimensionless variables

$$\begin{array}{ccc} x_i = x_i^\star d & t = t^\star d/U_c & u_i = u_i^\star U_c \\ p = p^\star \rho_c U_c^2 & T = T^\star T_c & \rho = \rho^\star \rho_c \\ \mu = \mu^\star \rho_c U_c d & \lambda = \lambda^\star \frac{\rho_c U_c^3 d}{T_c} & c_p = c_p^\star \frac{U_c^2}{T_c} \end{array}$$

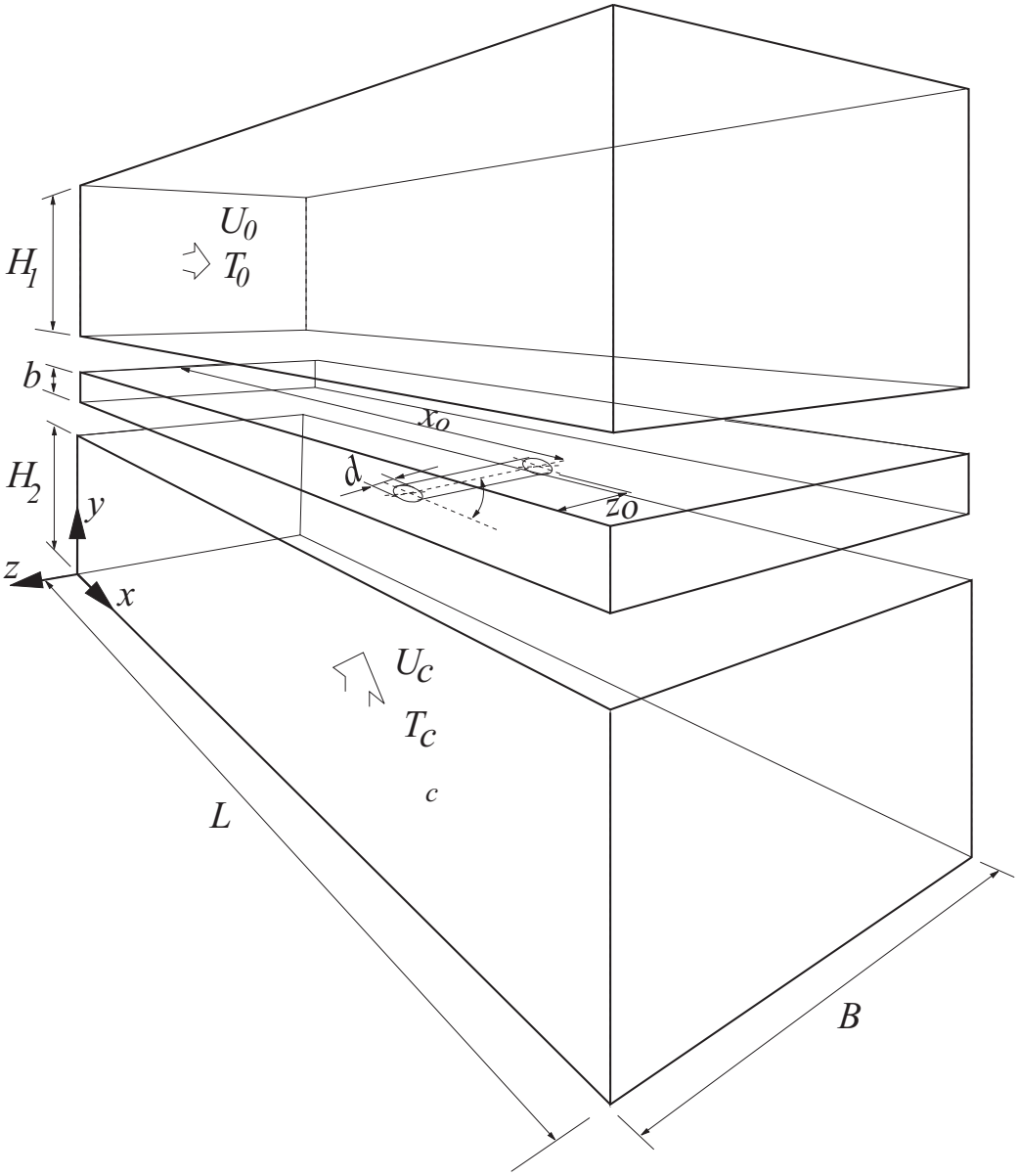

Figure C.1: Domain in the dimensional analysis. The lower block is the plenum chamber, the middle is the test plate and the uppermost is the mainstream duct.

C.5 Governing equations in dimensionless form

Continuity equation:

$$\frac{\partial \rho^\star}{\partial t^\star} + \frac{\partial}{\partial x_j^\star}\left(\rho^\star u_j^\star\right) = 0 \tag{C.17}$$

Navier-Stokes equation:

$$\frac{\partial}{\partial t^\star}\left(\rho^\star u_i^\star\right) + \frac{\partial}{\partial x_j^\star}\left(\rho^\star u_i^\star u_j^\star + p^\star \delta_{ij} - \tau_{ij}^\star\right) - \rho^\star g_i^\star = 0 \tag{C.18}$$

Energy equation for the fluid:

$$\begin{aligned}&\frac{\partial}{\partial t^\star}\left(\rho^\star\left(c_v^\star T^\star + \tfrac{1}{2}u_k^\star u_k^\star\right)\right) + \\ &+\frac{\partial}{\partial x_j^\star}\left(\rho^\star u_j^\star\left(c_v^\star T^\star + \tfrac{1}{2}u_k^\star u_k^\star\right) + u_j^\star p^\star + q_j^\star - u_i^\star \tau_{ij}^\star\right) = 0\end{aligned} \tag{C.19}$$

Energy equation for the solid:

$$\rho_s^\star \frac{\partial c_{p_s}^\star T^\star}{\partial t^\star} - \frac{\partial}{\partial x_i^\star}\left(\lambda_s^\star \frac{\partial T^\star}{\partial x_i^\star}\right) = 0 \tag{C.20}$$

C.6 Additional equations in dimensionless form

$$\tau_{ij}^\star = 2\mu^\star\left(e_{ij}^\star - \frac{1}{3}\Delta^\star \delta_{ij}\right) \tag{C.21}$$

$$e_{ij}^\star = \frac{1}{2}\left(\frac{\partial u_i^\star}{\partial x_j^\star} + \frac{\partial u_j^\star}{\partial x_i^\star}\right) \tag{C.22}$$

$$\Delta^\star = \frac{\partial u_k^\star}{\partial x_k^\star} \tag{C.23}$$

$$q_j^\star = -\lambda^\star \frac{\partial T^\star}{\partial x_j^\star} \tag{C.24}$$

$$p^\star = \rho^\star R^\star T^\star = \frac{RT_c}{U_c^2}\rho^\star T^\star \tag{C.25}$$

$$\begin{aligned}
\mu^\star &= \frac{\mu}{\rho_c U_c d} \approx \\
&\approx \frac{\mu_{ref}}{\rho_c U_c d}\left(\frac{T_c}{T_{ref}}\right)^{3/2} T^{\star 3/2}\left(\frac{T_{ref}/T_c + S_\mu/T_c}{T^\star + S_\mu/T_c}\right) = \\
&= \frac{\mu_c}{\rho_c U_c d} T^{\star 3/2}\left(\frac{1 + S_\mu/T_c}{T^\star + S_\mu/T_c}\right) \qquad \text{(C.26)}
\end{aligned}$$

$$\begin{aligned}
\lambda^\star &= \frac{\lambda T_c}{\rho_c U_c^3 d} \approx \\
&\approx \frac{\lambda_{ref} T_c}{\rho_c U_c^3 d}\left(\frac{T_c}{T_{ref}}\right)^{3/2} T^{\star 3/2}\left(\frac{T_{ref}/T_c + S_\lambda/T_c}{T^\star + S_\lambda/T_c}\right) = \\
&= \frac{\lambda_c T_c}{\rho_c U_c^3 d} T^{\star 3/2}\left(\frac{1 + S_\lambda/T_c}{T^\star + S_\lambda/T_c}\right) \qquad \text{(C.27)}
\end{aligned}$$

$$g_i^\star = \frac{g_i d}{U_c^2} = \frac{1}{Fr_c}\frac{g_i}{|g_i|} \qquad \text{(C.28)}$$

where Fr_c is the Froude number. In these experiments, the buoyancy effect is neglected, as $u_j \frac{\partial u_i}{\partial x_j} \sim U_0^2/d \gg g$ on a local basis and $u_j \frac{\partial u_i}{\partial x_j} \sim U_0^2/L \gg g$, ($17^2 \gg 9.81$) on a more global basis.

$$c_v^\star = c_p^\star - \frac{R T_c}{U_c^2} = c_p^\star - R^\star \qquad \text{(C.29)}$$

$$c_p^\star \approx \frac{T_c c_{p_c}}{U_c^2}\left(1 + \left(\frac{\partial c_p}{\partial T}\right)_c \frac{T_c}{c_{p_c}} T^\star\right) \qquad \text{(C.30)}$$

$$c_{p_s}^\star \approx \frac{T_c c_{p_{s,ref}}}{U_c^2}\left(1 + \left(\frac{\partial c_{p_s}}{\partial T}\right)_{ref} \frac{T_c}{c_{p_{s,ref}}} T^\star\right) \qquad \text{(C.31)}$$

$$\rho_s^\star = \rho_s/\rho_c \qquad \text{(C.32)}$$

$$\lambda_s^\star \approx \frac{T_c \lambda_{s,ref}}{\rho_c U_c^3 d}\left(1 + \left(\frac{\partial \lambda_s}{\partial T}\right)_{ref} \frac{T_c}{\lambda_{s,ref}} T^\star\right) \qquad \text{(C.33)}$$

C.7 Boundary conditions in dimensionless form

$$\left.\begin{array}{r} x^\star = 0 \text{ and } x^\star = L/d \\ 0 < y^\star < H_2/d \\ 0 < z^\star < B/d \end{array}\right\} \Rightarrow \left\{\begin{array}{l} u_i^\star = 0 \\ T^\star = 1 \\ \rho^\star = 1 \end{array}\right.$$

$$\left.\begin{array}{r} x^\star = 0 \\ H_2/d + B/d < y^\star < H_1/d + H_2/d + b/d \\ 0 < z^\star < B/d \end{array}\right\} \Rightarrow \left\{\begin{array}{l} u^\star = U_0/U_c \\ v^\star = w^\star = 0 \\ T^\star = T_0/T_c \\ \rho^\star = \rho_0/\rho_c \end{array}\right.$$

$$\left.\begin{array}{r} x^\star = L/d \\ H_2/d + b/d < y^\star < H_1/d + H_2/d + b/d \\ 0 < z^\star < B/d \end{array}\right\} \Rightarrow \left\{\begin{array}{l} \frac{\mathrm{D}u_i^\star}{\mathrm{D}t^\star} = 0 \\ \\ \frac{\mathrm{D}T^\star}{\mathrm{D}t^\star} = 0 \end{array}\right.$$

$$\left.\begin{array}{r} 0 < x^\star < L/d \\ 0 < y^\star < H_1/d + H_2/d + b/d \\ z^\star = 0 \text{ and } z^\star = B/d \end{array}\right\} \Rightarrow \left\{\begin{array}{l} u_i^\star = 0 \\ \\ \frac{\partial T^\star}{\partial z^\star} = 0 \end{array}\right.$$

$$\left.\begin{array}{r} 0 < x^\star < L/d \\ y^\star = 0 \\ 0 < z^\star < B/d \end{array}\right\} \Rightarrow \left\{\begin{array}{l} v^\star = 1 \\ u^\star = w^\star = 0 \\ T^\star = 1 \\ \rho^\star = 1 \end{array}\right.$$

$$\left.\begin{array}{r} 0 < x^\star < L/d \\ y^\star = H_1/d + H_2/d + b/d \\ 0 < z^\star < B/d \end{array}\right\} \Rightarrow \left\{\begin{array}{l} u_i^\star = 0 \\ \\ \frac{\partial T^\star}{\partial y^\star} = 0 \end{array}\right.$$

$$\left.\begin{array}{r} 0 < x^\star < L/d \\ y^\star = H_2/d \text{ and } y^\star = H_2/d + b/d \\ (x^\star - x^\star_{center})^2 \sin^2(\alpha) + (z^\star - z^\star_{center})^2 \not< \frac{1}{4} \\ \left\{\begin{array}{l} x^\star_{center} = (n-1)\delta x^\star + x^\star_{off} + 1/(2\sin\alpha) \\ \qquad +(y^\star - b/d - H_1/d)\cot(\alpha) \\ z^\star_{center} = (m-1)\delta z^\star + 1/2 \\ \qquad +(1-(-1)^n)\delta z^\star/4 + y^\star_{off} \\ n = 1, 2, 3, \ldots, \text{number of rows} \\ m = 1, 2, 3, 4 \end{array}\right. \\ 0 < z^\star < B/d \end{array}\right\} \Rightarrow \left\{\begin{array}{l} u_i^\star = 0 \\ \\ T^\star_+ = T^\star_- \\ \\ \left(\lambda^\star \frac{\partial T^\star}{\partial y^\star}\right)_+ = \\ = \left(\lambda^\star \frac{\partial T^\star}{\partial y^\star}\right)_- \end{array}\right.$$

where $x^\star_{off}$ is the dimensionless distance from $x^\star = 0$ to the leading edge of the first row of holes. In the same way, $z^\star_{off}$ is the dimensionless distance

from $z^\star = 0$ to the edge of the hole.

$$\left.\begin{array}{r} 0 < x^\star < L/d \\ y^\star = H_2/d \text{ and } y^\star = H_2/d + b/d \\ (x^\star - x^\star_{center})^2 \sin^2(\alpha) + (z^\star - z^\star_{center})^2 = \frac{1}{4} \\ \left\{\begin{array}{l} x^\star_{center} = (n-1)\delta x^\star + x^\star_{off} + 1/(2\sin\alpha) + \\ \quad +(y^\star - b/d - H_1/d)\cot(\alpha) \\ z^\star_{center} = (m-1)\delta z^\star + 1/2 \\ \quad +(1-(-1)^n)\delta z^\star/4 + y^\star_{off} \\ n = 1, 2, 3, \ldots, \text{number of rows} \\ m = 1, 2, 3, 4 \end{array}\right. \\ 0 < z^\star < B/d \end{array}\right\} \Rightarrow \left\{\begin{array}{l} u_i^\star = 0 \\ \\ T_+^\star = T_-^\star \\ \\ \vec{n}_+ \cdot (\lambda \nabla T)_+^\star = \\ = \vec{n}_- \cdot (\lambda \nabla T)_-^\star \end{array}\right.$$

C.8 Dimensionless groups

C.8.1 Primary groups

From eq. C.26 on page 129, we have

$$\frac{\mu_c}{\rho_c U_c d} = \frac{1}{Re_c} \tag{C.34}$$

from eq. C.27 on page 129

$$\frac{\lambda_c T_c}{\rho_c U_c^3 d} = \frac{1}{(\kappa - 1)\, Ma_c^2\, Re_c\, Pr_c} \tag{C.35}$$

and from eq. C.25 on page 128

$$\frac{RT_c}{U_c^2} = \frac{1}{\kappa\, Ma_c^2} \tag{C.36}$$

From eq. C.30 on page 129 and eq. C.33 on page 129, we have

$$\frac{T_c c_{p_c}}{U_c^2} = \frac{1}{(\kappa - 1)\, Ma_c^2} \tag{C.37}$$

$$\frac{T_c \lambda_{s,ref}}{\rho_c U_c^3 d} = \frac{1}{(\kappa - 1)\, Ma_c^2\, Re_c\, Pr_c} \frac{\lambda_{s,ref}}{\lambda_c} \tag{C.38}$$

From the dimensionless boundary conditions, we have

$$\frac{L}{d} \quad \frac{B}{d} \quad \frac{H_1}{d} \quad \frac{H_2}{d}$$

$$\frac{b}{d} \quad \frac{\delta x}{d} \quad \frac{\delta z}{d} \quad \frac{x_{off}}{d}$$

$$\frac{z_{off}}{d} \quad \alpha \quad \frac{U_0}{U_c} \quad \frac{T_0}{T_c}$$

$$\frac{\rho_0}{\rho_c}$$

C.8.2 Secondary groups

From Sutherland's law, eq. C.26 on page 129 and eq. C.27 on page 129, we have S_μ/T_c and S_λ/T_c. In the energy equation for the solid test plate, eq. C.32 on page 129, ρ_s/ρ_c appeared. The equations for the linear temperature dependence for c_p, c_{p_s} and λ_s eq. C.30 on page 129, eq. C.31 on page 129 and eq. C.33 on page 129 gave

$$\frac{T_c^2\left(\frac{\partial c_p}{\partial T}\right)_c}{U_c^2} \qquad \frac{T_c c_{p_{s,ref}}}{U_c^2}$$

$$\frac{T_c^2\left(\frac{\partial c_{p_s}}{\partial T}\right)_{ref}}{U_c^2} \qquad \frac{T_c^2\left(\frac{\partial \lambda_s}{\partial T}\right)_{ref}}{\rho_c U_c^3 d}$$

C.9 Radiative equation of transfer

C.9.1 Equations in dimensional form

If radiation is included in the analysis, an additional part, q_j^r, adds to the heat flux vector, q_j, in the energy equation for the fluid, eq. C.3 on page 123, and as a source term in the energy equation for the solid, eq. C.4 on page 123. The radiative heat flux can be written as (further details can be found in the book by Modest (1993))

$$q_i^r = \int_0^\infty \int_{4\pi} I_\eta(\widehat{\mathbf{s}}_i)\, \widehat{\mathbf{s}}_i \, d\Omega \, d\eta \tag{C.39}$$

where η is the wavenumber, Ω is the solid angle, $\widehat{\mathbf{s}}$ is a direction and $I_\eta(\widehat{\mathbf{s}})$ is the intensity in direction $\widehat{\mathbf{s}}$ at wavenumber η. The radiative transfer

equation, RTE, in direction $\widehat{\mathbf{s}}$ is

$$\widehat{\mathbf{s}} \cdot \nabla I_\eta(\widehat{\mathbf{s}}) = \overbrace{\kappa_\eta I_{b\eta}}^{\text{emission due to absorption}} + \overbrace{-\beta_\eta I_\eta(\widehat{\mathbf{s}})}^{\text{absorbtion and scattering away}} + \overbrace{\frac{\sigma_{s\eta}}{4\pi}\int_{4\pi} I_\eta(\widehat{\mathbf{s}}_i)\Phi_\eta(\widehat{\mathbf{s}}_i,\widehat{\mathbf{s}})\,d\Omega_i}^{\text{in-scattering}} \tag{C.40}$$

where $I_{b\eta}$ is the blackbody intensity, κ_η is the *absorption coefficient*, β_η is the *extinction coefficient*, $\sigma_{s\eta}$ is the *scattering coefficient* and $\Phi_\eta(\widehat{\mathbf{s}}_i,\widehat{\mathbf{s}})$ is the *scattering phase function*, all at wavenumber η. The equation above can be rewritten as

$$\frac{dI_\eta(\widehat{\mathbf{s}})}{d\tau_\eta} = (1-\omega_\eta)I_{b\eta} - I_\eta(\widehat{\mathbf{s}}) + \frac{\omega_\eta}{4\pi}\int_{4\pi} I_\eta(\widehat{\mathbf{s}}_i)\Phi_\eta(\widehat{\mathbf{s}}_i,\widehat{\mathbf{s}})\,d\Omega_i \tag{C.41}$$

where τ_η is the optical coordinate

$$\tau_\eta = \int_0^s (\kappa_\eta + \sigma_{s\eta})\,ds = \int_0^s \beta_\eta\,ds \tag{C.42}$$

and ω_η is the *single scattering albedo*

$$\omega_\eta = \frac{\sigma_{s\eta}}{\kappa_\eta + \sigma_{s\eta}} \tag{C.43}$$

The boundary condition for the RTE at a position $\mathbf{r_w}$ at the wall is

$$I_\eta(\mathbf{r_w},\widehat{\mathbf{s}}) = \epsilon'_\eta(\mathbf{r_w},\widehat{\mathbf{s}})I_{b\eta}(\mathbf{r_w}) + \int_{\widehat{\mathbf{n}}\cdot\widehat{\mathbf{s}}<0} \rho''_\eta(\mathbf{r_w},\widehat{\mathbf{s}}',\widehat{\mathbf{s}})I_\eta(\mathbf{r_w},\widehat{\mathbf{s}}')|\widehat{\mathbf{n}}\cdot\widehat{\mathbf{s}}'|\,d\Omega' \tag{C.44}$$

where $\widehat{\mathbf{n}}$ is the normal unit vector at the wall. Furthermore, $\epsilon'_\eta(\mathbf{r_w},\widehat{\mathbf{s}})$ is the *spectral directional emissivity* of the wall and $\rho''_\eta(\mathbf{r_w},\widehat{\mathbf{s}}',\widehat{\mathbf{s}})$ is the *spectral bidirectional reflection function* at the wall.

C.9.2 Equations in dimensionless form

The equations above can be written in a dimensionless form in the same way as for the continuity, momentum and energy equations. Intensity I_η

is a field variable, just like ρ, u_i and T, but the blackbody intensity, $I_{b\eta}$, is not. The blackbody intensity is a function of the field variables T and η. The extinction coefficient, β_η, has the dimension of reciprocal length, but the parameters ϵ'_η, ρ''_η, ω_η and Φ_η [m^2/m^2] are already dimensionless.

$$q_i^{\star r} = \int_0^\infty \int_{4\pi} I_\eta^\star(\widehat{\mathbf{s}}_i)\, \widehat{\mathbf{s}}_i \, d\Omega^\star \, d\eta^\star \tag{C.45}$$

where $\eta^\star = \eta d$, $\Omega^\star = \Omega$ and $I_\eta(\widehat{\mathbf{s}})^\star = I_\eta(\widehat{\mathbf{s}})/(\rho_c U_c^3 d)$. The dimensionless radiative transfer equation, RTE*, in direction $\widehat{\mathbf{s}}$ is

$$\widehat{\mathbf{s}} \cdot \nabla^\star I_\eta^\star(\widehat{\mathbf{s}}) = \kappa_\eta^\star I_{b\eta}^\star - \beta_\eta^\star I_\eta^\star(\widehat{\mathbf{s}}) + \frac{\sigma_{s\eta}^\star}{4\pi} \int_{4\pi} I_\eta^\star(\widehat{\mathbf{s}}_i) \Phi_\eta^\star(\widehat{\mathbf{s}}_i, \widehat{\mathbf{s}})\, d\Omega_i^\star \tag{C.46}$$

and the accompanying boundary condition

$$I_\eta^\star(\mathbf{r_w}, \widehat{\mathbf{s}}) = \epsilon_\eta^{'\star}(\mathbf{r_w}, \widehat{\mathbf{s}}) I_{b\eta}^\star(\mathbf{r_w}) + \int_{\widehat{\mathbf{n}}\cdot\widehat{\mathbf{s}}<0} \rho_\eta^{''\star}(\mathbf{r_w}, \widehat{\mathbf{s}}', \widehat{\mathbf{s}}) I_\eta^\star(\mathbf{r_w}, \widehat{\mathbf{s}}') |\widehat{\mathbf{n}} \cdot \widehat{\mathbf{s}}'| \, d\Omega^{'\star} \tag{C.47}$$

The dimensional blackbody intensity can then be written as

$$I_{b\eta} = \frac{2hc^2\eta^3}{e^{\left(\frac{hc\eta}{kT}\right)} - 1} \tag{C.48}$$

where c [m/s] is the speed of light in vacuum, h [Js] is the Planck constant and k [J/K] is the Boltzmann constant. The dimensionless blackbody intensity can be written as

$$I_{b\eta}^\star = \frac{2hc^2}{\rho_c U_c^3 d^4} \frac{\eta^{\star 3}}{e^{\left(\frac{hc}{kT_c d}\frac{\eta^\star}{T^\star}\right)} - 1} \tag{C.49}$$

Thus we have derived seven new dimensionless parameters to consider if radiative heat transfer is taken in account.

1. The spectral directional emissivity of the wall, $\epsilon_\eta^{'\star}(\mathbf{r_w}, \widehat{\mathbf{s}}) = \epsilon'_\eta(\mathbf{r_w}, \widehat{\mathbf{s}})$.
2. The spectral bidirectional reflection function, $\rho_\eta^{''\star}(\mathbf{r_w}, \widehat{\mathbf{s}}', \widehat{\mathbf{s}}) = \rho_\eta^{''}(\mathbf{r_w}, \widehat{\mathbf{s}}', \widehat{\mathbf{s}})$.
3. The product of the extinction coefficient and the length scale, $\beta_\eta^\star = \beta_\eta d$.
4. The single scattering albedo, ω_η.

5. The scattering phase function $\Phi_\eta^\star(\widehat{\mathbf{s}}_i, \widehat{\mathbf{s}}) = \Phi_\eta(\widehat{\mathbf{s}}_i, \widehat{\mathbf{s}})$.

6. The group $hc^2/(\rho_c \cdot U_c^3 \cdot d^4)$. (Note that $2\pi hc^2$=3.74·10^{-6} Wm^2 is the first Planck function constant.)

7. The group $hc/(k \cdot T_c \cdot d)$. (Note that hc/k=14.388 μmK is the second Planck function constant.)

The radiative heat transfer is not considered in these experiments but may be important in a real combustion chamber case.

Appendix D

Integration of the pressure gradients

The mean pressure gradients were computed by balancing the Reynolds momentum equations:

$$\begin{cases} \frac{1}{\rho}\frac{\partial \overline{P}}{\partial x} = -\overline{U}_i\frac{\partial \overline{U}}{\partial x_i} - \frac{\partial \overline{u_i u}}{\partial x_i} + \nu\frac{\partial^2 \overline{U}}{\partial x_i^2} \\ \frac{1}{\rho}\frac{\partial \overline{P}}{\partial y} = -\overline{U}_i\frac{\partial \overline{V}}{\partial x_i} - \frac{\partial \overline{u_i v}}{\partial x_i} + \nu\frac{\partial^2 \overline{V}}{\partial x_i^2} \\ \frac{1}{\rho}\frac{\partial \overline{P}}{\partial z} = -\overline{U}_i\frac{\partial \overline{W}}{\partial x_i} - \frac{\partial \overline{u_i w}}{\partial x_i} + \nu\frac{\partial^2 \overline{W}}{\partial x_i^2} \end{cases} \tag{D.1}$$

In equation system D.1, all terms on the right and side were computed from the measurements at each point in the Cartesian grid. In this way, the pressure gradients at each point were calculated. It was then possible to integrate the gradients to get the pressure itself. It is not certain that integrating along different paths will give the same result because the measured gradients are tainted with errors. The integration was done by minimizing, in a least-squares sense, the difference between the measured pressure gradients and the pressure gradients from the computed pressure field. This results in solving a linear equation system that is overdetermined as it is possible to integrate from a single point to an other point along many paths. Solving the equation system in the least-squares meaning involves an averaging process (an integration) that gives a much smoother pressure field than the pressure gradient field.

The gradients on the right hand side of equation system D.1 were estimated by central differences. The measured pressure gradients, $\partial\overline{P}/\partial x_i$, were interpolated to the cell faces between two measurement points and

denoted $(\partial\overline{P}/\partial x_i)^f$. The gradient at the cell face was calculated by a second order difference approximation. The absolute level of the pressure, the integration constant, is undetermined and is set in one point to an arbitrary constant, $\overline{P}_{abitrary}$. The resulting equation system was

$$\begin{cases} \overline{P}_P = \overline{P}_{abitrary} \\ \dfrac{\overline{P}_E - \overline{P}_P}{\delta x_e} = \left(\dfrac{\partial\overline{P}}{\partial x}\right)_e^f \\ \vdots \quad\quad \vdots \\ \dfrac{\overline{P}_N - \overline{P}_P}{\delta y_n} = \left(\dfrac{\partial\overline{P}}{\partial y}\right)_n^f \\ \vdots \quad\quad \vdots \\ \dfrac{\overline{P}_T - \overline{P}_P}{\delta z_t} = \left(\dfrac{\partial\overline{P}}{\partial z}\right)_t^f \\ \vdots \quad\quad \vdots \end{cases} \tag{D.2}$$

rewriting this gives

$$\underbrace{\begin{bmatrix} 1 & 0 & \cdots & & & & & \cdots & 0 \\ -1 & 1 & 0 & \cdots & & & & \cdots & 0 \\ 0 & -1 & 1 & 0 & \cdots & & & \cdots & 0 \\ \vdots & & & & & & & & \vdots \\ -1 & 0 & \cdots & 0 & 1 & 0 & \cdots & \cdots & 0 \\ \vdots & & & & & & & & \vdots \\ -1 & 0 & \cdots & & \cdots & 0 & 1 & 0 \cdots & 0 \\ \vdots & & & & & & & & \vdots \end{bmatrix}}_{\substack{\mathbf{S} \\ (m \times n)}} \underbrace{\begin{bmatrix} \overline{P}_1 \\ \overline{P}_2 \\ \vdots \\ \overline{P}_n \end{bmatrix}}_{\substack{\overline{\mathbf{P}} \\ (n \times 1)}} = \underbrace{\begin{bmatrix} \overline{P}_{abitrary} \\ \delta x_1 \cdot (\frac{\partial\overline{P}}{\partial x})_1^f \\ \delta x_2 \cdot (\frac{\partial\overline{P}}{\partial x})_2^f \\ \vdots \\ \delta y_1 \cdot (\frac{\partial\overline{P}}{\partial y})_1^f \\ \delta y_2 \cdot (\frac{\partial\overline{P}}{\partial y})_2^f \\ \vdots \\ \delta z_1 \cdot (\frac{\partial\overline{P}}{\partial z})_1^f \\ \delta z_2 \cdot (\frac{\partial\overline{P}}{\partial z})_2^f \end{bmatrix}}_{\substack{\mathbf{b} \\ (m \times 1)}} \tag{D.3}$$

where $n = n_x n_y n_z$ =35340 and $m = 3n_x n_y n_z$-$n_x n_y$-$n_x n_z$-$n_y n_z$+1 =102494. The pressure in each point was calculated as

$$\overline{\mathbf{P}} = (\mathbf{S}^t\mathbf{S})^{-1}\mathbf{S}^t\mathbf{b} \tag{D.4}$$

The moment matrix $\mathbf{S}^t\mathbf{S}$ is a penta-diagonal sparse matrix and direct inversion of it is very expensive. Equation D.5 was instead solved using the

conjugate gradients squared method, `cgs`, in Matlab.

$$\mathbf{A}\overline{\mathbf{P}} = \mathbf{B} \quad \text{where} \quad \mathbf{A} = \mathbf{S}^t\mathbf{S} \quad \text{and} \quad \mathbf{B} = \mathbf{S}^t\mathbf{b} \tag{D.5}$$

Convergence was reached within a few hundred iterations to a relative residual, $|\mathbf{B} - \mathbf{A}\overline{\mathbf{P}}|/|\mathbf{B}|$, of 10^{-9}.

Appendix E

Basic principles of laser-Doppler anemometry

This appendix gives a compilation of the most important relations and principles. Much of the material is taken from Adrian (1996) and from the volume of Durst *et. al* (1981), and the intention is to give easy access to the formulas and fundamentals of the LDA technique. A short description of the method used for adjusting the overlap of the two laser beams is given at the end of this appendix, see page 155.

E.1 Doppler shift

A moving particle is located at $\mathbf{x}_i(t)$, and scatters light with the electric vector $\mathbf{E}_{li}$, from an incident illuminating electric vector $\mathbf{E}_{0l}$, see figure E.1. The illuminating wave is supposed to be linearly polarized, plane wave with frequency ω_{0l}. Its direction of propagation is $\hat{\mathbf{s}}_l$, with wavenumber $k = 2\pi/\lambda$, its polarization is $\hat{\mathbf{p}}_l$, and its intensity is I_{0l} [W/(m^2, sr)]. The wave can be represented by

$$\mathbf{E}_{0l} = \sqrt{I_{0l}(\mathbf{x})} e^{\jmath \Phi_{0l}(\mathbf{x})} \hat{\mathbf{p}}_l, \tag{E.1}$$

where Φ_{0l} is the phase evaluated at $\mathbf{x}$. The phase, Φ_{0l}, can be written as

$$\Phi_{0l}(\mathbf{x}, t) = \omega_{0l} t - k\, \hat{\mathbf{s}}_l \cdot \mathbf{x}. \tag{E.2}$$

A point $\mathbf{r}$ is located in the far field if $r = |\mathbf{r}|$ is larger than the wavelength and the diameter of the particle. In the far field the scattered waves are spherical regardless of the shape of scattering particle,

$$\mathbf{E}_{li} = \sqrt{I_{0l}(\mathbf{x}_i)} \frac{\boldsymbol{\sigma}_{li}}{k|\mathbf{r} - \mathbf{x}_i|} e^{\jmath [\Phi_{0l}(\mathbf{x}_i, t) - k|\mathbf{r} - \mathbf{x}_i|]}. \tag{E.3}$$

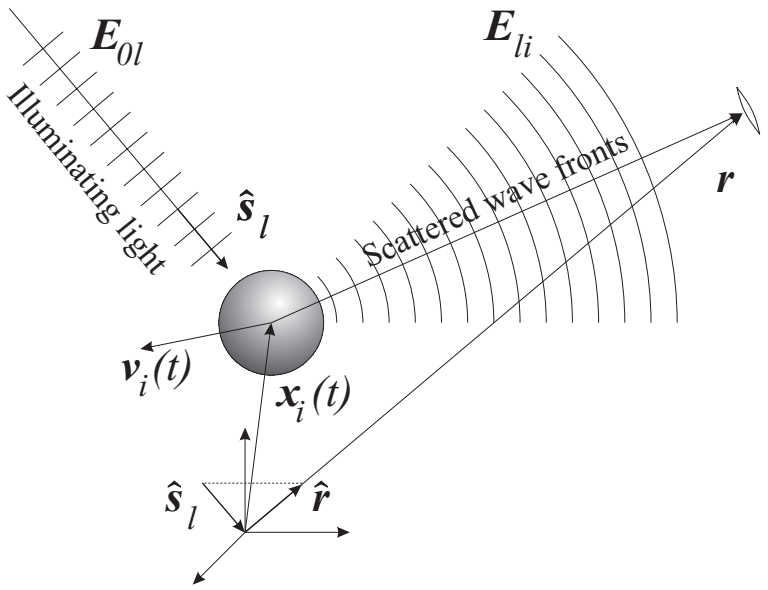

Figure E.1: Scattering from a particle

The phase of the scattered light is

$$\Phi_{li} = \Phi_{0l} - k\,|\mathbf{r} - \mathbf{x}_i|. \tag{E.4}$$

If $|\mathbf{x}_i| \ll |\mathbf{r}|$, vectors $\mathbf{r} - \mathbf{x}_i$ and $\mathbf{r}$ are nearly parallel, and $|\mathbf{r} - \mathbf{x}_i| \approx |\mathbf{r}| - \mathbf{x}_i \cdot \hat{\mathbf{r}}$, where $\hat{\mathbf{r}}$ is the unit vector in the $\mathbf{r}$ direction. Thus the phase of the scattered light can be written as

$$\begin{aligned}
\Phi_{li} &= \Phi_{0l} - k\,|\mathbf{r} - \mathbf{x}_i| \\
\Phi_{li} &= \omega_{0l} t - k\,\hat{\mathbf{s}}_l \cdot \mathbf{x}_i - k\,|\mathbf{r} - \mathbf{x}_i| \\
\Phi_{li} &= \omega_{0l} t - k\,\hat{\mathbf{s}}_l \cdot \mathbf{x}_i - k\,r + k\,\mathbf{x}_i \cdot \hat{\mathbf{r}} \\
\Phi_{li} &= \omega_{0l} t - k\,r + k\,\mathbf{x}_i \cdot (\hat{\mathbf{r}} - \hat{\mathbf{s}}_l).
\end{aligned} \tag{E.5}$$

The instantaneous frequency of the scattered light is

$$\frac{d\Phi_{li}}{dt} = \omega_{0l} + k\,\mathbf{v}_i(t) \cdot (\hat{\mathbf{r}} - \hat{\mathbf{s}}_l), \tag{E.6}$$

where $\mathbf{v}_i$ (t) is the instantaneous velocity of the particle. If we express the frequency in Hertz instead we get

$$\nu_{li} = \frac{1}{2\pi}\frac{d\Phi_{li}}{dt} = \nu_{0l} + \frac{\mathbf{v}_i(t) \cdot (\hat{\mathbf{r}} - \hat{\mathbf{s}}_l)}{\lambda}. \tag{E.7}$$

An alternative way to see the Doppler effect will be given here. Consider

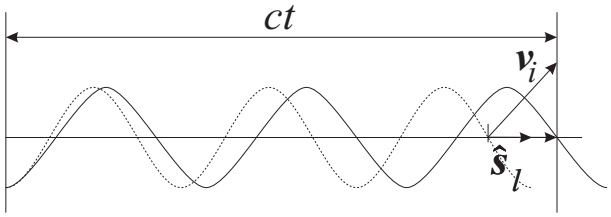

Figure E.2: Doppler shift from a moving sender.

a wave source moving with velocity $\mathbf{v}_i$, see figure E.2. The emitted waves are confined in a space $(c - \mathbf{v}_i \cdot \hat{\mathbf{s}}_l)\, t$, whereas the space would be $c \cdot t$ for the stationary wave. The wavelength, λ', seen by a stationary observer is

$$\lambda' = \frac{c - \mathbf{v}_i \cdot \hat{\mathbf{s}}_l}{\nu}, \tag{E.8}$$

and expressed in frequency

$$\nu' = \frac{\nu}{(1 - \frac{1}{c}\mathbf{v}_i \cdot \hat{\mathbf{s}}_l)}. \tag{E.9}$$

If the observer is moving and the wave source is stationary, a change in frequency is observed

$$\nu' = \frac{1}{\lambda}(c - \mathbf{v}_i \cdot \hat{\mathbf{s}}_l). \tag{E.10}$$

A moving transmitter can be considered. It receives waves from a stationary source and retransmits to a stationary observer. The frequency of transmitted waves is equal to received waves, thus

$$\nu_p = \nu(1 - \frac{1}{c}\mathbf{v}_i \cdot \hat{\mathbf{s}}_l). \tag{E.11}$$

The frequency seen by the stationary receiver is also Doppler shifted

$$\nu_l = \frac{\nu_p}{1 - \frac{1}{c}\mathbf{v}_i \cdot \hat{\mathbf{r}}} = \nu \frac{1 - \frac{1}{c}\mathbf{v}_i \cdot \hat{\mathbf{s}}_l}{1 - \frac{1}{c}\mathbf{v}_i \cdot \hat{\mathbf{r}}}. \tag{E.12}$$

Measurements made by means of the laser-Doppler anemometer are done by letting two focused Gaussian laser beams, with directions $\hat{\mathbf{s}}_1$ and $\hat{\mathbf{s}}_2$, intersect at their focusing point. The fluid is seeded with particles which act like receivers and transmitters of light. The scattered light is detected by optics and the scattered light from the two laser beams are optically mixed. The detectors are two slow to directly determine the frequency, ν_l, of the

light from the laser beam and to resolve the small Doppler shift. Therefore two laser beams are mixed (heterodyne mixing) at the detector. A beat signal with the difference in frequency of the two beams is obtained.

$$\begin{aligned} \Delta\nu &= \nu_2 - \nu_1 \\ \Delta\nu &= \nu \left(\frac{1 - \frac{1}{c}\mathbf{v}_i \cdot \hat{\mathbf{s}}_1}{1 - \frac{1}{c}\mathbf{v}_i \cdot \hat{\mathbf{r}}} - \frac{1 - \frac{1}{c}\mathbf{v}_i \cdot \hat{\mathbf{s}}_2}{1 - \frac{1}{c}\mathbf{v}_i \cdot \hat{\mathbf{r}}} \right) \end{aligned}$$

$$\text{if} \quad |\mathbf{v}_i| \ll c$$

$$\Delta\nu \;\rightarrow\; \frac{1}{\lambda}\,\mathbf{v}_i \cdot (\hat{\mathbf{s}}_2 - \hat{\mathbf{s}}_1) \quad \text{as} \quad \frac{1}{c}\mathbf{v}_i \cdot \hat{\mathbf{r}} \;\rightarrow\; 0 \tag{E.13}$$

In heterodyne mixing the trigonometric relation

$$\sin\omega_2 t \sin\omega_1 t = \underbrace{\frac{1}{2}\cos(\omega_2 + \omega_1)t}_{\text{too high frequency to detect}} + \underbrace{\frac{1}{2}\cos(\omega_2 - \omega_1)t}_{\text{the Doppler shift}}$$

is used. The cross product, $\sin\omega_2 t \sin\omega_1 t$, is obtained in the output,

$$(\sin\omega_2 t + \sin\omega_1 t)^2$$

of the photodetector, which is a square-law device. The sum of the frequencies is too high for the detector with regard to response time, so the output of the detector is the difference in frequency, the Doppler shift. In equation E.13 we see that the Doppler frequency is directly proportional to the velocity:

$$\nu_{D,i} = \Delta\nu_i = \frac{\mathbf{v}_i \cdot (\hat{\mathbf{s}}_2 - \hat{\mathbf{s}}_1)}{\lambda} \tag{E.14}$$

This can be rewritten as

$$\nu_{D,i} = \frac{\mathbf{K} \cdot \mathbf{v}_i}{2\pi} \tag{E.15}$$

where

$$\mathbf{K} = \frac{2\pi(\hat{\mathbf{s}}_2 - \hat{\mathbf{s}}_1)}{\lambda}. \tag{E.16}$$

If $u_i(t)$ is the velocity in the $\hat{\mathbf{s}}_2$-$\hat{\mathbf{s}}_1$ direction, we can write

$$u_i(t) = \frac{2\pi\,\nu_{D,i}}{K} \tag{E.17}$$

where

$$K = |\mathbf{K}| = \frac{4\pi \sin\kappa}{\lambda}, \tag{E.18}$$

and thus 2κ is the angle between the beams, $\hat{\mathbf{s}}_1$ and $\hat{\mathbf{s}}_2$.

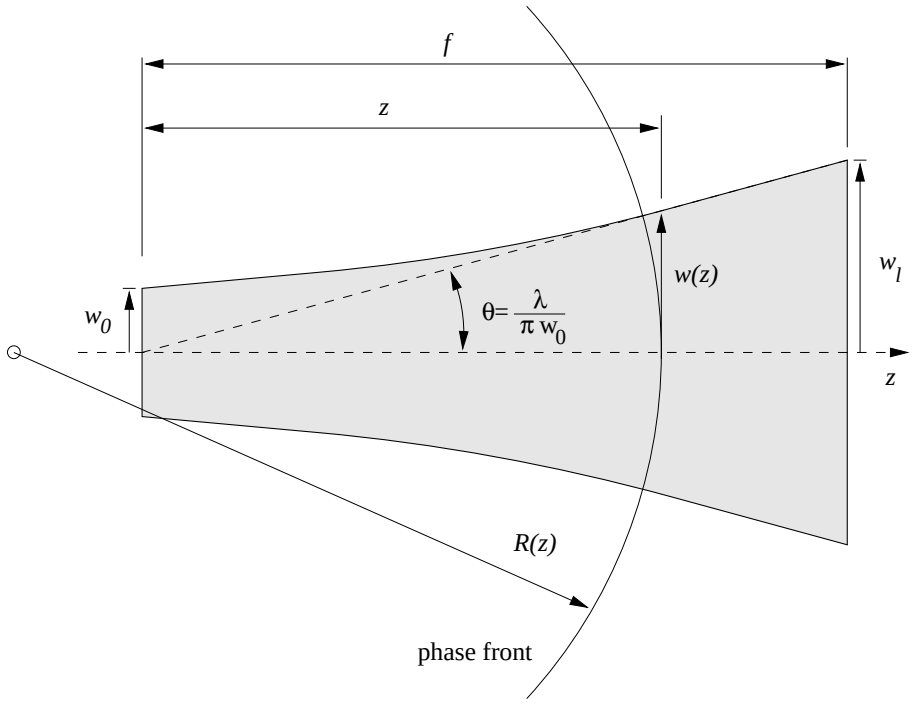

Figure E.3: Contour of a Gaussian beam.

E.2 Beam waist radius

Figure E.3 shows the contour of a focused Gaussian laser beam. The contour is given as e^{-2} of the peak value. The asymptotic angle of divergence is given by:

$$\theta = \frac{\lambda}{\pi w_0} \tag{E.19}$$

If the angle θ is small,

$$\theta \approx \tan\theta = \frac{w_l}{f} \tag{E.20}$$

The beam waist radius, w, is given by

$$w^2(z) = w_0^2 \left[1 + \left(\frac{\lambda z}{\pi w_0^2}\right)^2\right] \tag{E.21}$$

where w_l is the beam radius at location of the lens and w_0 is the minimum beam waist at the focus point.

$$w^2(z) \approx \frac{\lambda^2 f^2}{\pi^2 w_l^2} \left[1 + \left(\frac{\lambda z}{\pi w_0^2}\right)^2\right]$$

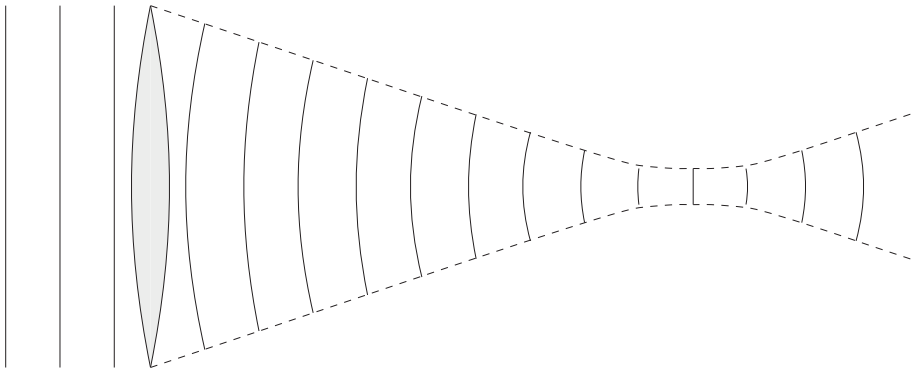

Figure E.4: Sketch of a focused Gaussian laser beam. Lines indicate wave fronts.

$$\frac{w^2(z)}{w_l^2} \approx \frac{\lambda^2 f^2}{w_l^4}\left[\frac{1}{\pi^2} + \frac{w_l^4}{\lambda^2 f^2}\frac{z^2}{f^2}\right]$$

In a dimensionless form, the equation can be written as

$$\tilde{w}(\tilde{z}) \approx \sqrt{A^2 + \tilde{z}^2} \tag{E.22}$$

where

$$\tilde{w} = \frac{w}{w_l} \qquad \tilde{z} = \frac{z}{f} \qquad A = \frac{\lambda f}{\pi w_l^2}$$

In figure E.5, the expression above is plotted for different values of A. From a laser, spherical wave fronts diverge, see figure E.6. The beam waist diameter is $D_{e^{-2}}$. An optical system, here a perfect thin lens with focal length f, focuses the laser beam. The converging laser beam focuses to a minimum diameter, $d_{e^{-2}}$, due to diffraction. As the wave fronts reach to the point of minimal waist diameter, s_1, the radius of the wave fronts increases. At the point, s_1, the wave fronts are planar, see figure E.4. The focal point, s_1, is located at

$$s_1 = f + \frac{s_0 - f}{\left(\frac{s_0}{f} - 1\right)^2 + \left(\frac{\pi D_{e^{-2}}^2}{4f\lambda}\right)^2} \tag{E.23}$$

and the minimal diameter of the focal spot is given by

$$\frac{1}{d_{e^{-2}}^2} = \frac{1}{D_{e^{-2}}^2}\left(1 - \frac{s_0}{f}\right)^2 + \left(\frac{\pi D_{e^{-2}}^2}{4f\lambda}\right)^2 \tag{E.24}$$

Errors can occur, since the initially parallel beams in laser-Doppler anemometry systems will intersect at the focal point, f. This point may be different

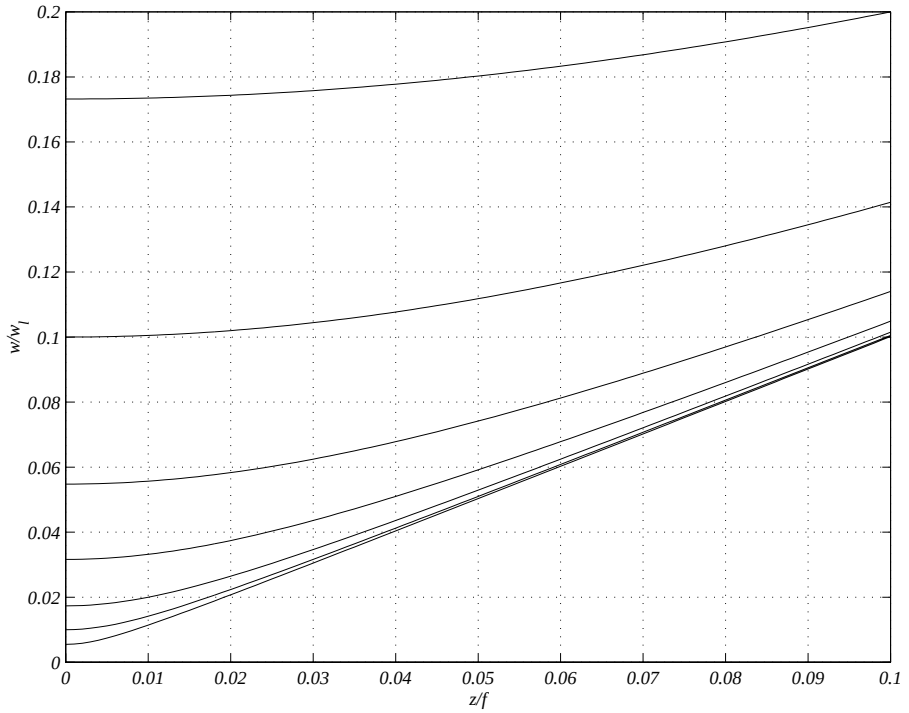

Figure E.5: Contour of a Gaussian beam. A variation in parameter A is made from the bottom; 0.0055, 0.0100, 0.0173, 0.0316, 0.0548 and 0.1000.

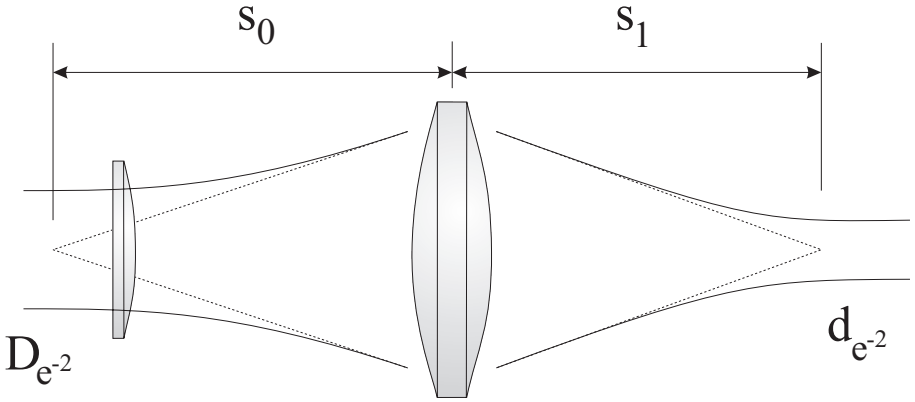

Figure E.6: Contour of a focused Gaussian laser beam.

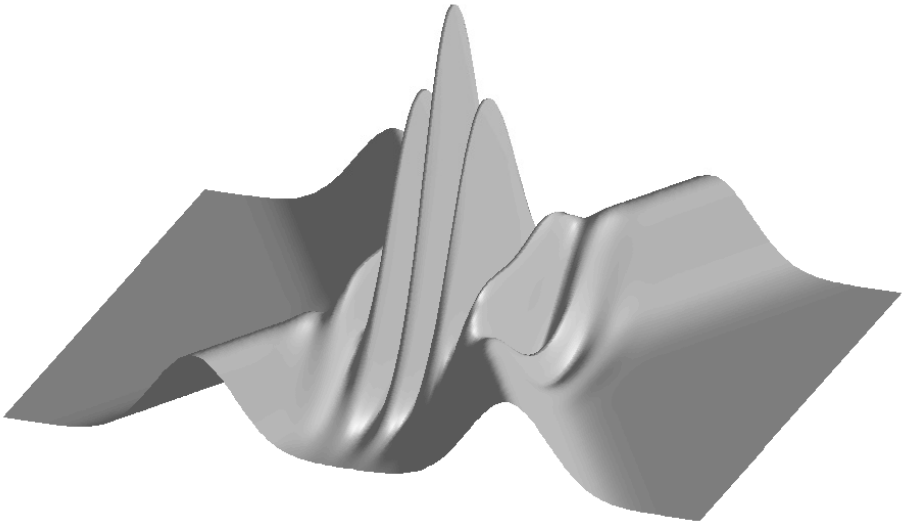

Figure E.7: Fringe pattern from two crossing Gaussian laser beams.

from s_1. These errors are usually small in laser-Doppler applications, for focal lengths up to some hundred millimeters and $s_1 \approx f$. An approximation of $d_{e^{-2}}$ is applicable

$$d_{e^{-2}} \approx \frac{4f\lambda}{\pi D_{e^{-2}}} \tag{E.25}$$

E.3 The LDA signal

A laser beam with plane waves fronts is focused by a lens to form spherical waves, see figure E.4. Near the focus point the wave fronts are approximately plane. The laser beam can be treated as a plane wave near the focus point. The particle scatters light from the two intersecting laser beams. The scattering coefficient is usually a function of the angle between the polarization vector of the laser light and the direction of the illuminating beam, thus $\boldsymbol{\sigma}_{li} = \boldsymbol{\sigma}_{li}(\hat{\mathbf{p}}_l, \hat{\mathbf{s}}_l, \hat{\mathbf{r}})$. The sum of the scattered waves is detected at the detector.

$$\mathbf{E}_i = \mathbf{E}_{1i} + \mathbf{E}_{2i} \tag{E.26}$$

The light intensity is

$$I = \mathbf{E}_i \cdot \mathbf{E}_i^* = \mathbf{E}_{1i} \cdot \mathbf{E}_{1i}^* + \mathbf{E}_{2i} \cdot \mathbf{E}_{2i}^* + \mathbf{E}_{2i} \cdot \mathbf{E}_{1i}^* + \mathbf{E}_{1i} \cdot \mathbf{E}_{2i}^* \tag{E.27}$$

Together with equations E.3, E.5, E.16, E.27, we get

$$I_i(\mathbf{r}, \mathbf{x}_i, t) = \frac{I_{01}\boldsymbol{\sigma}_{1i} \cdot \boldsymbol{\sigma}_{1i}^*}{k^2 r^2} + \frac{I_{02}\boldsymbol{\sigma}_{2i} \cdot \boldsymbol{\sigma}_{2i}^*}{k^2 r^2} + \frac{2\sqrt{I_{01} I_{02}}}{k^2 r^2} \mathrm{Re}\left(\boldsymbol{\sigma}_{1i} \cdot \boldsymbol{\sigma}_{2i}^* e^{j\Phi_i(t)}\right) \tag{E.28}$$

where

$$\Phi_i(t) = 2\pi\nu_S t + k\mathbf{x}_i(t) \cdot (\hat{\mathbf{s}}_2 - \hat{\mathbf{s}}_1) \tag{E.29}$$

The frequency, ν_S, is a shift in frequency in one of the illuminating laser beams. This is done because it is difficult to detect the 180° shift in phase when there is a change in the sign of the velocity. The shift in frequency causes the fringe pattern to move in one direction. Velocity fluctuations about zero correspond to a shift about the shift frequency, ν_S. The shift can be accomplished by e.g. an acoustic Bragg cell made of glass. In the Bragg cell, e.g. 40 MHz standing sound waves create a diffraction pattern, just like a grating. The beam going right through the cell is not shifted, and the first diffracted beam is shifted 40 MHz. Thus the frequency shifted laser-Doppler anemometer can distinguish between negative and positive velocities, if the velocities are not too high. The frequency shift also removes angular bias. This bias effect occurs when a particle moves along the fringes and perhaps only a few fringes are crossed. There is then not enough information in the signal to obtain a valid sample. The light flux (W/m^2) hitting the detector through the aperture that subtends the solid angle Ω, is

$$J_i(t) = \int_\Omega I(\mathbf{r}, \mathbf{x}_i, t)\, \mathbf{r}^2\, d\Omega. \tag{E.30}$$

Which can be rewritten as

$$J_i(t) = \frac{1}{k^2}\left(I_{01}P_{1i} + I_{02}P_{2i} + \sqrt{I_{01}I_{02}}D_i \cos[\Phi_i(t) - \Psi_i]\right) \tag{E.31}$$

where P_{1i}, P_{2i} and D_i are the integrals over the solid angle of the scattering coefficients. The integrated value of the phase shifts because of the phase difference between $\mathbf{E}_{1i}$ and $\mathbf{E}_{2i}$. The first two terms in equation E.31 are called the *pedestal*. They arise from the single scattering from a single laser beam. The term containing D_i is the Doppler signal and is a result of the heterodyne mixing of $\mathbf{E}_{1i}$ and $\mathbf{E}_{2i}$. Thus, the pedestal is

$$J_{P_i}(t) = \frac{1}{k^2}\left(I_{01}[\mathbf{x}_i(t)]P_{1i} + I_{02}[\mathbf{x}_i(t)]P_{2i}\right) \tag{E.32}$$

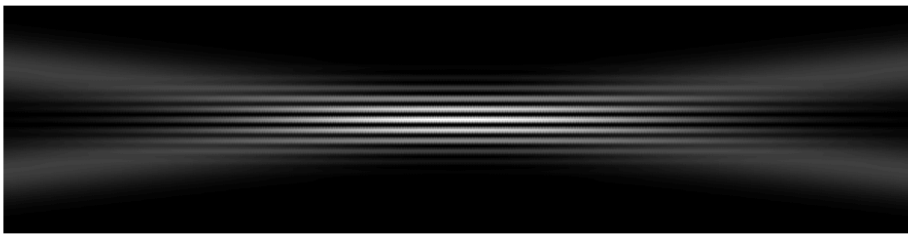

Figure E.8: The intensity as seen by the detector from the scattering of a small particle in the field of two focused Gaussian laser beams.

and the Doppler signal is

$$J_{D_i}(t) = a[\mathbf{x}_i(t)]D_i \cos[\Phi_i(t) - \Psi_i] \tag{E.33}$$

where

$$a[\mathbf{x}_i(t)] = k^{-2}\sqrt{I_{01}I_{02}}. \tag{E.34}$$

A term called *visibility* is defined as

$$V_i(t) = \frac{\sqrt{I_{01}I_{02}}D_i}{I_{01}P_{1i} + I_{02}P_{2i}}. \tag{E.35}$$

When $I_{01}[\mathbf{x}_i(t)]$ and $I_{02}[\mathbf{x}_i(t)]$ are equal, the value of the visibility is $D_i/(P_{1i} + P_{2i})$, which is a function of the optical system. The visibility is always less than one.

E.4 The size of the measurement volume

The area of nearly constant diameter and plane wave fronts extends approximately $(f/D_{e^{-2}})d_{e^{-2}}$ on either side of the focal point. The laser beam near the focus point can be approximated by

$$\mathbf{E}_{0l} = \sqrt{I_{0l}}e^{J(\omega_{0l} - k\hat{\mathbf{s}}_l \cdot \mathbf{x})}\hat{\mathbf{p}}_l \tag{E.36}$$

where

$$I_{0l} = \frac{8\,P_{0l}}{\pi d_{e^{-2}}}e^{-\left(\frac{8\zeta^2}{d_{e^{-2}}}\right)} \tag{E.37}$$

and ζ is the radial distance from the centerline of the beam and P_{0l} is the beam power. The peak intensity at the centerline is inversely proportional to $d_{e^{-2}}$, owing to continuity. The measurement volume, mv, can be defined as the volume in which the Doppler signal is greater than e^{-2} of the peak value:

$$a(\mathbf{x}_i)D_i \geq e^{-2}a(\mathbf{0})D_i \tag{E.38}$$

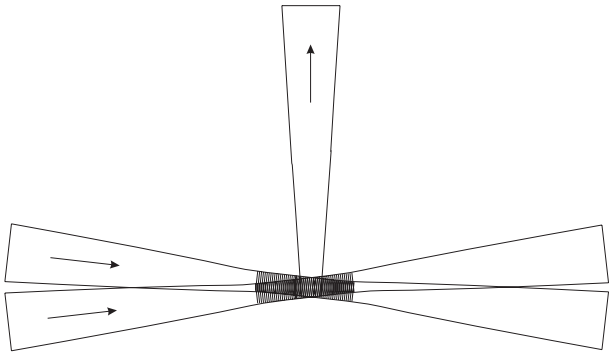

Figure E.9: An LDA system working in 'side-scatter' mode.

Together with equation E.37 one can show that $a(\mathbf{x}_i)$ is:

$$a(\mathbf{x}_i) = k^{-2}\sqrt{I_{01}(\mathbf{0})I_{02}(\mathbf{0})}e^{-\frac{8}{d_{e^{-2}}}\left(x_i^2\cos^2\kappa+y_i^2\sin^2\kappa+z_i^2\right)}. \tag{E.39}$$

Near the focal point, the measurement volume is approximately ellipsoidal, with axes in x, y and z equal to

$$d_m = \frac{d_{e^{-2}}}{\cos\kappa} \tag{E.40}$$

$$l_m = \frac{d_{e^{-2}}}{\sin\kappa} \tag{E.41}$$

$$h_m = d_{e^{-2}}. \tag{E.42}$$

The volume of the measurement volume, V_D, is

$$V_D = \frac{\pi\, d_{e^{-2}}^3}{6\,\cos\kappa\,\sin\kappa}. \tag{E.43}$$

An example will be given here that illustrates the LDA system used in the measurements presented in this thesis: f=310 mm, $D_{e^{-2}}$ =4.4 mm (the diameter, $D_{e^{-2}}$, of the laser beam is 2.25 mm and is expanded 1.94 times), κ=6.4°, λ=500 nm. This implies that $d_{e^{-2}}$ =45 μm, d_m=45 μm, l_m=0.4 mm, h_m=45 μm, V_D=4.3·10^{-4} mm^3. The length of the measurement volume, l_m=0.4 mm, used in back-scatter mode, can be improved by using side-scatter. In this mode, the ellipsoid is cut off optically, and the length is l_m=45 μm. The distance between the fringes is given by a simple geometrical consideration

$$d_f = \frac{\lambda}{2\,\sin\kappa}. \tag{E.44}$$

The frequency of the signal when a particle passes the fringe pattern will be

$$\nu_D = \frac{u}{d_f} = \frac{2\,\sin\kappa}{\lambda}u \tag{E.45}$$

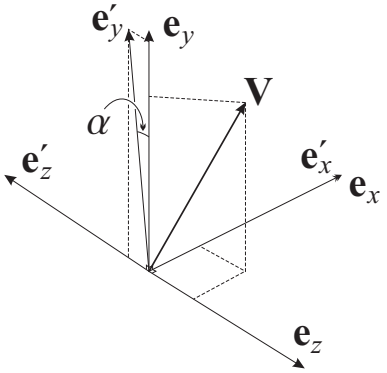

Figure E.10: Coordinate system for the velocities measured by the LDA system.

If we compare this with equation E.18, we see that $K = 2\pi/d_f$. This fringe model is not entirely correct with regard to the signal strength of larger particles, $d_p/d_f > 1.22$. For particles small compared to the fringe spacing but large compared to the wavelength of the light, i.e. $2\pi\, d_p/\lambda < 60$, the model gives an intuitive picture of the Doppler signal. Remember that the signal is the sum of wave fronts, scattered according to the theory of Mie, from different parts of the particle, that reaches the detector.

The number of fringes in the measurement volume can be calculated as

$$N_{FR} = \frac{d_m}{d_f} = \frac{2\, d_{e^{-2}}\, \tan\kappa}{\lambda} \tag{E.46}$$

In the example above, $d_f = 2.2$ μm and N_{FR}=20.

E.5 Optical transformation of the velocity components

It is usually not possible to measure the velocity component along the axes of the Cartesian coordinate system. When measurements are made close to a wall, one beam pair has to be tilted as in figure E.11. Figure E.10 shows how the LDA system measures velocity components along the non-orthogonal axes marked with a prime, denoted $\mathbf{e}'_x$, $\mathbf{e}'_y$ and $\mathbf{e}'_z$. It is relatively simple to reconstruct the orthogonal velocity components, if all three velocity components are measured simultaneously, by a matrix transformation. The velocity vector, $\mathbf{V}$, is projected onto each of the unit

vectors $\mathbf{e'}_x$, $\mathbf{e'}_y$ and $\mathbf{e'}_z$;

$$\begin{cases} U' = \mathbf{V} \cdot \mathbf{e'}_x \\ V' = \mathbf{V} \cdot \mathbf{e'}_y \\ W' = \mathbf{V} \cdot \mathbf{e'}_z \end{cases} \tag{E.47}$$

The velocity components in a Cartesian coordinate system are obtained by multiplication with the inverse matrix:

$$\begin{pmatrix} U \\ V \\ W \end{pmatrix} = \begin{pmatrix} \mathbf{e}_x \cdot \mathbf{e'}_x & \mathbf{e}_y \cdot \mathbf{e'}_x & \mathbf{e}_z \cdot \mathbf{e'}_x \\ \mathbf{e}_x \cdot \mathbf{e'}_y & \mathbf{e}_y \cdot \mathbf{e'}_y & \mathbf{e}_z \cdot \mathbf{e'}_y \\ \mathbf{e}_x \cdot \mathbf{e'}_z & \mathbf{e}_y \cdot \mathbf{e'}_z & \mathbf{e}_z \cdot \mathbf{e'}_z \end{pmatrix}^{-1} \cdot \begin{pmatrix} U' \\ V' \\ W' \end{pmatrix} \tag{E.48}$$

If we consider the case in figure E.10 (which is the same as that used in the measurements in part II, α was here 9°) the transformation matrix is:

$$\begin{pmatrix} U \\ V \\ W \end{pmatrix} = \begin{pmatrix} 1 & 0 & 0 \\ 0 & \frac{1}{\cos\alpha} & -\tan\alpha \\ 0 & 0 & -1 \end{pmatrix} \cdot \begin{pmatrix} U' \\ V' \\ W' \end{pmatrix} \tag{E.49}$$

E.6 Bias in LDA measurements

E.6.1 Velocity bias

If the particle distribution is uniform, the rate of particles arriving at the measurement volume will depend on the velocity and thus affect the statistics, called *velocity bias*, see McLaughlin & Tiederman (1973). This is a serious problem since it cannot be corrected by simply taking more samples - a systematic error persists. The statistical moment computed by a summation over all samples will cause biased ensemble averages, even if every single velocity sample is correct. The way to correct this bias is to use a residence time weight in the summation over all samples, see George (1976). The statistical velocity bias was thus removed as

$$\overline{U}_i = \frac{\sum_{k=1}^{N} u_i(k)\Delta\tau(k)}{\sum_{k=1}^{N} \Delta\tau(k)} \qquad \overline{u_i u}_j = \frac{\sum_{k=1}^{N} \left(u_i(k) - \overline{U}_i\right)\left(u_j(k) - \overline{U}_j\right)\Delta\tau(k)}{\sum_{k=1}^{N} \Delta\tau(k)} \tag{E.50}$$

where $\Delta\tau(k)$ is the residence time (transit time) for the k^{th} sample. As an estimate of $\Delta\tau(k)$, a typical length (the diameter) of the measurement volume was divided by velocity magnitude of the k^{th} sample. This is not entirely correct since the particle may take different trajectories through the

measurement volume. The effective length is then shorter (or longer). The motivation for using the velocity magnitude is that the residence time obtained from the hardware was not believed to be correct. There was simply too little correlation between the inverse residence time and the velocity magnitude. Some scatter is expected since particles cross the measurement volume randomly, as was mentioned. The difference between using the residence time weight and the inverse velocity magnitude weight was not large, however. It will not change the interpretation of the time averaged velocity field.

E.6.2 Velocity gradient bias

If the measurement volume is situated in a position where large gradients in the mean velocity field within the measurement volume persist, another type of bias arises called *velocity gradient bias*. Samples in areas with high velocity are weighted in more to the average value. Another motivation for operating the LDA system in side-scatter mode is to keep the measurement volume as small as possible. Correction methods have been suggested by e.g. Durst *et. al* (1992);

$$\begin{aligned} \overline{U}_{corr} &= \overline{U}(y_c) + \frac{d_m^2}{\text{const}} \left(\frac{\partial^2 \overline{U}(y)}{\partial y^2} \right) \Bigg|_{y_c} \\ \overline{u^2}_{corr} &= \overline{u^2}(y_c) + \frac{2\, d_m^2}{\text{const}} \left(\frac{\partial \overline{U}(y)}{\partial y} \right) \Bigg|^2_{y_c} \end{aligned} \tag{E.51}$$

The constant is 24 for top hat light intensity distribution in the measurement volume and 32 for Gaussian. From equation E.51 we can see that the mean value is only affected by the curvature whereas the second order moments depend on the mean velocity gradient. The correction to $\overline{U}$ and $\overline{u^2}$ increases with the square of the diameter of the measurement volume.

E.6.3 Noise in the LDA signal

In order to be able to make measurement close to the wall (0.3 mm) it was necessary to reduce the reflections from the laser beams. This was accomplished in two ways; first the test plate was painted with a black matte paint together with a fluorescent dye, *Rhodamine*, coating, and secondly the LDA operated in side-scatter mode.

E.6.4 Inhomogeneous seeding levels

It is important to have a homogeneous seeding level everywhere in the flow. When two air streams mix, care must be taken to ensure that this is the case. Otherwise, fluid packages from one of the air streams will have a higher weight in the average. The wind tunnel used in this study has two closed loops that are connected to each other - the condition for homogeneous seeding levels is thus good.

E.6.5 Misalignment of the laser beams

If the laser beams do not cross at their focus point (where the wave fronts are plane) the fringe pattern will be distorted. The spacing between the fringes will be different in different positions of the measurement volume (the calibration constant, K, is different in different regions) . This causes a fictitious increase in the RMS values.

E.7 Adjusting the beam overlap

The quality of the Doppler signal is determined by how well the laser beams cross at the focus point of the receiving fiber. This is usually checked on an optical bench on which the laser optics are mounted in a firm holder. A pinhole with a diameter of $\sim d_m$ (50 μm was used in these experiments) is used to find the focus of the receiver optics. Maximum light transmission is checked with a photo diode. In the same, way maximum transmission of the laser beams is ensured. When a good overlap is reached the laser beams should create diffraction patterns, *Airy discs*, after the pinhole. Experience has shown that this is a very important adjustment and that care should be taken in executing it. In the experiment described in this thesis, a window was situated between the measurement volume and the front lens. A slightly tilted arrangement was use in order to be able to make measurements close to the wall. In this way, the two laser beams have different inclinations to the window and will be refracted differently. The overlap will then be poor. Instead the pinhole was mounted at the position of the actual measurement to ensure that a good overlap was established, see figure E.11. This adjustment was made on both probes. Secondly the probes themselves were adjusted so that the two measurement volumes overlapped, simply by maximizing the data rate and degree of validation when the signal processors worked in coincidence mode (master/master/master).

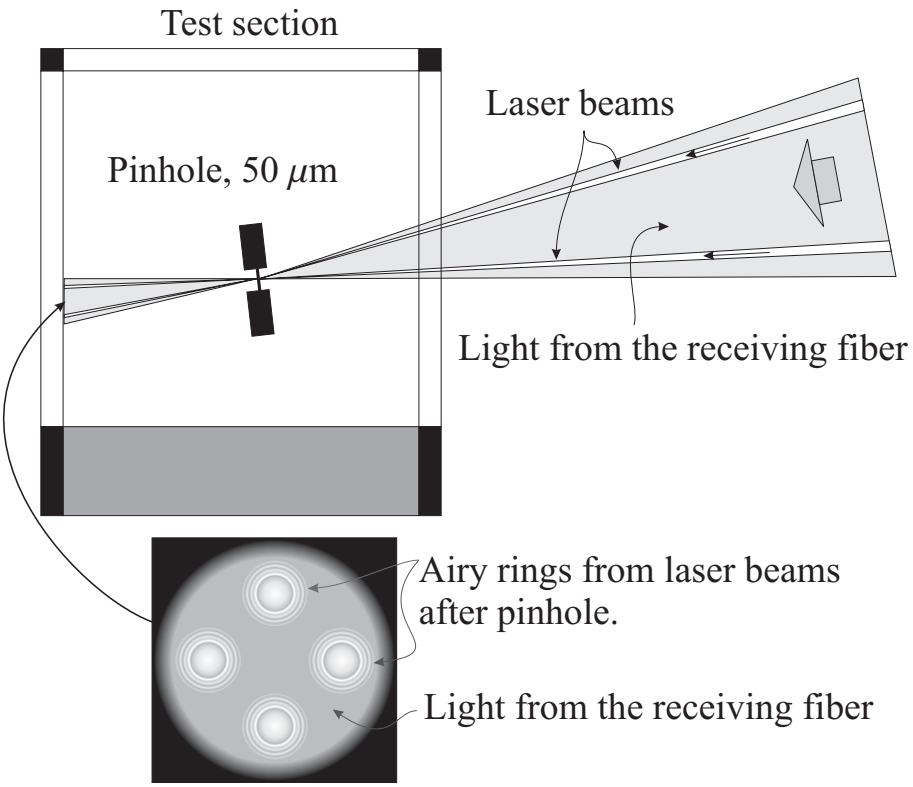

Figure E.11: Adjustment of the laser beam crossing at the focus of the receiving optics.